



HAL
open science

Mass transfer coefficients across dynamic liquid steel/slag interface

Leandro Dijon de Oliveira Campos

► **To cite this version:**

Leandro Dijon de Oliveira Campos. Mass transfer coefficients across dynamic liquid steel/slag interface. Mechanics [physics]. Université de Bordeaux, 2017. English. NNT: 2017BORD0554. tel-01531356

HAL Id: tel-01531356

<https://theses.hal.science/tel-01531356>

Submitted on 1 Jun 2017

HAL is a multi-disciplinary open access archive for the deposit and dissemination of scientific research documents, whether they are published or not. The documents may come from teaching and research institutions in France or abroad, or from public or private research centers.

L'archive ouverte pluridisciplinaire **HAL**, est destinée au dépôt et à la diffusion de documents scientifiques de niveau recherche, publiés ou non, émanant des établissements d'enseignement et de recherche français ou étrangers, des laboratoires publics ou privés.

THÈSE PRÉSENTÉE
POUR OBTENIR LE GRADE DE
DOCTEUR DE
L'UNIVERSITÉ DE BORDEAUX

ECOLE DOCTORALE DES SCIENCES PHYSIQUES ET DE L'INGENIEUR
SPÉCIALITÉ : MECANIQUE

Par Leandro Dijon DE OLIVEIRA CAMPOS

**MASS TRANSFER COEFFICIENTS ACROSS DYNAMIC
LIQUID STEEL/SLAG INTERFACE**

Sous la direction de : Jean-Paul CALTAGIRONE
(co-directeur : Stéphane VINCENT)

Soutenue le 10 Mars 2017

Membres du jury :

M. BRUNEAU, Charles-Henri	Professeur Inst. de Mathématique de Bordeaux	Président
M. ESTIVALEZES, Jean-Luc	Ingénieur de Recherche, ONERA-DMAE	rapporteur
M. ZALESKI, Stéphane	Professeur de l'Institut d'Alembert	rapporteur
M. BUCHLIN, Jean-Marie	Professeur, Von Karman Institute	Examineur
M. GARDIN, Pascal	Ingénieur Recherche (HDR), ArcelorMittal R&D	Co-Encadrant

“Vamos pro combate !”

Rocha, F.C.M.

Title : Mass Transfer Coefficients Across Dynamic Liquid Steel/Slag Interface

Abstract :

In order to characterize the mass transfer coefficients (MTC) of different species across liquid steel/slag interface, a multiphase Computational Fluid Dynamic (CFD) model was developed. MTC's are estimated from models based on physicochemical and hydrodynamic parameters, such as mass diffusivity, interface shear and divergence strength. These models were developed for gas-liquid interactions with relative low Schmidt ($Sc=vD$) numbers ($Sc\approx 200$). However, the industrial processes involve mass transfer of chemical species with Sc number ranging from 10^3 to 10^4 . To evaluate the applicability of these existing models, the fluid flow in the vicinity of a liquid/liquid interface is investigated. Computational Fluid Dynamic (CFD) and Laser Doppler Anemometry (LDA) were used to calculate and measure the velocity field on a continuous casting (CC) water model configuration. The work provides new insights and original measures to understand the fluid flow near liquid-liquid interfaces.

The mass transfer model of an industrial continuous casting mold showed that the mass transfer coefficients are not homogeneously distributed, and slag properties should follow this trend. This non-homogeneity was confirmed by physical experiments performed with a water model of a CC configuration and its CFD representation. The calculated flow was used to predict the MTC and the interface area between phases, since the interface is constantly moving. These parameters will be the input of thermodynamic models to predict slag composition and viscosity. This methodology is currently under validation, and it will also be applied to improve steel plant performance in the desulphurization process.

Keywords : mass transfer; interface; multiphase flow; numerical simulation; CFD; experiments.

Titre : Identification des coefficients de transfert de masse à travers d'une interface acier liquide/laitier liquide dynamique

Résumé :

Afin de prédire l'évolution de la composition chimique du laitier dans différents procédés sidérurgiques, un modèle CFD a été développé. Les coefficients de transfert de masse sont

estimés à partir des modèles basés sur les paramètres physico-chimiques et hydrodynamiques, comme par exemple la diffusivité des espèces chimiques et la divergence de l'interface. Ces modèles ont été développés pour la prédiction du transfert gaz-liquide où les nombres de Schmidt ($Sc=vD$) sont relativement faibles ($Sc\approx 200$). Par contre, les procédés industriels ont un nombre de Sc considérablement plus important, de l'ordre de 10^3 à 10^4 . Pour évaluer la pertinence de ces modèles, l'hydrodynamique au voisinage d'une interface liquide-liquide a été étudiée. Un modèle CFD et des mesures par l'anémométrie laser (LDA) ont été utilisés pour calculer et valider les champs de vitesse d'une maquette à eau d'une lingotière de coulée continue (CC).

Le modèle de transfert de masse d'une lingotière de coulée continue industrielle nous a montré que les coefficients de transfert de masse ne sont pas distribués de manière homogène, et les propriétés physiques du laitier ne doivent pas y être non plus. Cette distribution non-homogène a été confirmée par des essais physiques. Les écoulements calculés numériquement ont été utilisés pour prédire les coefficients de transfert de masse entre les deux phases liquides. Ces paramètres seront utilisés comme données d'entrée pour un modèle de thermodynamique afin de prédire l'évolution de la composition chimique du laitier.

Mots clés: transfert de masse; interface; écoulement multiphasique; simulation numérique; CFD.

Laboratoire TREFLE de l'I2M

(UMR CNRS 52 95) / Site ENSCBP 16 Avenue Pey Berland 33607 Pessac cedex

Titre : Identification des coefficients de transfert de masse à travers d'une interface acier liquide/laitier liquide dynamique

Résumé :

Afin de prédire l'évolution de la composition chimique du laitier dans différents procédés sidérurgiques, il est nécessaire de de décrire en détail les écoulements au voisinage de l'interface séparant l'acier liquide du laitier. Dans la présente étude, nous avons étudié à la fois expérimentalement et par simulation numérique la dynamique de l'interface entre les deux liquides.

Les nouveaux aciers par exemple utilisés dans l'industrie automobile sont souvent chargés en éléments d'alliage, en plus de l'aluminium utilisé pour désoxyder l'acier, comme le silicium, titane, manganèse et autres... Quelques problèmes peuvent apparaître dans le procédé de coulée continue, dont un schéma est donné sur la Figure 1.

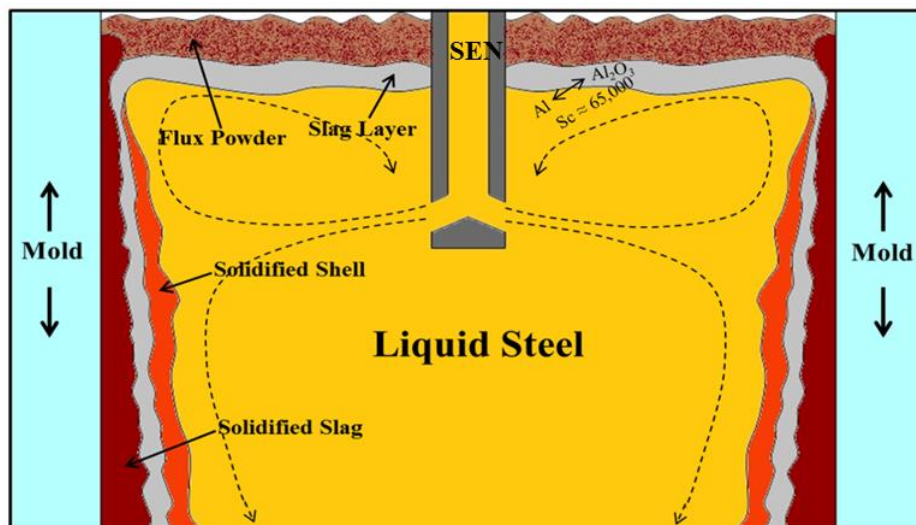


Figure 1 - Schéma de la lingotière du coulé continue de brames - largeur comprise entre 1,0 et 1,8 m, épaisseur entre 0,20 et 0,25 m.

L'acier est injecté dans la lingotière par un busette appelé *Submerged Entry Nozzle* (SEN). Pendant la coulée, une poudre est déposée sur la surface de l'acier. Cette poudre fond au contact de l'acier. Ses fonctions sont de limiter la réoxydation de l'acier au contact de l'air, d'apporter une isolation thermique, de capter les inclusions présentes dans l'acier liquide et, principalement, de lubrifier la lingotière.

Les différences de composition chimique entre l'acier liquide et le laitier induisent des transferts d'espèce chimiques. La composition du laitier peut donc évoluer très fortement entre sa composition initiale et sa composition d'équilibre avec l'acier liquide, ce qui peut produire de fortes variations de sa viscosité et une capacité de lubrification très affectée. : la peau solidifiée d'acier touche directement la lingotière, ce qui peut causer un arrêt couteux de la coulée continue. Le transfert de masse est un phénomène tellement sensible que la coulée des nouveaux aciers ne peut en général pas se faire avec les poudres conventionnelles.

Pour prédire ce changement de viscosité il est impératif d'avoir a priori une connaissance du transfert de masse à travers cette interface liquide/liquide, pour ensuite choisir la bonne composition de poudre à utiliser. Le choix de la bonne composition pourrait se faire par de essais successifs, mais le coût d'une telle opération est souvent très élevé. La simulation numérique est une alternative intéressante, dans la mesure où elle est validée.

Une recherche bibliographique exhaustive nous a indiqué la possibilité de prédire le coefficient de transfert de masse en n'utilisant que les caractéristiques hydrodynamiques locales au voisinage de l'interface et quelques propriétés thermo physiques (viscosité et diffusivité massique).

Nous avons utilisé une simulation numérique qui résout les équations de Navier-Stokes par une approche de type volumes finis implicites sur des maillages structurés. L'interface liquide/liquide est quant à elle simulée par une approche *Volume Of Fluid*. Le coefficient de tension de surface, supposé constant, est modélisé par la méthode dénommée *continuum surface force*. La turbulence a été prise en charge par un modèle aux grandes échelles ou *Large Eddy Model* (LES) où la modélisation des contraintes de sous maille repose sur un modèle d'échelle mixte.

L'hydrodynamique décrite par ce modèle a été validée par des comparaisons à des mesures réalisées dans une maquette de la lingotière où l'acier est simulé par de l'eau. Cette approximation est possible car les deux fluides ont la même viscosité cinématique et les écoulements sont en bonne similitude.

Une deuxième maquette a été conçue pour valider le calcul des coefficients de transfert de masse. Dans cette maquette, l'eau est utilisée pour simuler l'acier liquide et une couche d'huile simule le laitier liquide. Le mouvement de l'eau est produit par une injection d'air à travers la face inférieure de la maquette. Du Thymol en poudre est dissout dans l'eau pour simuler un scalaire que sera transféré vers la couche de laitier. En mesurant la concentration

de Thymol dans l'eau au cours du temps, nous avons identifié le coefficient de transfert de masse entre les phases liquides, pour différents régimes d'agitation. La comparaison des résultats de la simulation CFD sur cette configuration expérimentale nous a permis de valider le modèle de transfert de masse proposé.

Le modèle complet de prédiction de l'hydrodynamique et des coefficients de transfert de masse a été appliqué à un cas industriel. Les résultats (montrés sur la Figure 2) font ressortir une distribution très hétérogène du coefficient de transfert de masse à l'interface métal liquide/laitier.

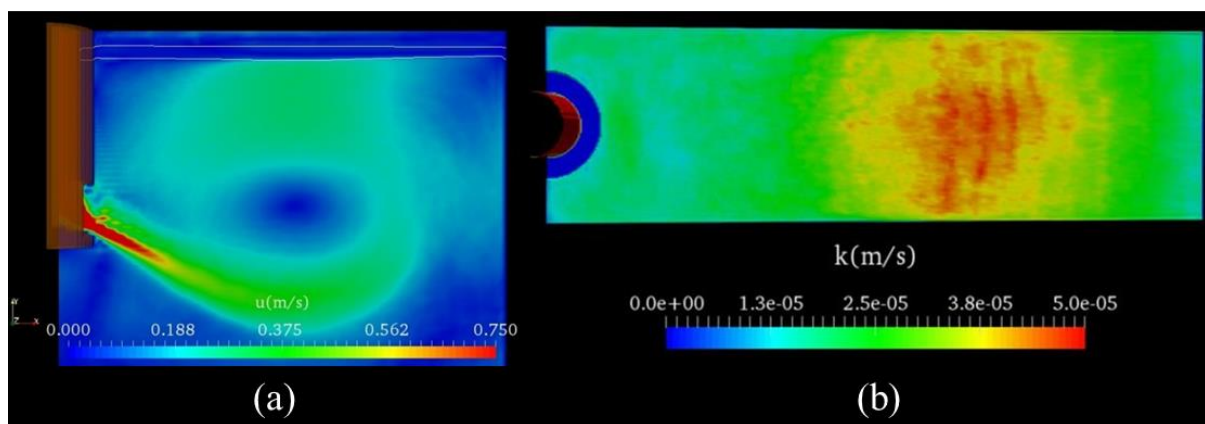


Figure 2 - Configuration industriel. (a) hydrodynamique du système. (b) coefficient de transfert de masse sur l'interface acier/laitier.

Cette constatation nous montre la nécessité d'adapter les pratiques opérationnelles actuelles. Dans les régions où les coefficients de transfert de masse sont les plus importants, il est attendu d'avoir des changements de viscosité du laitier significatifs, de sorte que la lubrification en sera localement affectée. Aujourd'hui, la même poudre est posée uniformément sur toute l'interface. Les résultats du calcul suggèrent que cette pratique doit être révisée afin de garantir une meilleure homogénéité des propriétés du laitier. Par contre, il faut garder à l'esprit que ce résultat préliminaire doit être encore complété en prenant en compte l'injection de gaz dans la busette. Avec ce modèle, il devient possible d'évaluer et choisir a priori la meilleure composition chimique initiale de la poudre pour la coulée des aciers de nouvelle génération. Afin d'évaluer l'efficacité de ce modèle, des tests sur pilote de coulée continue seront menés par les chercheurs du centre de recherche d'ArcelorMittal à Maizières-lès-Metz. Pendant ces tests, des échantillons de laitier seront prélevés et leur compositions comparés à celle prédite sur la base des calculs CFD.

Acknowledgements

There is no relevant scientific work which can be performed by an individual alone. This work is not different. Many were the contributors who made this project possible and I sincerely thank all of them. Some of them had more dedication and devoted part of their lives to further improve the quality of this project and I specially thank:

- Pascal Gardin, for the kind invitation he made me to start this thesis. It was a great opportunity for me, personally, to go through this big challenge and, professionally, to advance in the scientific field. Pascal was always motivating me and pushing me to further improve the quality of our project. He is an inspiration for my career goals and was not only a great leader but a good friend.
- The professors involved in this work, Stéphane Vincent and Jean-Paul Caltagirone. For all the provided support, pertinent questions and helpful insights. I specially thank Stéphane for his patience, friendship and availability throughout the thesis duration.
- Marcele Salgueiro, the woman who changed my life, for her support, dedication and motivational conversations. Without her this thesis would be by far one of the hardest periods of my life. Thank you for the love you shared with me, and for the common passion for science and metallurgy that united us during this whole time.
- My family, who always motivated and supported me in my decisions and always gave me the inspiration I needed to go forward.
- The ArcelorMittal team. The engineers from the steelmaking department for they supportive assistance. My colleagues from THEMEF, for all the fruitful technical exchanges. I specially thank Bastien Volland and Armand Mallinger, without whom my experiments would certainly not be performed as they were.
- And finally, to my former professors, Roberto P. Tavares, Simão Oliveira, Breno T. Maia and Sidiney Nascimento for the technical exchanges, motivational talks and inspirational stories. You are the people who made me love the iron and steelmaking.

To the many I did not mention and those who have supported me during this path, thank you!

Leandro Dijon

Table of Contents

Acknowledgements	1
Nomenclature.....	5
List of Figures.....	8
1 Introduction	11
1.1 <i>Steelmaking Processes and Mass Transfer</i>	<i>11</i>
1.2 <i>Continuous Casting.....</i>	<i>15</i>
1.3 <i>Mass Transfer in Steelmaking</i>	<i>19</i>
1.4 <i>Objectives.....</i>	<i>23</i>
2 Mass Transfer and Fluid Flow near the Interface Region	24
2.1 <i>Turbulence interactions in Multiphase Flows</i>	<i>24</i>
2.2 <i>Mass Transfer in Multiphase Flows.....</i>	<i>30</i>
2.2.1 <i>Mass Transfer across Liquid-Gas Interface – A brief overview.....</i>	<i>30</i>
2.2.2 <i>The film theory.....</i>	<i>31</i>
2.2.3 <i>The penetration model</i>	<i>34</i>
2.2.4 <i>The surface renewal time model</i>	<i>34</i>
2.2.5 <i>The surface Divergence Model</i>	<i>36</i>
2.3 <i>Conclusion</i>	<i>39</i>
3 Experimental Methods	41
3.1 <i>Continuous Casting (CC) Water Model.....</i>	<i>41</i>
3.1.1 <i>Similitude: Non-Dimensional Parameters.....</i>	<i>41</i>
3.1.2 <i>Physical Model and Fluid Properties.....</i>	<i>44</i>
3.2 <i>Velocity Measurements.....</i>	<i>46</i>
3.2.1 <i>Laser Doppler Anemometry (LDA)</i>	<i>46</i>
3.3 <i>Image processing</i>	<i>48</i>
3.3.1 <i>Python Image Processing</i>	<i>48</i>
3.3.2 <i>Experimental Interface Tracking (EIT).....</i>	<i>49</i>
3.4 <i>Conclusions.....</i>	<i>51</i>
4 Models and Numerical Methods.....	52
4.1 <i>The single fluid model</i>	<i>52</i>
4.1.1 <i>Mass Conservation</i>	<i>52</i>

4.1.2	Momentum Conservation	52
4.1.3	Navier-Stokes Equation for Single Fluid Model	53
4.2	<i>Turbulence modeling</i>	56
4.2.1	General featuring's.....	56
4.2.2	LES modeling for single fluid flows	58
4.2.3	Spatial filtering of Navier-Stokes single-fluid model.....	58
4.2.4	Filtered Navier-Stokes equations for two-phase flows	59
4.3	<i>Fictitious Domain Method (FDM) for Obstacles and solid boundaries</i>	61
4.4	<i>Approximation of the turbulent single-fluid model</i>	63
4.4.1	Temporal discretization	63
4.4.2	The incompressibility constraint – The velocity-pressure coupling	65
4.5	<i>Spatial Integration</i>	69
4.6	<i>Interface Tracking Methods</i>	71
4.6.1	Interface tracking with reconstruction – VOF-PLIC.....	71
4.6.2	Capillarity effects Smooth Volume of Fluid - SVOF.....	72
4.7	<i>Conclusion</i>	73
5	Continuous Casting – Hydrodynamic Characterization.....	75
5.1	<i>Experimental Analysis</i>	77
5.1.1	Effect of water flow rate	77
5.1.2	Effect of oil layer viscosity.....	81
5.1.3	Effect of oil layer thickness	84
5.1.4	Conclusions	88
5.2	<i>Proposed configuration for mathematical modeling</i>	89
5.3	<i>Interface Characteristics</i>	90
5.4	<i>Mean Flow Description</i>	92
5.4.1	Water Oil Interface (WOI) configuration	92
5.4.2	Water Air (WFS) Configuration	96
5.5	<i>Turbulence Characterization</i>	101
5.6	<i>Turbulence implications on Mass Transfer Coefficients</i>	108
5.7	<i>Mass Transfer distribution at the liquid/liquid interface</i>	110
5.8	<i>Influence of process parameters on mass transfer coefficients</i>	112
5.8.1	Casting Speed	112

5.8.2	Slag viscosity.....	113
5.9	<i>Conclusions</i>	115
6	Liquid/Liquid Mass Transfer Experiments	117
6.1	<i>Liquid/Liquid Experiments</i>	117
6.1.1	Mass Transfer in a Ladle Model	119
6.1.2	Simplified liquid/liquid mass transfer experiments.....	121
6.1.3	Simplified liquid/liquid mass transfer modeling	125
6.1	<i>Conclusion</i>	129
7	Mass Transfer on an Industrial Configuration.....	131
7.1	<i>Continuous Casting – Industrial Configuration</i>	131
7.1.1	The mold	131
7.1.2	The Submerged Entry Nozzle (SEN)	132
7.1.3	The operational conditions	133
7.2	<i>CFD Model Results</i>	134
7.2.1	Hydrodynamic aspects	134
7.2.1	Mass Transfer Coefficient	135
7.3	<i>Conclusion</i>	138
8	Conclusions	139
9	References	143

Nomenclature

Latin letters

A :	area	m^2
C :	concentration	g/l
D :	mass diffusivity	m^2/s
F :	force	N
h :	depth, submersion, thickness	m
J :	mass flux	kg/m^2s
k :	mass transfer coefficient	m/s
K :	mass transfer constant	kg/l.s
L :	integral length scale	m
n :	normal vector	
p :	pressure	Pa
Q :	flow rate	m^3/s
t :	time	s
T :	integral time scale	s
u :	velocity vector	m/s
u :	velocity horizontal component	m/s
v :	velocity vertical component	m/s
V :	volume	m^3
w :	velocity perpendicular component	m/s
W :	width	m
x :	Cartesian horizontal direction	
y :	Cartesian vertical direction	

z : Cartesian perpendicular direction

Greek letters

γ :	surface divergence	s^{-1}
δ :	boundary layer thickness	m
ε :	energy dissipation	m^2/s^3
η :	Kolmogorov length scale	m
κ :	surface curvature	
μ :	molecular viscosity	Pa.s
ν :	kinetic viscosity	m^2/s
ρ :	density	kg/m^3
σ :	surface tension	N/m
τ :	shear stress	Pa
φ :	continuous field	
ψ :	vector field	
ω :	vorticity	
Ω :	delimitation of a domain	

Subscriptions and superscriptions

l : liquid

g : gas

o : oil

w : water

$i, 0$: initial

I : industrial process

int : interface

T :	transposed
t :	turbulent
m :	metal
p :	physical model
s :	slag
e :	equilibrium
∞ :	far field indication

Non-dimensional numbers

Fr :	Froude number
Re :	Reynolds number
Sc :	Schmidt number
We :	Weber number

Acronyms

BF :	blast furnace
BOF :	basic oxygen furnace
CC :	continuous casting
LEM :	large eddy model
MT :	mass transfer
MTM :	mass transfer model
SEM :	small eddy model
SEN :	submerged entry nozzle
WFS :	water free surface
WOI :	water oil interface
rms :	root mean square

List of Figures

Figure 1.1 - Flowchart of an integrated steel mill [1].	11
Figure 1.2 - Common hot metal pre-treatment scheme [3].	12
Figure 1.3 - A schematic view of an Electric Arc Furnace (EAF) [3].	13
Figure 1.4 - Basic Oxygen Furnace (BOF) scheme with inputs (blue) and outputs (red) [3].	14
Figure 1.5 - Ladle treatments commonly used in secondary steelmaking processes [4].	14
Figure 1.6 - Continuous Casting Machine [4].	16
Figure 1.7 - Bifurcated SEN.	17
Figure 1.8 - Schematic of continuous casting SEN and mold [9].	18
Figure 1.9 - Influence of mean velocity or turbulence fluctuation velocity near interface on metal-phase mass transfer coefficient by Ogawa and Onoue [13].	21
Figure 1.10 - Relationship between $k_w A$ and flow rate in terms of the order dependence, n , for center tuyere injection [14].	22
Figure 2.1 – Instantly images of the gas-liquid interface under different gas-side friction velocities. The wave crests are highlighted with white lines by Turney <i>et al</i> [20].	25
Figure 2.2 – Schematic diagram showing the mechanisms that may enhance the mass transfer in wavy interfaces, according to Peirson <i>et al</i> [21]. (a) Steep non-breaking wave. (b) A small-scale breaking wave with the additional processes introduced by breaking initiation.	26
Figure 2.3 – Examples of the wave conditions described by Peirson <i>et al</i> [21] (a) Low wave condition, wind speed 3.9 m/s; (b) Micro-scale breaking condition, wind speed 3.9 m/s. In each case the wind is from the right. The scales show centimeters at the top edge and inches at the lower edge.	26
Figure 2.4 – Coherent structures formation near a flat plate. (Perry <i>et al.</i> [24])	27
Figure 2.5 - Root-mean-square velocity fluctuations (u_{rms} , v_{rms} , w_{rms}), gas and liquid side, cases R29, R10, R1, and CH from Lombardi <i>et al</i> [16].	29
Figure 2.6 – Scheme of the film theory.	31
Figure 3.1 – Continuous Casting Water Model.	44
Figure 3.2 – CC water model and submerged entry nozzle (SEN) dimensions.	45
Figure 3.3 – The schematic diagram of LDA system [57].	47
Figure 3.4 - Laser beam reflection at the interface position.	49
Figure 3.5 - The main steps of the procedure: In (a) the extraction of the frames from the video, in (b) the isolation of the contours, in (c) the filtering of the noisy contours and in (d) the measure of the interface position.	50
Figure 3.6 – Rule placed to determine the pixel to cm conversion factor.	51
Figure 4.1 - Difference between the real domain (the physical one) and the fictitious domain (FDM).	62
Figure 4.2 - Finite Volume discretization - Control volume of u_x .	70
Figure 4.3 - Comparison of SVOF and VOF iso-surfaces by Pianet <i>et al</i> [59].	73
Figure 5.1- Schematic view of the water model configuration.	75
Figure 5.2 - LDA limit for the vertical velocity.	76
Figure 5.3 - Schematic view of the horizontal velocity profile with the boundary layer close to the interface. ...	77
Figure 5.4 - LDA measures of the horizontal component of the velocity field with Oil A (350 cSt). Mean values from the water flow rate $Q=1.6$ and $2.0 \text{ m}^3/\text{s}$ are presented in (a) and (b), respectively. The r.m.s. values are displayed at (c) and (d).	78
Figure 5.5 - LDA measures of the horizontal component of the velocity field with Oil B (20 cSt). Mean values from the water flow rate $Q=1.6$ and $2.0 \text{ m}^3/\text{s}$ are presented in (a) and (b), respectively. The r.m.s. values are displayed at (c) and (d).	79
Figure 5.6 - LDA measures of the vertical component of the velocity field with Oil A (350 cSt). Mean values from the water flow rate $Q=1.6$ and $2.0 \text{ m}^3/\text{s}$ are presented in (a) and the r.m.s. values are displayed in (b).	80

Figure 5.7 - LDA measures of the vertical component of the velocity field with Oil B (20 cSt). Mean values from the water flow rate $Q=1.6$ and $2.0 \text{ m}^3/\text{s}$ are presented in (a) and the r.m.s. values are displayed in (b).	80
Figure 5.8 - LDA measurements of the horizontal component of the velocity field with the lowest water flow rate, $Q = 1.6 \text{ m}^3/\text{h}$. Mean values from the configuration with oil viscosities $\nu = 20$ and 350 cSt are presented in (a) and the r.m.s. values are displayed in (b). No remarkable influence is found.....	82
Figure 5.9 - LDA measurements of the horizontal component of the velocity field with the highest water flow rate, $Q = 2.0 \text{ m}^3/\text{h}$. Mean values from the configuration with oil viscosities $\nu = 350$ and 20 cSt are presented in (a) and (b) respectively. The r.m.s. values are displayed at (c) and (d).	83
Figure 5.10 - LDA measurements of the vertical component of the velocity field with the lowest water flow rate, $Q = 1.6 \text{ m}^3/\text{h}$. Mean values from the configuration with oil viscosities $\nu = 20$ and 350 cSt are presented in (a) and the r.m.s. values are displayed in (b).	84
Figure 5.11 - LDA measurements of the vertical component of the velocity field with the lowest water flow rate, $Q = 2.0 \text{ m}^3/\text{h}$. Mean values from the configuration with oil viscosities $\nu = 20$ and 350 cSt are presented in (a) and the r.m.s. values are displayed in (b).	84
Figure 5.12 - LDA measures of the horizontal component of the velocity field with the lowest water flow rate, $Q = 1.6 \text{ m}^3/\text{h}$ with oil layer viscosity $\nu = 350$. Mean values from the configuration of 4 and 15 mm oil layer are presented in (a) and (b) respectively. The r.m.s. values are displayed at (c) and (d).	85
Figure 5.13 - Schematic view of the flow at the regions where the velocity measures were taken.	86
Figure 5.14 – Schematic view of the effects of oil layer thickness on the flows near the interface region where the LDA measures were performed.	86
Figure 5.15 – Velocity profiles and rms for different oil layer thickness. The water flow rate is $Q = 2.0 \text{ m}^3/\text{h}$ and the oil viscosity is $\nu = 350 \text{ cSt}$	87
Figure 5.16 – LDA measures of the vertical velocity components, V , with different oil layer thickness for $1.6 \text{ m}^3/\text{h}$ (a-b) and $2.0 \text{ m}^3/\text{h}$ (c-d) water flow rate and oil layer viscosity $\nu = 350 \text{ cSt}$	88
Figure 5.17 - Physical apparatus with the indication of the LDA measurement position and a schematic view of the average flow pattern in CC mold.	90
Figure 5.18 – Normalized spectrum of the interface displacement in the WOI configuration. Figures (a) and (b) concern the interface displacement in the experimental model. Figures (c) and (d) show the interface displacement in the mathematical model.	91
Figure 5.19 - Velocity field of the WOI experiment vs CFD at 3.5 cm from the SEN. (a) shows the streamwise component and its rms values are displayed in (b).	93
Figure 5.20 - Velocity field of the WOI experiment vs CFD at 7.0 cm from the SEN. (a) shows the streamwise component and its rms values are displayed in (b).	93
Figure 5.21 - Velocity field of the WOI experiment vs CFD at 3.5 cm from the SEN. (a) shows the vertical component and its rms values are displayed in (b).	94
Figure 5.22 - Velocity field of the WOI experiment vs CFD at 7.0 cm from the SEN. (a) shows the vertical component and its rms values are displayed in (b).	94
Figure 5.23 - Normalized velocity profiles.	95
Figure 5.24 - Velocity field of the WFS configuration at 3.5 cm from the SEN. (a) shows the comparison between the CFD and the LDA values of the streamwise component (b) the comparison of the rms values.	96
Figure 5.25 - Velocity field of the WFS configuration at 7 cm from the SEN. (a) shows the comparison between the CFD and the LDA values of the streamwise component (b) the comparison of the rms values.	97
Figure 5.26 - Velocity field of the WFS configuration at 3.5 cm from the SEN. (a) shows the comparison between the CFD and the LDA values of the vertical component (b) the comparison of the rms values. ..	97
Figure 5.27 - Velocity field of the WFS configuration at 7 cm from the SEN. (a) shows the comparison between the CFD and the LDA values of the vertical component (b) the comparison of the rms values.	98
Figure 5.28 – Scheme of the instantaneous flow and the origins of the low velocities at the interface of the WFS configuration. (a) the front view and (b) the perpendicular view.	99
Figure 5.29 – Instant vector field of the WFS simulation. The front view is shown in (a) and a perpendicular view is shown in (b). The non-zero values of the velocity field are identified by the vectors in red touching the water/air interface.	99
Figure 5.30 – Averaged velocity profiles of the WFS configuration	100

Figure 5.31 - Normalized velocity profiles.	100
Figure 5.32 - Spectral signal of the LDA in (a), the experimental interface displacement in (b) and the CFD interface displacement in (c).....	102
Figure 5.33 - Superposition of the normalized spectrum signal of the velocity measured at each point of a velocity profile.....	102
Figure 5.34 - Brut signal and its different components in (a) and the different filters applied to the RMS profile of the horizontal component of the WFS configuration at 7cm from the SEN.....	103
Figure 5.35 – rms profile after filtering the low frequency fluctuation values.....	104
Figure 5.36 – Normalized rms velocities of WOI (a and b) and WFS (c and d) in the liquid-side.	105
Figure 5.37 - Normalized turbulence intensities of WOI (a and b) and WFS (c and d) in the upper phase-side.	106
Figure 5.38 – Evolution of the Kinetic energy (a) and (c) and the energy dissipation (b) and (d) close to the WOI and WFS.	107
Figure 5.39 - Prediction of mass transfer coefficients, k [m/s], in a CC water model. Results in (a) are calculated by Large Eddy Model and in (b) by Surface Divergence Model.....	111
Figure 5.40 – CFD mass transfer coefficient at the WOI for a water flow of 1.6 m ³ /h (a) and 3.0 m ³ /h (b). The images show the average values over 10 seconds.	113
Figure 5.41 – CFD mass transfer coefficient at the WOI for an oil layer viscosity of 20 cSt (a) and 350 cSt (b). The images show the average values over 10 seconds.	115
Figure 6.1 – The experimental work of Kim <i>et al</i> [14] showing the variation of $K_w A$ as a function of gas flow rate for central tuyeres injection.	118
Figure 6.2 - Scheme of the dimension of Kim's experiments.....	119
Figure 6.3 - Relationship between L.H.S. of mass transfer Eq. (6.6) and time from Kim <i>et al</i> [14].....	121
Figure 6.4 - Physical model used to perform the mass transfer experiments	122
Figure 6.5 - Light Refractometer used to measure thymol concentration from samples in trials.....	122
Figure 6.6 - LHS evolution in our experiments.....	123
Figure 6.7 – Mass transfer measured in different gas flow rates.....	124
Figure 6.8 – The mesh used during the simulations. (a) the top view, (b) the front view and (c) an isometric view.	125
Figure 6.9 – Experimental and numerical open-eye size measurement.	126
Figure 6.10 - Comparison between CFD and experimental average open-eye diameters.....	127
Figure 6.11 - Comparison of the mass transfer parameter measured and calculated from CFD.	128
Figure 6.12 - Water/oil interface predicted by our CFD model. The gas flow of this simulation is 0.5 l/min. The interface is colored by the calculated mass transfer coefficient.....	129
Figure 7.1 - CC industrial configuration. The simulated domain (half of a complete geometry) was reduced to diminish computational time.	132
Figure 7.2 - SEN geometry defined in Thetis by the FDM.	133
Figure 7.3 - Horizontal Velocity component profile at different distances from the SEN (30, 50, 60 cm).....	135
Figure 7.4 - Mass Transfer Coefficient distribution at a liquid steel/slag interface ($Sc = 1 \times 10^3$). Values averaged over 30s.	136
Figure 7.5 – Averaged velocity profile at the symmetry plane of the CC mold. The upper loop touches the interface at the same position where the higher mass transfer coefficients were observed.	136
Figure 7.6 - Measured and predicted MnO content of slags in a CC machine during the casting of a free-machining steel. Work presented by Chaubal et al [94] [102].....	137

1 Introduction

In the steel industry, every step of the production of high quality steels involves the transfer of impurities or undesired elements present in the liquid metal to the slag. This process is performed by transferring chemical species through the steel-slag interface. For this reason, the mass transfer between liquid metal and slag is of major importance for steelmakers.

In this chapter, we are going to briefly describe the steel production chain, showing where and how mass transfer takes place in each process of a common steelmaking facility. Mass transfer experiments are commented and results of mass transfer correlations are shown at the last part of this chapter. Then, the objectives of this thesis are set. The next chapter will provide further mass transfer and fluid flow theories, which are the bases for our discussion. Chapter three and four will describe the experimental and numerical models, respectively. The results and discussions of the work are presented in chapter's five to seven.

1.1 Steelmaking Processes and Mass Transfer

In an integrated steel mill the steel production begins with the reduction of the iron ore through many chemical and physicochemical reactions, from the sintering and pellet plants to the blast furnaces, where the sources of iron are reduced and melted to produce hot metal and slag. Figure 1.1 shows schematically the layout of a typical steel mill.

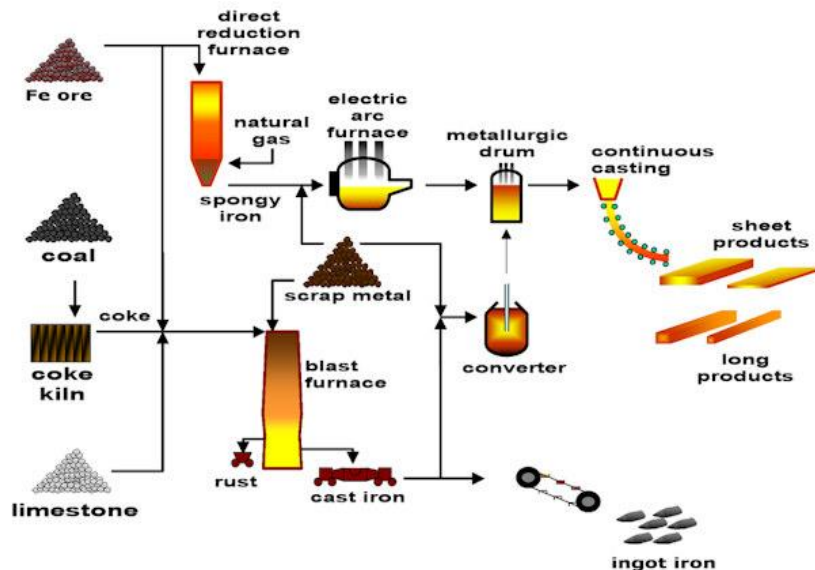


Figure 1.1 - Flowchart of an integrated steel mill [1].

The hot metal produced in the blast furnace (BF) is a liquid alloy with approximately 94% Fe content, 4% C content and 1% of other elements such as Si, Mn, Mg, Al, S and P, varying according to the raw materials used and operational conditions during its production. Inside the BF, the sulfur, generally provided from metallurgical coals, is dissolved in the hot metal and later, a small amount of it is removed by the slag formed. Here, the mass transfer occurs in the hot metal/slag interface inside the BF. Other elements from the raw materials, such as Al, Mn, Mg, P are also incorporated to the hot metal inside this reactor.

After the reduction, the cleaning process of the hot metal, commonly called *refinement* or *pre-treatment*, starts with the desulfurization and/or dephosphorization and desilicication [2] which consists of reducing the sulfur, phosphorus and silicon content before starting the steelmaking process itself. These procedures can be made in a ladle or in a torpedo car (Figure 1.2). During the hot metal refinement, fluxes are added as sources of calcium (CaO) and magnesium (MgO) to form a slag with the appropriate characteristics to dissolve, capture and react with the liquid metal bath which is stirred by gas injection or mechanically stirred.

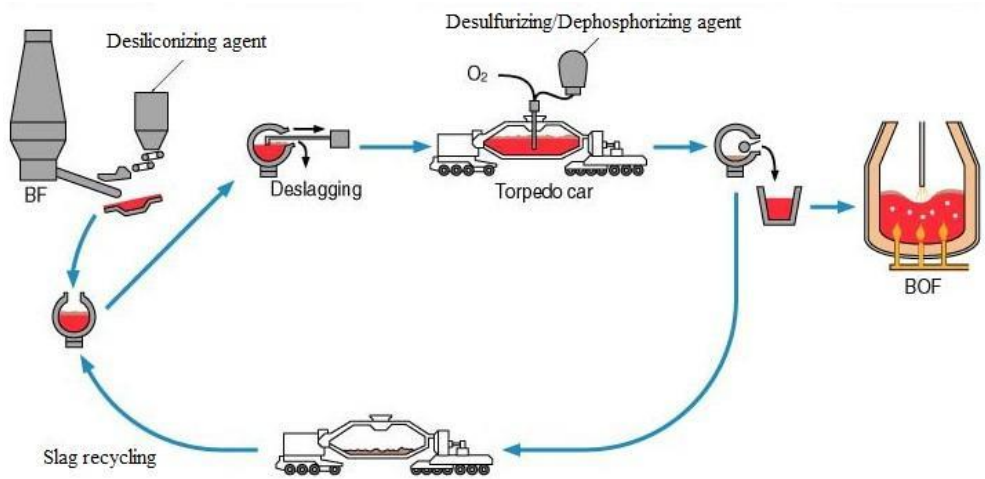
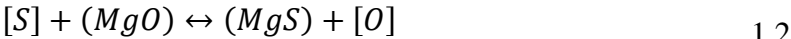


Figure 1.2 - Common hot metal pre-treatment scheme [3].

The reaction for desulphurization occurs between basic oxides from the slag and dissolved sulfur, according to Eq. (1.1) and (1.2)



Where the elements in [] are dissolved in liquid metal and the ones in () are dissolved in the slag. In this case, the mass transfer at the interface between hot metal and slag is very important to control the time of reaction to achieve the composition desired by the steelmakers.

Once the hot metal composition is adjusted, it is taken to the steelmaking facility, where the liquid iron is transformed into liquid steel by removing its dissolved carbon. It is considered as steel any ferrous alloy with less the 2.11%wt of carbon content and iron as its major component. Commercially steels are divided in three main groups, according to its carbon content; Low Carbon ($\%C_{wt} < 0.30$), Medium Carbon ($0.30 < \%C_{wt} < 0.6$) and High Carbon ($0.6 < \%C_{wt} < 1.0$).

The steel can be produced in Electric Arc Furnaces (EAF - Figure 1.3), or in Basic Oxygen Furnaces (BOF - Figure 1.4).

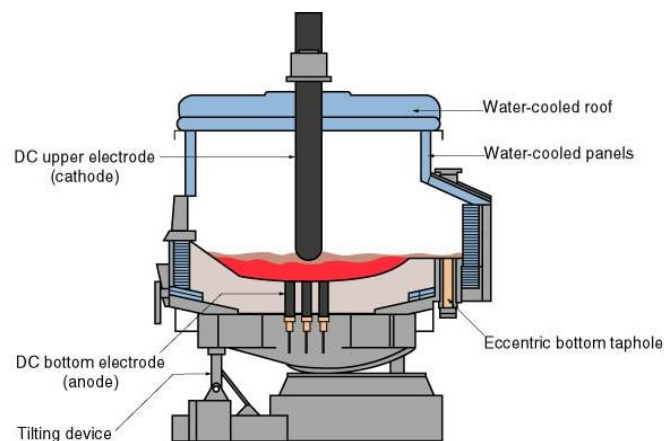


Figure 1.3 - A schematic view of an Electric Arc Furnace (EAF) [3].

The BOF is filled with liquid hot metal (and often with steel scrap for cost optimization) and fluxes are added to form slag to promote the removal of the oxides formed during the tapping. Oxygen is injected through a vertical lance during the heating to react with the carbon present in the hot metal charged, forming CO and CO₂ as shown in Figure 1.4. The oxygen also reacts with other elements dissolved in the bath, such as silicon, aluminum, magnesium, sulfur, phosphorus and even the iron. The oxides formed from these reactions can remain in the liquid steel bath forming the harmful inclusions or affecting the composition and physical properties of slag if they are entrapped by it.

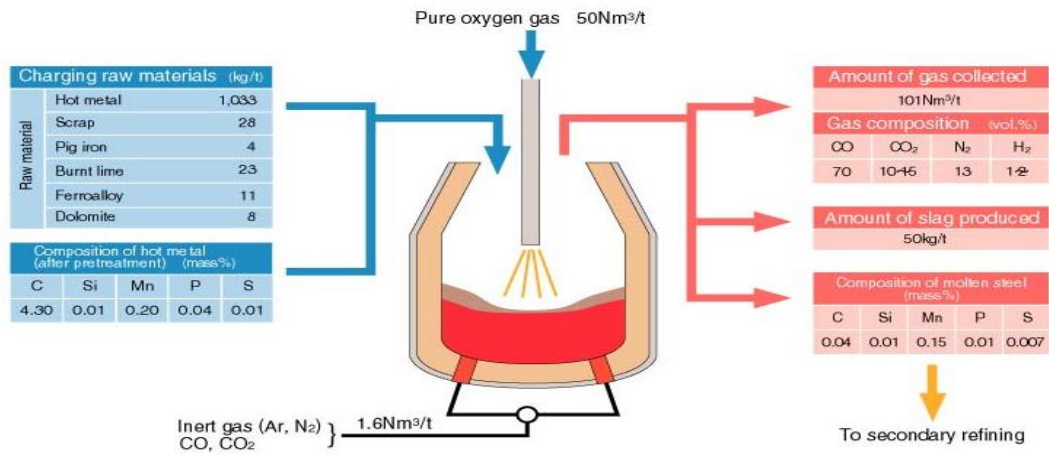


Figure 1.4 - Basic Oxygen Furnace (BOF) scheme with inputs (blue) and outputs (red) [3].

After the BOF, the steel may need a composition adjustment or a second refinement. These procedures are usually performed in ladle treatments and vacuum vessels, and are called *Secondary Steelmaking Operations*.

During the ladle treatment, the steel is delivered into a ladle which may be stirred in order to achieve an homogeneous composition and temperature, ensure good slag-metal interactions, essential for desulfurization and alloy dissolution, and to accelerate the removal of inclusions in the steel. In practice, stirring is achieved by argon bubbling through the liquid steel, either via a submerged lance, by porous plugs in the bottom of the ladle, or electromagnetic stirring (EMS) (Figure 1.5).



Figure 1.5 - Ladle treatments commonly used in secondary steelmaking processes [4].

A slag layer is present on the steel surface and has the function of protecting the steel against atmosphere contact to avoid steel oxidation and heat losses, promoting inclusion removal as

well as steel refinement. Alloys can be added to adjust chemical composition according to future steel application. Ogawa *et al* [5] have shown, by water model and plant scale experiments, the strong influence of mass transfer on efficiency in this process.

In all these processes, the mass transfer plays an important role, since all the treatments are achieved through mass transfer between the different phases. However, all the previous processes involve high complex phenomena and high turbulence level, which makes the computations of such domains very time consuming or unfeasible with the current computational resources. Instead, the continuous casting has a lower complexity level and keeps all the phenomena we are interested in the present study; the turbulent multiphase flow and mass transfer at the steel-slag interface. The continuous casting will be described with more details in the next section.

1.2 Continuous Casting

Once the steel cleanness and composition are well adjusted, it is solidified to form the billets, blooms or slabs. Nowadays, the Continuous Casting (CC) machine is the most used casting process because of its high productivity, yield, and possibility of achieve high superficial and internal quality level. It has the capacity and versatility to cast different grades of steels without the need of stopping the process.

The steel is delivered to the CC machine in ladles. The CC machine is composed of three main reactors:

- The ladle;
- The tundish;
- The mold.

Figure 1.6 shows schematically one of these installations.

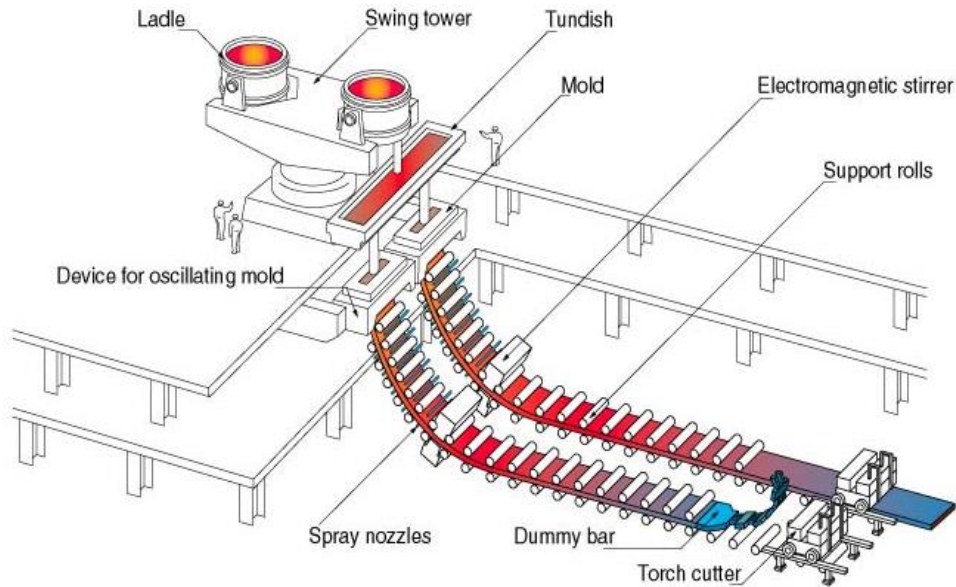


Figure 1.6 - Continuous Casting Machine [4].

In the CC, the ladle has, first of all, the role of transporting the liquid steel to the CC machine, as well as to serve as a pot of liquid steel during the casting.

The tundish is an intermediate reactor between the ladle and the mold. It is a reservoir that allows the steel to flow at a controlled rate to the copper mold and ensure the feeding of the molds during the ladle changing. By using some flow modifiers it is also possible to capture the inclusions that remained in the steel and improve the cleanness level of the steels. The tundish can also be used to control temperature oscillations and to perform some chemical homogenization.

The mold is usually considered as the most important component of a continuous casting machine, where the heat extraction and solidification take place. The steel is injected into the mold through the submerged entry nozzle (SEN). According to Thomas [6], the required characteristics for a good SEN are:

- To be able to create a good flow pattern into the mold;
- To be resistant to wear, shear stresses and thermal shock;
- To have a low porosity level and competitive cost;

There are many different types of SEM. For the continuous casting of slabs the most commonly used are the bifurcated ones, as shown in Figure 1.7:



Figure 1.7 - Bifurcated SEN.

These valves have some characteristics that must be adjusted, since the steel flow is directly affected by their configurations. Some of these variables are the SEN immersion and the geometry of the outlet of these SEN's. The casting speed and the width of the slab also have a direct relation with the liquid flow inside the mold and are parameters that must be taken into account during the SEN selection.

During the casting, a flux powder is continuously poured on the liquid steel surface, forming a liquid pool which flows through the mold walls reducing the friction between the solidified shell and the mold walls. This powder has among its different tasks [6] [7] [8]:

- The lubrication between the solidified steel shell and the mold walls, minimizing the occurrence of breakage of the solidified shell during the casting (break out). The lubrication ability of the slag is determined by its viscosity and liquidus temperature;
- The thermal insulation of the liquid steel, preventing its solidification on the mold surface;
- Prevention against re-oxidation, avoiding the contact of the liquid steel with the oxidant atmosphere;
- Inclusion removal. This property depends on the chemical composition of the mold flux;
- Control of the heat transfer between mold and liquid steel, also determined by its viscosity, liquidus temperature and chemical composition. The occurrence of non-uniform heat transfer can contribute to crack formation.

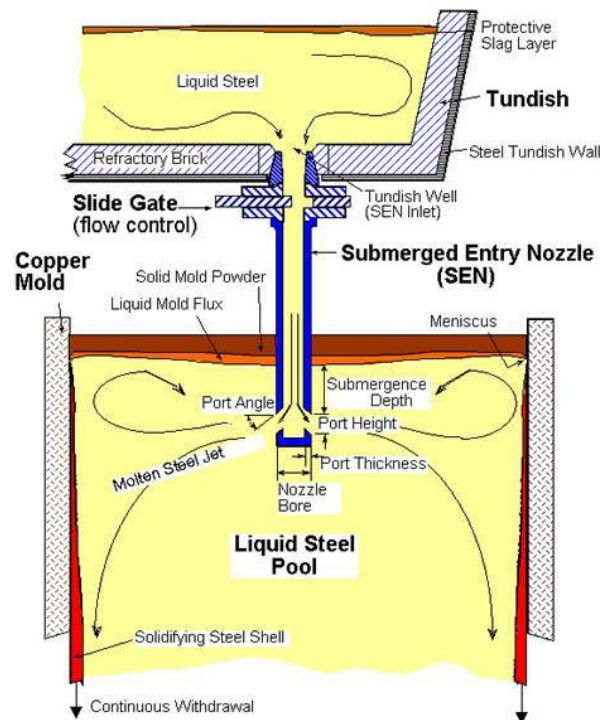


Figure 1.8 - Schematic of continuous casting SEN and mold [9].

The liquid steel and the liquid mold flux (the slag) are immiscible. In the mold, because of its lower density, the mold flux stays above the liquid steel. The movement of the liquid steel modifies the shape of the interface, which means that the interface between liquid steel and slag is not flat, as schematically shown in Figure 1.8.

The velocity of the fluids must be the same at the interface and this makes the velocity field of the liquid steel to impose a velocity to the liquid mold flux at the interface. Since the viscosities of the liquids are different, the imposition of a velocity by the steel generates a shear stress at the interface. When the shear stress is stronger than the surface tension it can detach the slag from its layer and drag it into the steel, generating new inclusions that will contaminate the produced steel.

As previously mentioned at the end of section 1.1, the continuous casting was chosen to study the mass transfer and multiphase flow in the steelmaking because of its relative low complexities and the possibility to find all the phenomena involved in multiphase flows for the different steps of steel production.

1.3 Mass Transfer in Steelmaking

The productivity of steelmaking processes, including production and refining of liquid steel, depends on the mass transfer rates. Due to the high temperatures involved in the processes, the rate controlling step of the processes is usually a mass transfer phenomenon [10]. In steelmaking operations, different situations of mass transfer can occur, depending on the phases involved:

- Liquid-liquid mass transfer, in the case of reactions involving liquid steel and slag;
- Liquid-gas mass transfer, when a gas is injected into or onto liquid steel;
- Liquid-solid mass transfer, when solid particles are injected into liquid steel to promote refining reactions and alloy additions.

In all these situations, the characterization of the mass transfer coefficients and the parameters that interfere on its value is a very important task to optimize the process and improve productivity.

The first step to determine the mass transfer coefficient is the modeling of the flow of the different phases to determine the mass flux based on the concentration gradients. Far from the interface, turbulent mixing ensures that the bulk concentrations remain largely uniform and spatial concentration gradients remain small. As approaching to the interface, turbulence activity is damped and the description of a species concentration C with molecular diffusivity D is governed by the advection diffusion equation:

$$\frac{\partial C}{\partial t} + u \cdot \nabla C = \nabla \cdot J \quad 1.3$$

$$J = D \nabla C \quad 1.4$$

This mass transfer occurs concomitantly with momentum transfer. Thus the velocity field must also be predicted. For complex $3D$ flows the Navier-Stokes and mass conservation equations are resolved and then the mass transfer coefficient is estimated.

In steelmaking processes, the mass transfer coefficient is usually obtained by curve fitting experimental data. Variations of concentration of a certain component as a function of time are predicted and compared to experiments; subsequently, a mass transfer coefficient that leads to the best agreement between experimental data and theoretical predictions is determined [11]. Due to the costs and complications of performing test with liquid steel, water models can be used to investigate mass transfer rates.

The mass transfer rate in a BOF was studied by Singh *et al* [12]. They used a physical model to find the best bottom stirring configuration by adjusting the tuyeres gas flow rates. They used different oils to simulate slag. The distribution coefficient of benzoic acid was determined in a typical mass transfer experiment in lab to use it as the exchange material in the water/oil system. They monitored the benzoic acid concentration in water during the experiments and assumed the mass transfer between the two fluids to be of first order and used the following equation to calculate the mass transfer rate constant:

$$\ln \frac{(C_t - C_e)}{(C_0 - C_e)} = kt \quad 1.5$$

Where k is the mass transfer constant [$\text{gL}^{-1}\text{min}^{-1}$], which is related to the mass transfer coefficient, C_e is the equilibrium concentration of the exchange material in water [gL^{-1}], C_t is the concentration of the exchange material in water after time t [min], and C_0 is the initial concentration of exchange material in water [gL^{-1}].

This simple approach yields to an improved BOF performance in terms of phosphorous removal by adjusting the tuyere flow rate configuration. However, the authors did not confirm if the 30% enhancement in mass transfer rate between slag-metal, expected from physical experiments, was achieved in plant trials.

Ogawa and Onoue [13] studied the mixing time and slag-steel mass transfer coefficient in gas bubbling and induction stirred ladle with a water model and plant scale experiments. They added a constant volume of foaming polystyrol particles coated with KCl or foaming alumina particles coated with benzoic acid to the surface of the water model and continuously measured the change in concentration of KCl or benzoic acid in water. The metal-phase mass transfer coefficient was considered to be determined by Eq.(1.6) and it was calculated by Eq.(1.7) and the interfacial area, A , was measured from photographs taken under each experimental condition.

$$\frac{\partial C}{\partial t} = K_m \frac{A}{V} (C_s - C) \quad 1.6$$

$$\ln(1 - C/C_s) = -K_m \frac{A}{V} t \quad 1.7$$

They also measured in a water model, the mean velocity and turbulence fluctuation near the interface with a hot film anemometer. They showed that the metal-phase mass transfer coefficient is determined with the turbulence fluctuation velocity rather than mean velocity

(Figure 1.9). Therefore, processes having high turbulence near the slag-metal interface, for example, gas bubbling treatments, have a superior mass transfer coefficient.

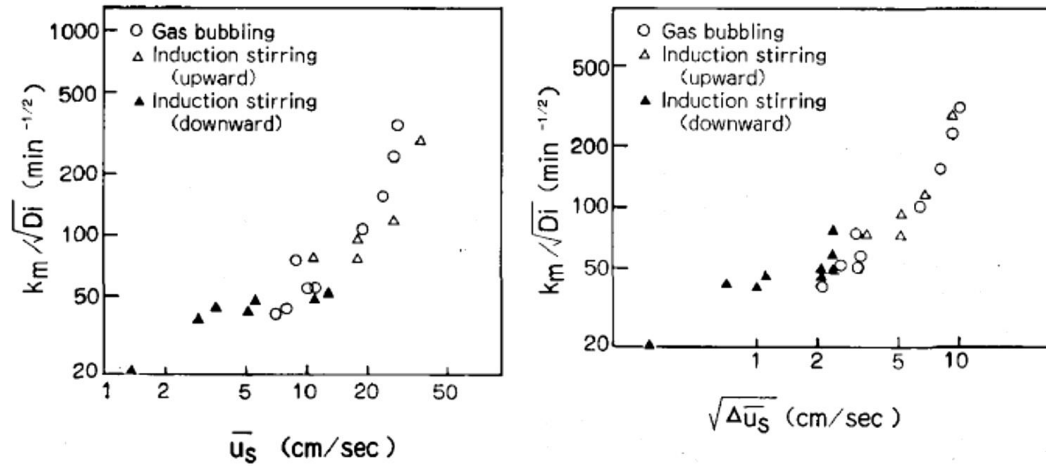


Figure 1.9 - Influence of mean velocity or turbulence fluctuation velocity near interface on metal-phase mass transfer coefficient by Ogawa and Onoue [13].

The dependence of mass transfer on hydrodynamic regimes was also studied by Kim and Fruehan [14] in a cold model of a gas stirred ladle. They simulated the desulphurization by using thymol ($\text{C}_{10}\text{H}_{14}\text{O}$) as a tracer, water to simulate liquid steel and a solution of paraffin oil and cottonseed oil in a 50/50 volume proportion to simulate slag. In the oil solution, the partition ratio of thymol is higher than 350, while the sulfur in a typical liquid slag on ladle treatment is about 200 to 500. The mass transfer is then controlled by metal or water resistance. The diffusivity of Thymol in these systems is about $6.8 \times 10^{-10} \text{ m}^2/\text{s}$, which is in the same range of chemical species such as sulfur and aluminum in liquid steel.

They observed three different regimes to the mass transfer, according to the gas flow rate in the configuration of central nuzzle (Figure 1.10):

Low gas flow rate (Regime I) - In this first regime, the mass transfer is a weak function of the gas flow rate, where $k_w A$ (k_w is the mass transfer parameter and A is the interfacial area) has a 0.6 order dependence on the water flow rate. In this configuration, the oil layer is very calm, no oil droplets are driven into the water, and the interface between oil and water phases is close to planar surface except for the very weak wave motion of the interface near the edge of plume eye.

Intermediate gas flow rate (Regime II) - At this stage, where the gas flow rate is about 4.5 to 9.0l/min, the product $k_w A$ has an order dependence of 2.5 on the gas flow rate. This high

value and the abrupt change of the dependence can be explained by the observation that the oil layer near the edge of a plume eye continuously forms oil ligaments and then breaks up into droplets which are entrained into the water.

High gas flow rate (Regime III) - At this higher gas flow rate region, the $k_w A$ is proportional to $Q^{1.43}$ (where Q is water flow rate), and nearly the entire oil layer breaks down into oil droplets without forming oil ligaments near the edge of plume eye right after gas injection, and the penetration of oil droplets deep into the water bath occurs.

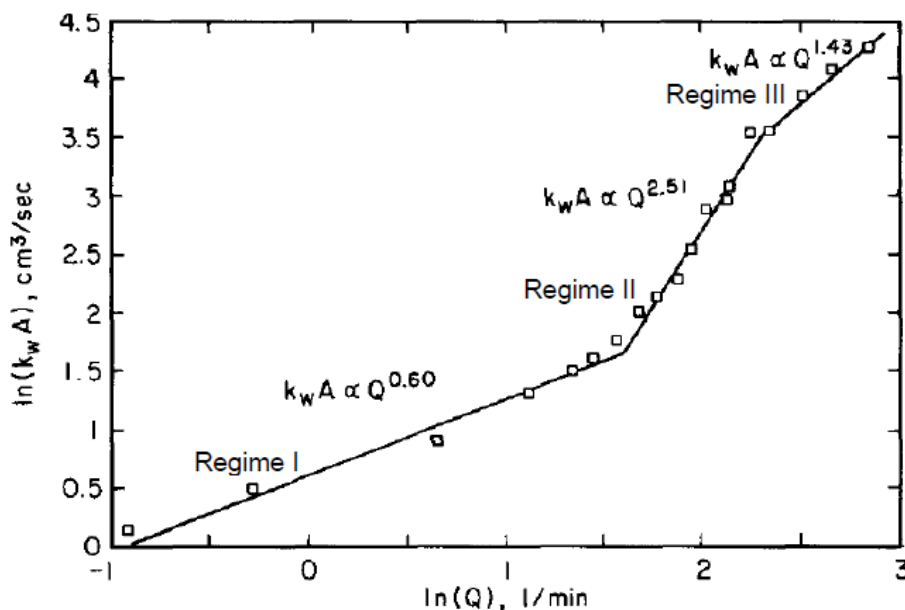


Figure 1.10 - Relationship between $k_w A$ and flow rate in terms of the order dependence, n , for center tuyere injection [14].

These works illustrate the strong dependence of the mass transfer on the hydrodynamics. Unfortunately, the correlation for $k_w A$ is totally linked to the set-up and there is no methodology to extrapolate the results to the real process, due to the fact that the interface morphology is depending both on the momentum impulse brought by the bubble plume and the resistance to interface deformation resulting from the interfacial tension. There is no similarity criteria respecting the two mechanisms, and it is not possible to predict such dependence between mass transfer and gas flow rate for industrial processes.

1.4 Objectives

To increase the accuracy of the mass transfer modeling, it is necessary to switch from a global approach to a local one. For a local approach, the starting point should be the determination of a correct correlation for the mass transfer coefficient. Many methods can be used for that purpose, most of them derived from two main theories; the surface renewal theory and the surface divergence theory. These models are detailed in Chapter 2. The focus of the present work is to derive an equation to locally predict the mass transfer coefficients of chemical species in a steelmaking environment, with high density and viscosity ratios at the interfaces, high interface/surface tension and very high Schmidt number. The starting point will be a comprehensive characterization of the hydrodynamics close to a sheared liquid-liquid interface in both, a CC water model and a CFD simulation of these experiments. Latter, we will implement the models created to gas-liquid mass transfer in the code used in this work. Finally we will evaluate and adapt these models to predict the liquid-liquid mass transfer coefficients and apply them to an industrial case.

2 Mass Transfer and Fluid Flow near the Interface Region

2.1 Turbulence interactions in Multiphase Flows

The previous section described some interactions between the bulk flow and interface that may locally change the interface properties and its shape. We are going to discuss about the effects of turbulent flows near the interface region and its implications on mass transfer.

For a more detailed discussion, it is important to start by analyzing where the turbulence is produced, and two main cases may occur [15]. The interface may have a free slip condition, which happens in channel flows when the turbulence is produced far from the interface, at the channel bottom, with no-slip condition, and brought to the interface. A second configuration is found in studies considering multiphase flows in tanks, lakes or sea, where the wind flows over the liquid-gas interface. When sufficiently high speed winds flow over a free surface, they can generate waves due to the shear imposed on the surface [15].

Studies like those from Lombardi *et al* [16], Banerjee *et al* [17], Lin *et al* [18] and Komori *et al* [19] verified that for the air-water cases, the turbulence characteristics at the gas side are fairly similar to those near the wall, being damped at the vicinity of the interface. The same behavior is not observed at the liquid side, where the velocity fluctuations are high near the interface [19].

Later, Turney *et al* [20], by investigating the turbulence structures at the liquid side of the gas-liquid interface and its effect on the mass transfer, verified that the friction velocity at the interface of the gas side should be inferior to 0.1 m/s to avoid the formation of waves on the liquid interface. In this research field, it is customary to relate the friction velocity to the wind velocity 10 m above the interface, which can be easily measured. The maximum friction velocity suggested corresponds to a wind velocity at 10 m of about 3.5 m/s. The perturbations that may occur at the liquid interface due to the wind shear are of two types; (i) small perturbations, capillary waves, or ripples, which main characteristics are low amplitude and wave length and high frequency, and (ii) large perturbations, disturbance waves, which characteristics are high amplitudes, large wave length and frequencies lower than the capillary waves. This transition from a plane surface, with small perturbations can be seen in Figure

2.1, from Turney *et al* [20]. The existence of waves at the interface favors the turbulence generation and structures characteristics of this flow regime.

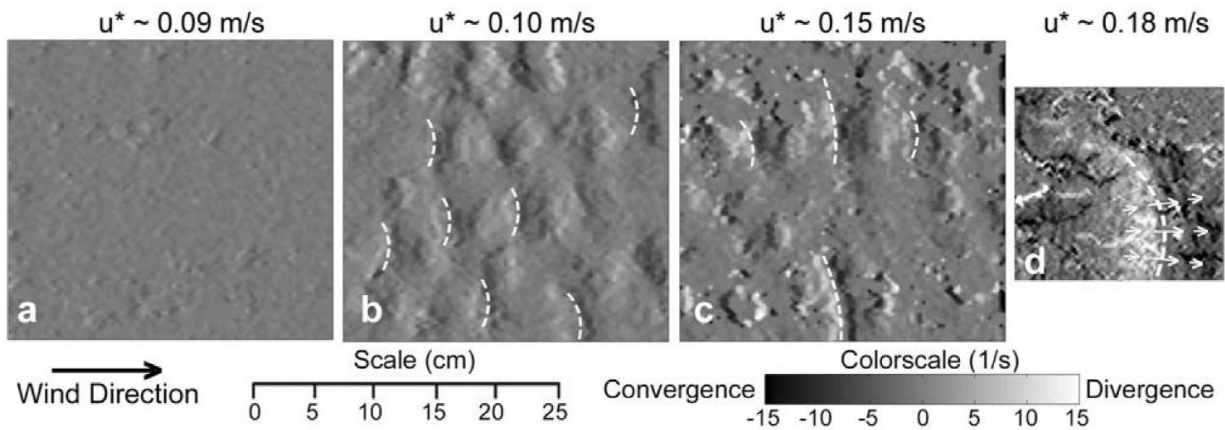


Figure 2.1 – Instantly images of the gas-liquid interface under different gas-side friction velocities. The wave crests are highlighted with white lines by Turney *et al* [20].

Peirson *et al* [21] made a literature survey to identify the movements close to the interface which may occur with the gas-liquid surface deformation and enhance mass transfer. Figure 2.2 shows some of the processes that may occur at the proximity of the gas-liquid interface. He identified five processes, which may be interdependent in some cases, and which control the mass boundary layer that provides the driven force for mass transfer. One of these is the surface divergence, as mentioned before, and the regions of surface renewal, where the fluid is replaced by fluid portions coming from the bulk of the flow, brought by turbulent vortices. They pointed out the capillary waves as well. These waves have high vorticity and are very important for the fluid renewal at the interface.

Another effect which can be seen at the interface region at Figure 2.2 (b), where the wave crest is projected forward and overpasses the wave front, recirculating in an opposing direction to the flow, caring with it the surface region and creating a high turbulence region. In this case, micro-scale wave braking may occur.

Figure 2.3 (a) and (b), from Peirson *et al* [21], are examples of these two wavy categories. The first one is related to the scheme showed in Figure 2.2 (a), and for this case the friction velocity is 0.24 m/s. Figure 2.3 (b), where the friction velocity of the gas phase is equal to 0.42 m/s, show a case where there is a micro-scale wave braking, related to Figure 2.2 (b).

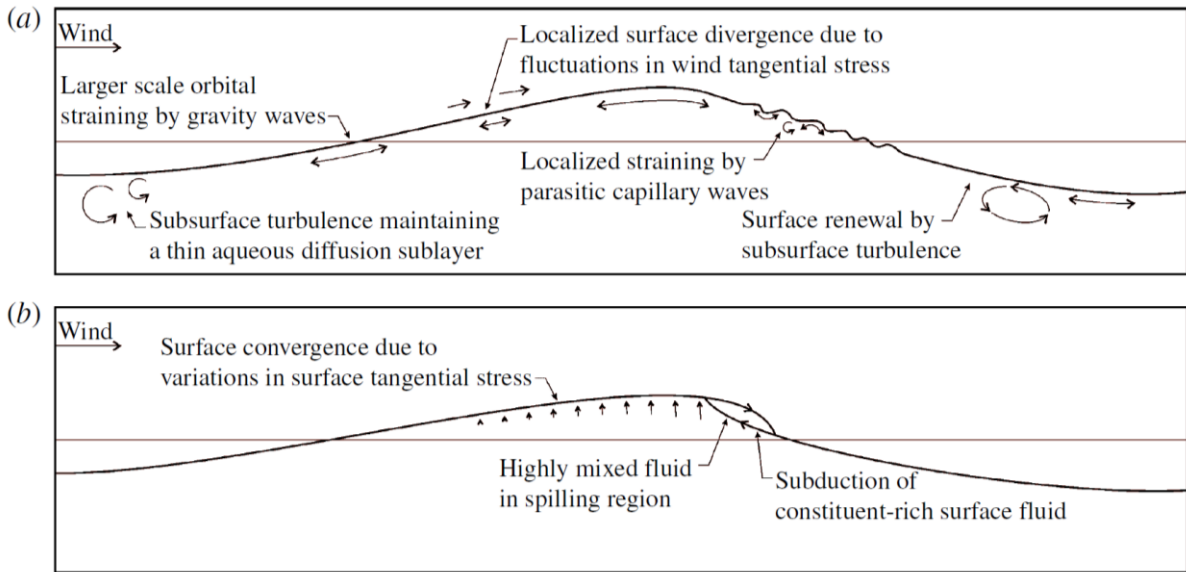
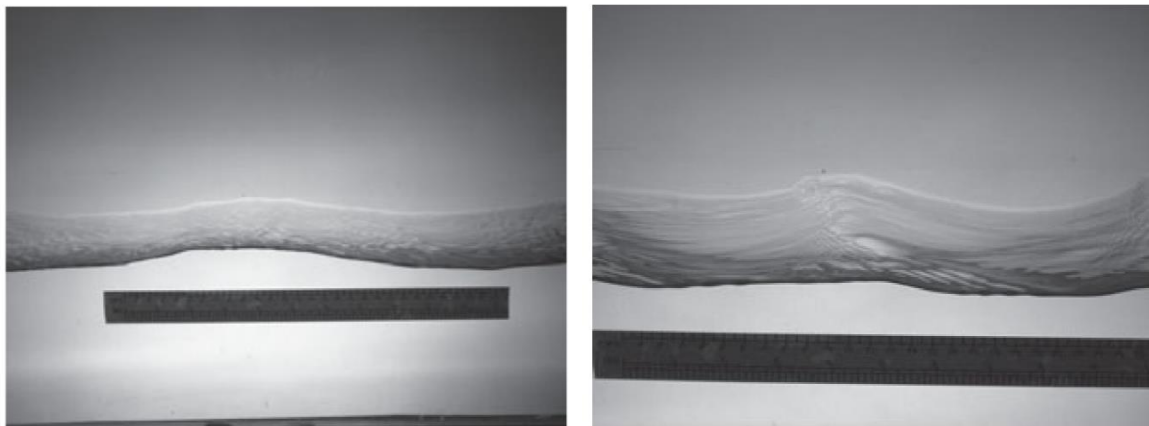


Figure 2.2 – Schematic diagram showing the mechanisms that may enhance the mass transfer in wavy interfaces, according to Peirson *et al* [21]. (a) Steep non-breaking wave. (b) A small-scale breaking wave with the additional processes introduced by breaking initiation.



(a) (b)

Figure 2.3 – Examples of the wave conditions described by Peirson *et al* [21] (a) Low wave condition, wind speed 3.9 m/s; (b) Micro-scale breaking condition, wind speed 3.9 m/s. In each case the wind is from the right. The scales show centimeters at the top edge and inches at the lower edge.

Kline *et al* [22] showed large structures of the turbulent flow that had not been observed by the scientific community until the 60's. This concept gave birth to new investigations in the sense of not treating the turbulence as a random movement, but rather considering the dominant *coherent structures*.

The concept of coherent structures may vary in literature but they are basically defined as movements of the flow with a characteristic length and which duration may persist for more

than a characteristic time period, contributing to the investigated process (such as matter transport and/or mix and momentum and/or energy transfer), and which are distinguishable from random movements in the flow [23]. They may have space organization and last sufficiently long to be captured in a recorded visualization of the flow (in an experiment) and/or significantly contribute to the average statistics of the flow.

We can see in Figure 2.4 the turbulent structures formation in an experiment of Perry *et al* [24] in an investigation of the turbulence in a plate. This picture shows the transition between the laminar and turbulent regimes. The first structures that are formed are what they called of Tollmien-Schlichting structures. These waves start to oscillate in the transverse direction of the flow and originate the streamwise vortices which depending upon its form are called *hairpin vortices*. These instabilities are turbulent counter-rotating strands that emerge from the interior of the boundary layer. The presence of these counter-rotating vortices suggests the formation of streaks of low and high velocity. As a consequence of the instabilities of these streamwise vortices which emerge from the wall, there is a rupture originating the bursts and finally its degeneration in a developed turbulence. The turbulent explosions consist of an ejection process of low velocity fluid from the wall and a sweep of high velocity fluid at the wall (see Venditti *et al* [23]). In summary, we can describe the coherent structures near a wall-bounded turbulent flow as velocity streaks and streamwise vortices which are tri-dimensional structures.

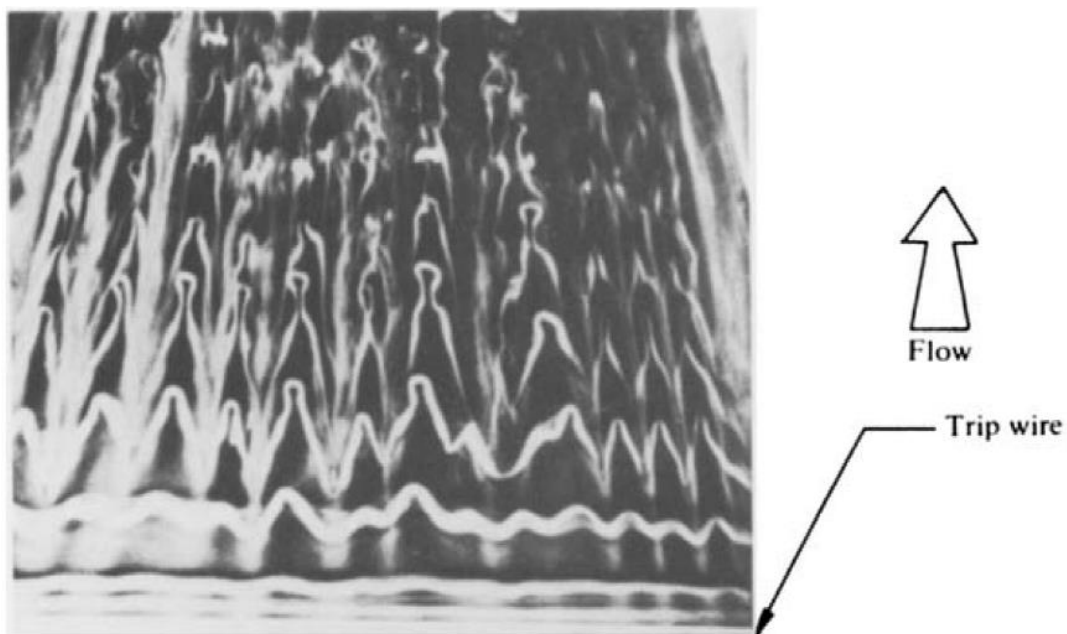


Figure 2.4 – Coherent structures formation near a flat plate. (Perry *et al.* [24])

Many experiments and numerical simulations (Lombardi *et al* [16], Magnaudet and Calmet [25], Lin *et al* [18], Hasegawa and Kasagi [26], Komori *et al* [19], Turnay and Banerjee [27], Takagaki *et al* [28]) have been performed focusing only in the presence and development of turbulent structures at the interface region.

According to Banerjee and Macintyre [17], the key question is to know if these turbulent structures that occur at the wall region of a flat plate will also exist close to interfaces. They are expected at the interphase at the gas side, as we have already cited, however, at the liquid side, the interface conditions are very different from the ones on solid surfaces, and studies investigated what happens at this region.

To clarify this fact, Rashidi and Banerjee [29] realized experiments in which the flow structures close to the interface were visualized. They verified, at the interface in the liquid phase, the appearance of streaks and bursts similar to the ones in the wall region.

Lombardi *et al* [16] showed that in the gas-liquid configuration, sweep regions (regions with movements bringing fluid from the gas bulk to the interface) are correlated to high shear interface zones and ejections (regions with movements bringing fluid to the gas bulk) are correlated to low shear interface zones. However, in the liquid side, there is no correlation of sweep-ejection regions to the interface shear. Their DNS studies were performed in a channel configuration where they varied the density ratio, which they represented by $R = \sqrt{\rho_{liq}/\rho_{gas}}$, and analyzed the difference of the near interface characteristics for $R=1, 10, 29$, these configurations being labeled as R1, R10 and R29, respectively, and the latter being the case of air/water configuration. They also provided the results of a reference case, CH, where a “no-slip” boundary condition is applied at the interface, i.e., the fluids are uncoupled and the flow corresponds to that in a channel with one slip wall and one no-slip wall. They stated that the R1 would not be a physical realizable situation, but this is in fact the case of two stratified liquids (e.g. oil/water) and the main interest of this work. The results of Lombardi *et al* [16] showed that the liquid side may actually present wall flow like characteristics in low density ratios, and deviate as the density ratio increases, as can be seen in Figure 2.5. This is particular interesting whet dealing with liquid/liquid interfaces, where the density ration remains at the order of $R=1$.

Studies like the ones of Banerjee *et al* [30] [31] [17] , Calmet and Magnaudet [25], Gualtieri and Doria [15], Komori *et al* [19], Peirson *et al* [21] , Takagaki *et al* [28], Liu *et al* [32], and many others have been investigating how deformable and non-deformable interfaces with and

without waves and the turbulent structures close to the interface region affect the mass transfer of a given species. They try to correlate the mass transfer with hydrodynamic parameters and arrange it with the basis of different mass transfer theories. These theories are described in the next section.

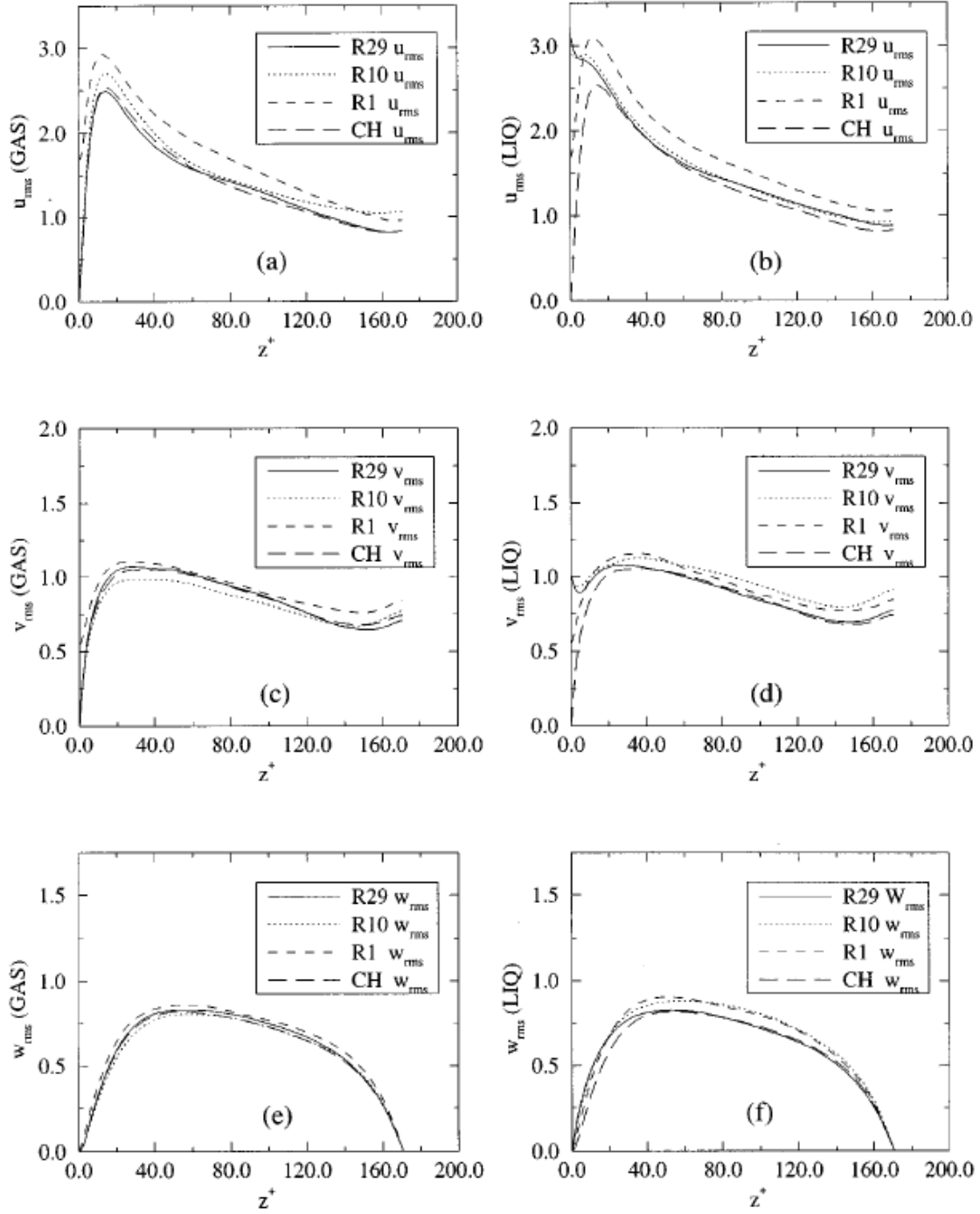


Figure 2.5 - Root-mean-square velocity fluctuations (u_{rms} , v_{rms} , w_{rms}), gas and liquid side, cases R29, R10, R1, and CH from Lombardi *et al* [16].

2.2 Mass Transfer in Multiphase Flows

2.2.1 Mass Transfer across Liquid-Gas Interface – A brief overview

Mass transfer occurs when there is a concentration gradient. The flux is directed from the region of high concentration to the one with lower concentration. This concentration difference of the transferred species is the driven force of the mass transfer.

There are a vast number of published investigations concerning the mass transfer across the liquid-gas interface. These investigations can be numerical ([31] [33] [30] [34] [35]) or experimental ([36] [37] [38] [39]) allowing the development of empirical models and the validation of numerical models for the mass transfer coefficient calculations at the different phases.

Turney and Banerjee [40] [30] discussed the formulations for the mass transfer coefficient at the liquid-gas interface. For their widely applications, we could mention some of these formulations as the film theory of Lewis and Whitman [41], the penetration theory of Higbie [42], the renewal surface theory of Danckwerts [43] and the surface divergence theory of Banerjee [34]. Each of these groups is based on a distinct hypothesis of the flow behavior close to the liquid-gas interface and they will be explained in section 2.2. All these approaches show that the mass transfer of a given chemical species depends on a transport property, the mass diffusivity, and on the hydrodynamic conditions maintaining the contact between these phases, such as the film thickness [41], the time that the fresh fluid packets coming from the bulk flow remain in contact with the interface [42], the surface renewal time [43] and the divergence of the interface parallel flow [34]. These quantities are hard to be experimentally measured, forcing us to make use of empirical relations and/or much complex mathematical models to describe all the physical phenomena involved.

Numerical investigations of the mass transfer phenomenon at the liquid-gas interface vary from those that consider a tank with a liquid phase in laminar regime [44] [45] (where the liquid surface is characterized by the low perturbation degree) to those that consider the liquid phase to be on a turbulent regime [25] [46] [26] (assuming that the transport mechanisms in the gas phase are not limiting factors for the mass transfer). In these investigations, the thickness of the mesh elements at the interface region is reduced in order to guarantee at least three mesh elements at the mass boundary layer [25]. Latter, the mass transfer calculated is correlated to the different theories and the coefficients are adjusted.

In this chapter, we will describe the main mass transfer theories used in the scientific communities to estimate the mass transfer coefficients.

2.2.2 The film theory

Because of its simplicity, the film theory developed by Lewis and Whitman [41] is one of the most used models for mass transfer studies. Its mathematical formulation is relatively simple and its predictions are usually close to those of the most sophisticated models, such as the renewal theory. The main hypotheses for this model are:

- The mass flux occurs in both sides of the interface;
- The flow is steady;
- The equilibrium conditions are instantly attained at the interface;

In this model, it is considered two thin fluid films or boundary layers, adjacent to each of the interface sides at which the mass transfer resistance is located. It is assumed that at each of these fluid films the boundary-tangential concentration gradient is negligible compared to the boundary-normal gradient, and that in the bulk of each phase interface the turbulence is sufficient to eliminate any concentration gradient. Figure 2.6 schematically shows this theory.

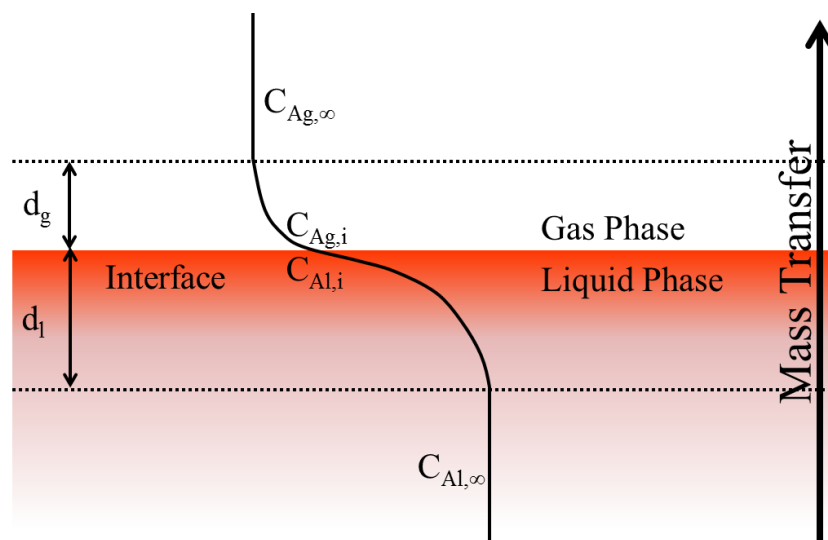


Figure 2.6 – Scheme of the film theory.

According to this theory, the mass flux on the liquid layer, where the molecular diffusion is dominant, can be calculated from Eq.(2.1).

$$J_A = -D \frac{\partial C_A}{\partial y} \quad 2.1$$

Where J_A , D , C_A , are the mass flux, the molecular diffusivity and the concentration of specie A respectively and y is the direction perpendicular to the interface. As the film represents a very thin layer (d_g) or (d_l) at the gas and liquid side, respectively, Eq.(2.1) can be rewritten as

$$J_{Al} = -D \frac{\partial C_A}{\partial y} = -D_l \frac{(C_{Al,i} - C_{Al,0})}{d_l} \quad 2.2$$

Or

$$J_{Al} = k_l (C_{Al,i} - C_{Al,0}) \text{ where } k_l = \frac{D_l}{d_l} \quad 2.3$$

And to complement the theory, the mass flux in the gas phase is given by

$$J_{Ag} = -k_g (C_{Ag,i} - C_{Ag,0}) \text{ where } k_g = \frac{D_g}{d_g} \quad 2.4$$

In these equations $C_{Al,0}$ and $C_{Ag,0}$ are the concentrations of species A in the bulk of the liquid and gas phase (both in kg/m^3) respectively, $C_{Al,i}$ and $C_{Ag,i}$ are the interface concentration of species A, and D_l and D_g are the diffusivity of the substance in the liquid and gas phase, respectively.

The film thickness, d_g for the gas phase and d_l for the liquid phase, which provide information about the hydrodynamics of the gas-liquid system, depends upon factors such as the geometry, physical properties and the agitation mechanisms. High turbulence intensity, for example, diminishes the values of d_g or d_l and consequently increases the mass transfer coefficient (Eq.(2.3) and (2.4)). Temperature variations may influence the mass transfer coefficient in two different ways; firstly, it may change the diffusivity D and secondly it could change the viscosity and then alter d_g or d_l .

k_g and k_l are the mass transfer coefficients at the gas phase and liquid phase respectively, usually expressed in m/s. The values of k_g and k_l depend upon the velocity in which the water or gas are moving, the temperature, species properties such as the diffusivity and the viscosity and the geometry of the system [45].

The equilibrium concentration at the interface, $C_{Ag,i}$ and $C_{Al,i}$, can be described by the Henry's constant in its dimensionless form

$$K_H = \frac{C_{Ag,i}}{C_{Al,i}} \quad 2.5$$

From Eq.(2.5) and considering $J_{Al} = J_{Ag} = J_A$, which is the total flux, we obtain Eq.(2.6):

$$C_{Al,i} = \frac{k_l C_{Al,0} + k_g C_{Ag,0}}{k_g K_H + k_l} \quad 2.6$$

Substituting Eq.(2.6) in Eq.(2.3) one obtains

$$J_{Al} = \frac{k_l k_g K_H}{k_l + k_g K_H} \left(C_{Al,0} - \frac{C_{Ag,0}}{K_H} \right) \quad 2.7$$

$$J_{Al} = K_L \left(C_{Al,0} - \frac{C_{Ag,0}}{K_H} \right) \quad 2.8$$

Where K_L is the global mass transfer coefficient at the liquid side and corresponds to a combination between the mass transfer coefficients of each phase, as

$$K_L = \frac{k_l k_g}{k_g + k_l / K_H} \text{ which results in } \frac{1}{K_L} = \frac{1}{k_l} + \frac{1}{k_g K_H} \quad 2.9$$

To solve Eq.(2.8) it is necessary to measure $C_{Al,0}$, $C_{Ag,0}$, K_H and K_L . We can assume $C_{Al,0} = C_{Al,\infty}$ for a homogeneous mixture. However, $C_{Ag,0}$ cannot be assumed to be equal to $C_{Ag,\infty}$ even for a homogeneous mixture and measurements close the interface in the gas phase must be done. An expression similar to Eq.(2.8) can be derived for the gas phase.

The main advantage of using Eq.(2.8) is that it is based on quantities that can be measured, rather than the concentrations at the interfaces, which cannot be measured in experiments. In gas-liquid mass transfer, the resistance to the transfer in the liquid side, $1/k_l$, is considerably higher than the resistance in the gas phase, $1/k_g$. In this case, the liquid film controls the transfer rate across the interface.

The disadvantage of the film model is that the flow is hardly ever stable to really present a laminar boundary at the gas-liquid interface. However, for its simplicity, this model is still used as a base for other models.

2.2.3 The penetration model

Higbie [42] proposed a model where the liquids at the interface are periodically renewed by new fresh fluids coming from the bulk. In his model, the mass flux is a function of the time these new fluids remain in contact with the interface. This model considers that these new fresh fluids are continually emerging from the bulk and that every new fluid packet remains in contact with the interface for the same given time, t , this time being a function of the turbulence or agitation level of the system.

A resolution of the mass balance provides the concentration profiles where it is possible to evaluate the mass flux at time t . For the liquid phase we have

$$J_{Al} = -D \frac{\Delta C_A}{\Delta y} = \sqrt{\frac{D_l}{\pi t}} (C_{Al,i} - C_{Al,0}) = k_l (C_{Al,i} - C_{Al,0}) \quad 2.10$$

Where k_l is the mass transfer coefficient at the liquid phase and is written by

$$k_l = \sqrt{\frac{D_l}{\pi t}} \quad 2.11$$

where k_l depends on the diffusion coefficient of the solute in the liquid phase and t is the residence time of the fluid packets at the interface region.

The basic difference between the film model and the penetration model is that the first one considers a well-established concentration gradient in each phase, from which results the mass transfer by diffusion in steady state. The second, however, considers the liquid as a set of fluid packets, where each packet is exposed at the interface, for a given time, in which there is a transient diffusion mass transfer.

2.2.4 The surface renewal time model

The penetration theory was reinterpreted by Danckwerts [43], who created the surface renewal time theory. He supposed that the time which fluid packets remain at the interface region is not constant but rather follows a normal distribution. In that manner, the fluid close to the interface can be renewed at any time with a certain probability, which was more typical of what might be expected from a turbulent fluid, giving on the liquid side,

$$J_{Al} = \sqrt{\frac{D_l}{\bar{t}}}(C_{Al,i} - C_{Al,0}) = k_l(C_{Al,i} - C_{Al,0}) \quad 2.12$$

where the mass transfer coefficient is

$$k_l = \sqrt{\frac{D_l}{\bar{t}}} \quad 2.13$$

Where \bar{t} should be thought of as the mean time between surface renewals.

Here one should have two important observations; firstly, the film model proposed a mass transfer coefficient directly proportional to the diffusivity, D , whereas the other models proposed a coefficient $k \propto D^{1/2}$, which have been proved to be more accurately in predicting experimental mass transfers. Secondly, none of the theories give precise information of how to measure the time between the fluid packages renewal and the techniques to measure the mean time between bursts.

A number of researchers proposed various models for \bar{t} in the 1960s, notably the large-eddy model of Fortescue and Pearson [47] and the small-eddy model of Banerjee *et al.* [34]. The large-eddy model (LEM) gave

$$\bar{t} \approx \frac{L}{u} \quad 2.14$$

Where L is the turbulence integral length scale and u is the integral velocity scale. This model was simplified by Banerjee [31], who considered a $\bar{t}^+ = 30$ to 90 (ν/u^{*2}) at Eq.(2.13). He obtained the following expression:

$$\frac{k_l Sc^{0.5}}{u^*} = 0.108 \text{ to } 0.158 \quad 2.15$$

This expression was compared with simulation results over a large range of Sc number by de Angelis [48] and good agreement was found for the high Sc number cases.

On the other hand, the small eddy model (SEM) of Banerjee *et al.* [34] gave

$$\bar{t} \approx \sqrt{\frac{\nu}{\varepsilon}} \quad 2.16$$

where ε was the turbulent energy dissipation rate close to the interface and ν was the kinematic viscosity. Here ε can be calculated as, for example, $\varepsilon \approx u^3/L$.

These models were validated with a few different set of experiments. However, when used to predict the mass transfer coefficient for the same study, they provided very different mass transfer coefficients. Theofanous *et al.* [49] resolved this discrepancy by showing that the large and small-eddy models gave good results of the transfer coefficient at small and large turbulent Reynolds numbers, respectively.

As Reynolds numbers based on integral scales in the field are variable, but often quite high, 10^3 to 10^5 , the small-eddy model and the surface divergence model, which will be explained in the next section, are appropriate, and many experiments are directed towards finding the near surface energy dissipation rate, ε , as discussed later [17].

It is also important to note that Banerjee *et al.*'s SEM is quite general, and energy dissipation may arise from many factors, e.g. wind shear, natural convection, wave breaking, rain, etc. In fact, Banerjee *et al.* originally applied the model to estimate mass transfer in situations where vorticity generation by capillary waves was important.

2.2.5 The surface Divergence Model

The difficulties in determining whether to apply the LEM or the SEM models as well as in measuring the renewal time led McCready *et al.* [50] to propose a different approach to the mass transfer modeling. His approach uses the governing equations (advection–diffusion equation) to suggest that the gas–liquid transfer rate is controlled by surface-normal motions. The key simplifications are that at high Sc the interface parallel motions have a negligible effect compared to the interface-normal motions, and that only near-surface (viscous boundary layer) motions need consideration. Therefore the velocity field used with the advection–diffusion equation is the first term in a Taylor series expansion, as explained by Turney and Banerjee [27], and

$$v_i = - \left(\frac{\partial u_i}{\partial x} + \frac{\partial w_i}{\partial z} \right) y = -\gamma y \quad 2.17$$

where u_i , v_i and w_i are the near-surface velocities in the x , y , and z directions (y being oriented normal to the local interface with $y=0$ at the interface). The terms in parenthesis are the ‘surface divergence’ strength and are labeled γ for convenience. Even though the model is

called the surface divergence model (SDM), it uses the fluctuation values of γ , namely γ' . Chan & Scriven [51] had shown that, given a time series of γ values, they could directly calculate the interfacial scalar transfer. McCready *et al* [50] further developed this model and showed that, a time series of γ with statistics similar to that of real turbulence, which means, $\gamma = \bar{\gamma} + \gamma'$, leads to

$$k = 0.71(D\gamma')^{1/2} \quad 2.18$$

where $\gamma' = (\overline{\gamma'^2})^{1/2}$ is the rms of the surface divergence. One should note the units of γ and γ' [s^{-1}] and that in this form γ' in Eq.(2.18) is analogous to the renewal time needed in the LEM and SEM in Eq.(2.13).

Banerjee *et al* [33], based on the blocking theory of Hunt and Graham [52] derived a general form of the relation for the mass transfer coefficient at unshered interfaces with high Sc gas transfer and with the far field turbulence homogeneous and isotropic. He provided the mass transfer equation

$$\frac{k}{u} \approx Sc^{-1/2} Re_t^{-1/2} \left[\left(\frac{\partial u'^+}{\partial x^+} + \frac{\partial w'^+}{\partial z^+} \right)^2 \right]_{int}^{1/4} \quad 2.19$$

By considering

$$\gamma' = \left[\left(\frac{\partial u'}{\partial x} + \frac{\partial w'}{\partial z} \right)^2 \right]_{int}^{1/2} \quad 2.20$$

where the subscript *int* denotes the interface, and all quantities on the RHS of Eq.(2.19) and Eq.(2.20) were normalized by u and L , the integral velocity and length scales in the far field, and $Re_t = uL/\nu$ is the turbulent Reynolds number based on these scales. They improved the formulation by taking into account the effects of the interface curvature, $\kappa = -\nabla \cdot \mathbf{n}$, where \mathbf{n} is the vector normal to the interface and Eq.(2.19) turns into

$$\frac{k}{u} = C Sc^{-1/2} Re_t^{-1/2} \left[\left(\frac{\partial u'^+}{\partial x^+} + \frac{\partial w'^+}{\partial z^+} \right)^2 - 2v'^+ \nabla \cdot \mathbf{n} \right]_{int}^{1/4} \quad 2.21$$

Where we should note the proportionality coefficient $C \approx O(1)$.

These expressions are strictly applied if the far field turbulence is isotropic and homogeneous. If there is shear at the interface, the turbulence is locally generated and has characteristics somewhat similar to those of wall turbulence. It is expected that the surface divergence scaling is still respected in these cases, but the appropriate scaling variables should, now, be related to the viscous boundary layer parameters and kinematic viscosity of the fluid exerting resistance to the mass transfer, the so-called inner variables. In that manner, $k^+ = k/u^*$, $u_i'^+ = u_i'/u^*$.

In an attempt to directly relate the mass transfer coefficient with the far-field homogenous isotropic turbulence characteristics, Banerjee *et al* [33] used the blocking theory of Hunt and Graham [52] to derive the spectrum for the surface divergence term $\gamma = [\partial u/\partial x + \partial w/\partial z]_{int}$ in the form

$$S(\Omega) = 0.3[12\Omega^{1/2} - 7.2\Omega^{1/3}] \quad 2.22$$

Where Ω is a normalized frequency ($L\omega/u$), and the spectrum is valid for $\Omega > 5$. By integrating this spectrum from the integral length scale L to the viscous cut-off $(\nu/\varepsilon)^{1/2}$ and by using the relationship between integral and Kolmogorov scales, where $L/\eta \approx 0.5Re_t^{-3/4}$ with $\eta = (\nu^3/\varepsilon)^{1/4}$, they obtained the mass transfer coefficient for high Sc as

$$\frac{k}{u} \approx \frac{C}{Sc^{1/2}Re_t^{1/2}} [0.3(2.83Re_t^{3/4} - 2.14Re_t^{2/3})]^{1/4} \quad 2.23$$

Where the proportionality coefficient $C \approx O(1)$ as in Eq.(2.19) and Eq.(2.21). This expression may apply only to clean, unsheared rigid interfaces, with no effects due to surfactants or natural convection.

All of the relations for the SD model derive from the same simple relation, which can be stated in its dimensional form as in Eq.(2.18). Where D is the mass diffusivity of the transferred species and γ' is the rms of the surface divergence, as previously described, and has dimensions of s^{-1} . The divergence strength provides information similar to the renewal time from the models of Dankwerts [43], who extended the works of Higbie [42]. Note that the LEM and SEM models also predicted the mass transfer proportional to $D^{1/2}$.

The main advantage of using mass transfer models based on the surface divergence instead of the time between renewals is that γ is more easily measured than τ - usually by scattering particles on the liquid surface and measuring their trajectories as did by Kumar *et al.* [53] as

stated by Banerjee *et al* [30]. However, this conclusion is only true when investigating stratified flows with low perturbations and the absence of interface fragmentation. The problems come out when we have to choose the reference surface to the divergence statistics when many droplets are present and advected within the bulk flow. For instance, the statistics to derive γ' are performed over the whole surface, but it may be completely different and complex to perform such statistics on a large amount of droplets surfaces.

2.3 Conclusion

We have seen in this chapter how turbulence interacts with free surfaces and many studies based on gas-liquid configurations. Different aspects of turbulence in the vicinity of the interface in both sides are discussed. Many researches showed that for the gas-liquid configuration, the gas side perceives the liquid as a movable wall, whilst the same does not happen for the liquid side. This behavior may change if the density ratio of the fluids is low ($R \approx 1$), where the turbulence characteristics at the liquid side may present structures similar to that of the wall region in wall-bounded flows.

The mass transfer models used to predict the mass transfer velocity have been presented. These models are based on theories that have been proved very efficient in gas-liquid mass transfer, but have never been tested in liquid-liquid cases. The mass transfer theories are mainly relied on the friction velocity and the divergence field of the parallel flow at the interfaces, thus, it is evident the importance of thoroughly describe the flow near the interface regions.

For industrial cases, where there is high interface fractioning and droplets formation, we believe that the simplifications of the renewal time models, based on the friction velocity, are more appropriate. This is due to the relatively easiness of computing the shear velocity. The same easiness is not found in the implementations of the surface divergence models. The needed statistical treatments of the surface divergence strength is a simple task when investigating stratified flows with low interface perturbations, but it is much more complex when applied on fragmented interfaces where droplets are advected with the bulk flow.

We have in mind that all of these mass transfer models were conceived to be applied on gas/liquid mass transfer with a relatively low range of Sc numbers and interface perturbations. Also, they are mainly tested and applied on isotropic and homogeneous turbulence, which

may not be the case of industrial applications. Nonetheless, we believe it is worthy to investigate its application on industrial process of liquid/liquid mass transfer and verify its accuracy to obtain local mass transfer coefficients.

We proceed this study with the presentation, in Chapter 3, of the experimental apparatus and physical methods used in this work. Chapter 4 will describe the mathematical models and numerical methods whilst the results are provided in chapter's 5 to 7.

3 Experimental Methods

Physical and numerical methods are important tools to study metallurgical processes. When trying to optimize such processes by looking for the optimal operational conditions, these methods are very useful to verify the influence of different process variables without harming the operational routines, and to reduce the costs of trials and losses for non-conformities in the metallurgical processes.

In this sense, it is desired that the mathematical model be able to fully describe one specific process, determining possible interactions among gas, liquid metal and liquid slag. However, this task is too complicated even to the most sophisticated calculators, and it is obvious that several approximations and simplifications are needed to obtain a satisfactory solution to the problem. On the other side, physical modeling is a valuable alternative that allows the simulation of such process in affordable conditions and the evaluation of many characteristics of the processes.

3.1 Continuous Casting (CC) Water Model

In this chapter, we will describe the experimental apparatus and the techniques used to extract the data needed to analyze the flow in such models. Such techniques include the Laser Doppler Anemometry (LDA) to measure the velocity field inside the water model, the image processing, which was performed with Python®, and the Experimental Interface Tracking (EIT) method, which we developed to locally track the liquid-liquid interface.

3.1.1 Similitude: Non-Dimensional Parameters

Generally speaking, the physical modeling consists in building a model in laboratorial scale of one specific reactor, and simulating the process that takes place in such reactor. For the obtained results in laboratory scale to be applicable in industrial scale, it is necessary to respect some similarities between the model and the real process. We say that the model and the industrial reactor are similar when they exhibit a constant ratio between correspondent values and scales, named similarity relations or scale relations [54].

The similarity between the industrial process and the model may include geometric, mechanic (which is divided in static, kinematic and dynamic), thermal and chemical similitude. For the fluid dynamic study, and considering a turbulent flow that can be modeled by the Navier-

Stokes equations, the dominant forces that govern the fluid are the inertia, gravity, shear and possibly the surface tension [54]. The dimensionless numbers obtained from these forces are:

- The Reynolds number (Re): the ratio between the inertial and viscous forces

$$Re = \frac{\rho Lu}{\mu} \quad 3.1$$

- The Froude (Fr): the ratio between inertial and gravitational forces

$$Fr = \frac{u^2}{gL} \quad 3.2$$

- The Weber (We): the ratio between inertial and surface tension forces

$$We = \frac{\rho u^2}{\sigma} \quad 3.3$$

Where ρ is the fluid density (kg/m^3); μ is the molecular viscosity ($\text{Pa}\cdot\text{s}$); u is a characteristic velocity scale (m/s); L is a characteristic length scale (m); g is the gravity acceleration (9.81 m/s^2); and σ is the surface tension (N/m^2).

According to de Santis *et al* [55], if we neglect the solid shell presence in the mold and the effects on the fluid flow of the convective motion due to the steel dependence on temperature (including fluid velocity, which is generally one order of magnitude weaker than the average liquid velocity in the mold), the main field forces are related to inertia and gravity. Thus, the relevant dimensionless numbers for this physical system are the Froude number and the Reynolds number. The high value of $We (O) \approx 10^4$ in this system also indicates that the effects of inertia are predominant over the surface tension effects and we can neglect it. Hence, for a physical model we should have $Re_p = Re_I$ and $Fr_p = Fr_I$, where p stands for physical model and I for Industrial process, and we have

$$\left(\frac{\rho UL}{\mu}\right)_p = \left(\frac{\rho UL}{\mu}\right)_I \quad 3.4$$

$$\left(\frac{U^2}{gL}\right)_p = \left(\frac{U^2}{gL}\right)_I \quad 3.5$$

Water is usually used to simulate liquid steel since the flows of water and liquid steel are quite analogous as they have very similar kinematic viscosity ($\nu_{\text{water}} = 1.0 \times 10^{-6} \text{ m}^2/\text{s}$ and $\nu_{\text{steel}} = 0.8 \times 10^{-6} \text{ m}^2/\text{s}$), implying that

$$\left(\frac{\mu}{\rho}\right)_p = \left(\frac{\mu}{\rho}\right)_I \quad 3.6$$

And substituting Eq.(3.6) in Eq.(3.4) we have

$$\left(\frac{\rho UL}{\mu}\right)_p = \left(\frac{\rho UL}{\mu}\right)_I \therefore (UL)_p = (UL)_I \Rightarrow \frac{U_p}{U_I} = \frac{L_I}{L_p} = \lambda \quad 3.7$$

Where λ is a scale factor.

For the Froude number, simplifying Eq.(3.5) we have:

$$\left(\frac{U^2}{L}\right)_p = \left(\frac{U^2}{L}\right)_I \Rightarrow \frac{U_p^2}{U_I^2} = \frac{L_p}{L_I} = \frac{1}{\lambda} \Rightarrow \frac{U_p}{U_I} = \lambda^{-1/2} \quad 3.8$$

If a physical model is meaning to respect the Reynolds and the Froude dimensionless numbers, we have, from Eq.(3.7) and (3.8), $\lambda = \lambda^{-1/2}$. Therefore, the only scale factor respecting both dimensionless numbers criteria would be a full scale water model, where $\lambda = 1$. A full scale model would reproduce the same velocity field found in the industrial process. It is important to note that this result is valid when the flux in the mold is laminar. In practical cases, flow is turbulent in most of the mold domain and the turbulent viscosity is not known *a priori* [54]. But in the present work we used a CC mold water model with linear scale of approximately 1:3, which means that

$$\frac{L_I}{L_p} = \lambda = 3 \quad 3.9$$

And we cannot respect both dimensionless number criteria. In this case, we evaluate the implications in respecting each of these criteria and we respect the most reasonable one. By respecting the Re similarity criteria, we have

$$\frac{L_I}{L_p} = \frac{U_p}{U_I} = 3 \Rightarrow U_p = 3U_I \quad 3.10$$

And the velocities in the system will be extremely high, producing many disturbances and complications during the physical and numerical simulations. On the other hand, by evaluating the *Fr* similarity criteria, we have

$$\frac{U_p^2}{U_I^2} = \frac{1}{3} \Rightarrow U_p = \frac{U_I}{\sqrt{3}} \quad 3.11$$

And we see that respecting the Fr similarity criteria will lead to a much more affordable situation. As a result, we chose to respect the Froude number and the configurations of the water model are presented in Table 3.1.

Table 3.1 – Industrial and experimental dimensions of the CC mold used.

	Industrial CC mold	Water Model CC mold
Mold width (m)	1.2 - 2.0	0.48
Mold Thickness (m)	0.2 - 0.3	0.10
Casting speed (m/min)	0.5 - 1.5	0.56
Liquid flow rate (m ³ /h)	0.4	1.6

3.1.2 Physical Model and Fluid Properties

The experiments were conducted in a CC water mold (Figure 3.1), which is similar to a rectangular glass cavity, schematically shown in Figure 3.2. The inner dimensions of the mold are $1.5 \times 0.48 \times 0.10 \text{ m}^3$ ($= H \times W \times T = \text{height} \times \text{width} \times \text{thickness}$).

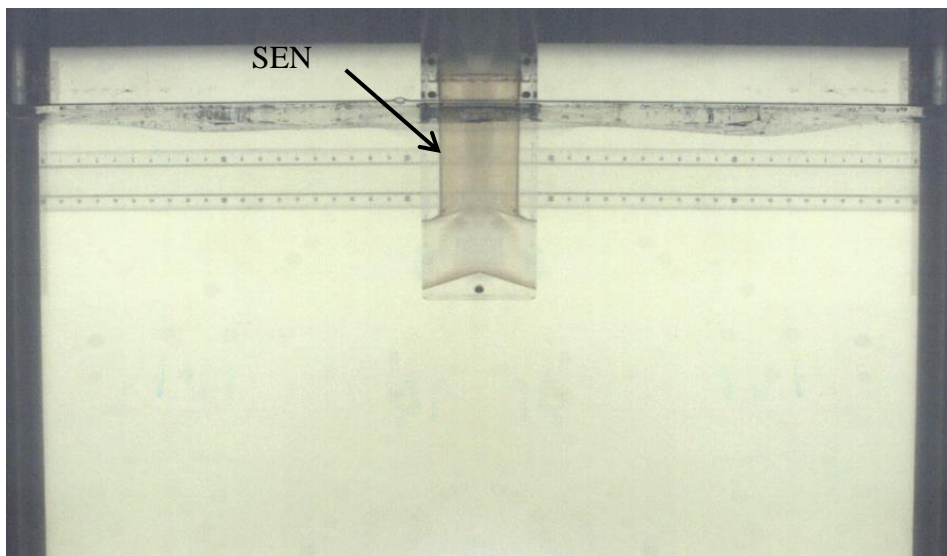


Figure 3.1 – Continuous Casting Water Model.

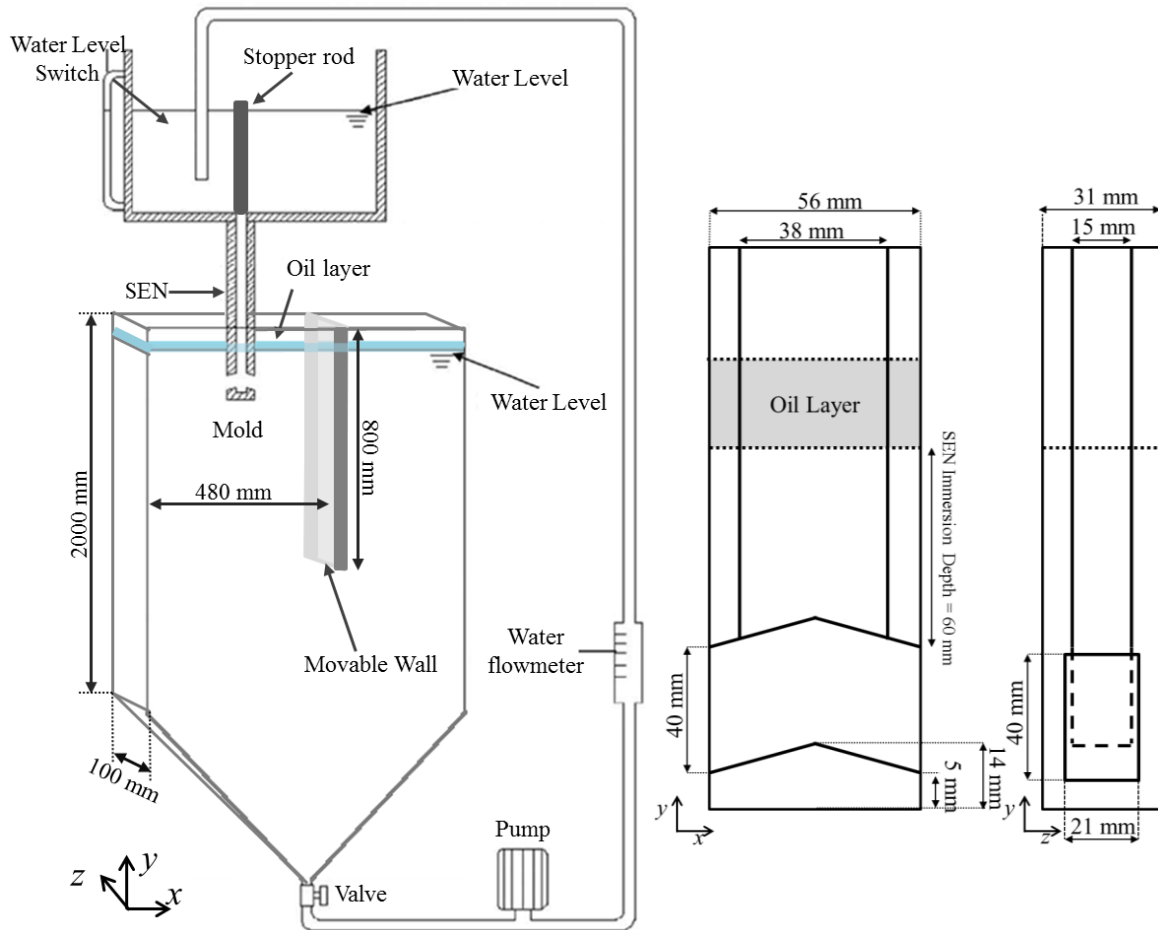


Figure 3.2 – CC water model and submerged entry nozzle (SEN) dimensions.

Water is fed into the mold through a rectangular cross sectional nozzle with inner dimensions of $15 \times 38 \text{ mm}^2$ and outer dimensions of $31 \times 56 \text{ mm}^2$. The average flow velocity in the nozzle is defined as the volumetric flow rate of liquid emerging into the cavity divided by the nozzle outflow area, giving $V_{in} = 0.78 \text{ m/s}$. It is known that due to a low dynamic pressure in the upper part of the nozzle opening the liquid flow may be unevenly distributed over the outflow area [56]. The nozzle is closed at the end but has two rectangular outflow openings of $21 \times 40 \text{ mm}^2$ in opposite sidewalls near the end of the nozzle, perpendicular to the nozzle cross section, as shown in Figure 3.2. The nozzle is submerged at a depth d_n measured from the top of the outflow opening to the water surface.

Through a hydraulic pump, water is pumped out of the mold into an external flow circuit and back into the nozzle, maintaining a constant volume of water in the mold. The inlet flow rate is varied between 1.6 and $2.04 \text{ m}^3/\text{h}$.

For further reference, an orthogonal coordinate system is defined with its origin located at the equilibrium position of the water surface in the center of the nozzle. The x-axis is parallel to

the equilibrium free liquid surface and to the front wall of the cavity, and the y-axis is in the upward vertical direction. Hence, the initial position of the water interface is at $y = 0$.

To simulate the liquid slag and its properties that vary during the process, two silicone oils were used. In order to have liable information to use in our CFD models, the surface and interface tensions of these oils were characterized with a Force Tensiometer – K100, which uses the Wilhelmy method to measure such properties. The oil characteristics are summarized in Table 3.2.

Table 3.2 – Fluid properties used in the experiments.

	Silicone Oil 1	Silicone Oil 2
Density (kg/m^3)	970	950
Viscosity (Pa.s)	0.034	0.019
Surface Tension ($\times 10^{-3}$ N/m) (oil/air)	21.1	20.3
Interface Tension ($\times 10^{-3}$ N/m) (oil/water)	31.7	32.6

3.2 Velocity Measurements

In this section, the experimental measurement techniques used in our multiphase system are described. Laser Doppler anemometry (LDA) was used to characterize the velocity field at the interface region. Image processing was also performed with the aid of a code built with Python language to provide insightful information about the interface displacement and wave induced motion. A methodology to locally track the interface was developed and is described at the last section of this chapter.

3.2.1 Laser Doppler Anemometry (LDA)

The LDA has been used in this work due to its non-intrusive principle, which allows the measurement of the velocity field without any intrusion in the fluid flow. It measures the instantaneous velocity of the fluid by detecting the frequency shift of laser light that has been scattered by small particles suspended in the flow. The LDA equipment used is a one dimensional component LDA. With this equipment, it was possible to measure the horizontal and the vertical component of the velocity field by turning the laser source in its support. The components of a LDA system are displayed in Figure 3.3:

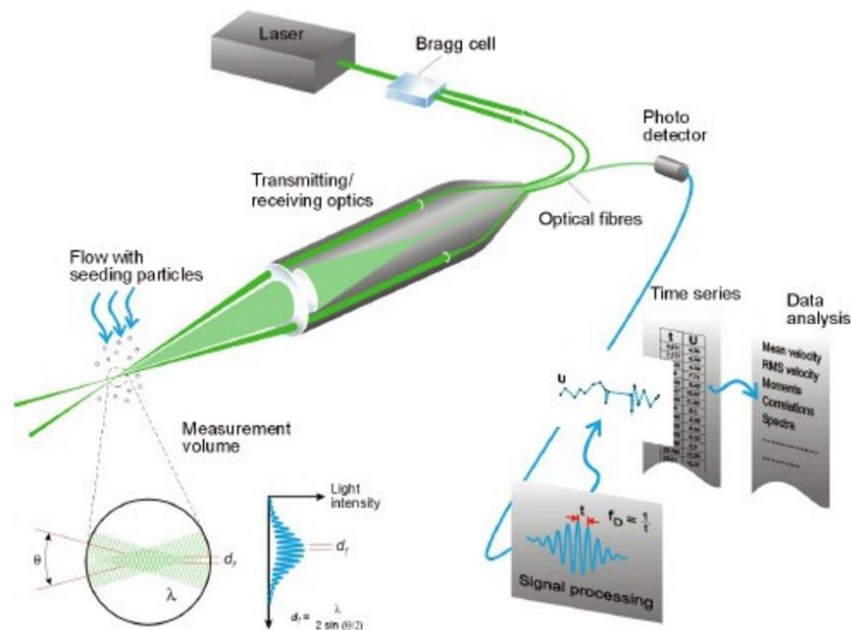


Figure 3.3 – The schematic diagram of LDA system [57].

In LDA, the light is emitted from a laser source with a specific wavelength toward the measurement point. In fact, the LDA technique does not measure the velocity of the fluid itself, but the velocity of particles dispersed in the fluid, called the seeding particles. Thus, for the measured velocity to be assumed the same as the fluid velocity, these particles must have the same specific mass as fluid of interest, in such a way that the gravity forces and the buoyancy can be neglected. The seeding particles may also have a geometric form that reduces the resistance forces that may interfere in the flow characteristics. They should scatter the light sufficiently and be generated conveniently. For a more comprehensive explanation of LDA principles the reader is referred to the Dantec website [57].

With the LDA technique, we could measure the mean flow velocity and the root mean square (rms) of the velocity field in each measured position, p . For each point of measure, 600 seconds of measures with an average data acquisition frequency of 80Hz were taken. We believed that this measurement time would be sufficient to characterize most of the low frequencies encountered in CC model configurations. The mean velocity and the rms at each point are calculated by

$$\bar{u}_p = \frac{1}{N} \sum_{i=1}^N u_{p,i} \quad 3.12$$

And

$$u_{rms} = \sqrt{\frac{1}{N} \sum_{i=1}^N (u_i - \bar{u})^2} \quad 3.13$$

With these measures, we could provide enough data to validate the CFD model and proceed with further analysis.

3.3 Image processing

3.3.1 Python Image Processing

In principle, an image is coded in a matrix whose the dimensions represent the image width and height. Each element in this matrix represents a pixel modeled by a matrix of three elements that represent the numerical values for the three primitive color intensities (red, green, blue), each color with 256 (8bits) tons. In the Python code, images are generated from geometric instructions describing objects, such as point coordinates, lines, circles and others. A code can be implemented to manipulate those data and adapt images for the desired measurements.

In our work, image processing can be a useful tool to analyze the interface movements and evaluate its influence in the interface near field. Taking images of the capillary line at the front mold wall provides very good estimation of the interface position if the flow is predominantly two-dimensional. However, according to Kalter *et al.* [56] [58], this is achieved only when the ratio of width to thickness (W/T) is sufficiently high (W/T > 13). In a usual CC configuration, W/T \approx 7 and the flows are three dimensional, having very unstructured and complex patterns. In the present model, W/T \approx 4.8. With this arrangement, it is very difficult to determine the exact interface position by filming the front wall of the cavity. To overcome this difficulty, a laser beam was pointed out perpendicularly to the interface, at the same positions where the LDA measures were taken. Once the laser touches the interface, the reflection can be used to locally track the movements in that vertical axis. We used a Motion Blitz EoSens Cube 6 high-speed camera to capture 16,370 images of the marked surface at 25 frames per second and with a resolution of 1280×1024 pixels. The spatial resolution achieved was 32.5 pix/mm. Figure 3.4 shows how the frames look like. With the images generated, we could locally track the interface movement.

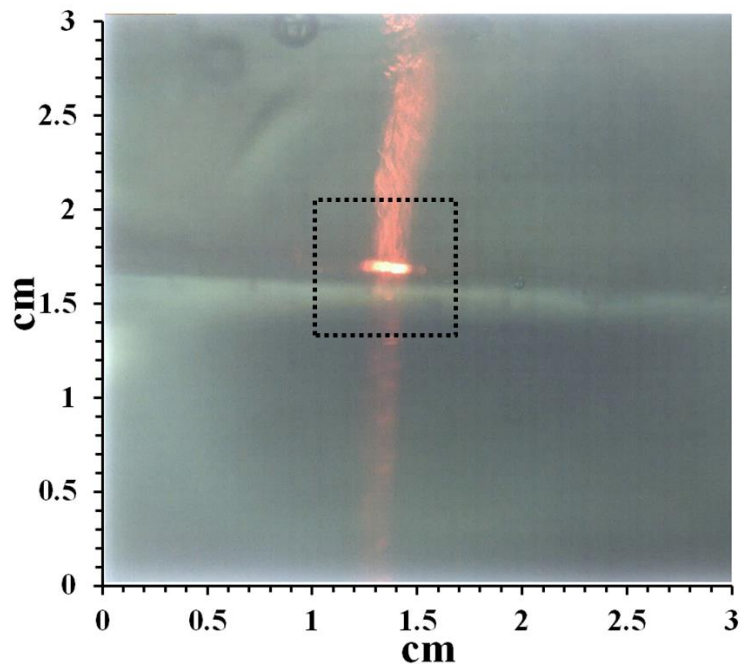


Figure 3.4 - Laser beam reflection at the interface position.

After recording, the images are processed by an algorithm implemented in the Python programming language, where the interface movement is measured and exported in a file for further data treatment. This technique is best described in the following section.

3.3.2 Experimental Interface Tracking (EIT)

The algorithm built to measure the interface displacement is based on Python OpenCV library and consists of four main steps. A first function was built to transform the images in gray color traces varying from black to white. The darkness of the traces corresponds to the intensity of the color gradient between the pixels. A second function filters the traces, keeping the traces with the maximum intensity, which roughly correspond to the interface contours. A trace is, usually, a continuous sequence of points, but in this case, when isolating and filtering these traces, they can represent image defects and discontinuities. To solve these problems, a third function is needed to reconstruct these traces by keeping their darkest neighbors. When all the first neighbors are white, the code searches in the values of the second neighbors. If a black pixel is found, it is linked by darkening the intermediate pixel. Finally, to keep only the main traces, which correspond to the laser reflection and/or the interface, a last function is used to erase the traces shorter than a critical length.

Once the contours are isolated, the algorithm searches for the laser reflection in a vertical line previously determined. With the position of the laser mark, the algorithm is able to track the

interface movements and store the data in an external file. The line distance from a reference point to the laser reflection is drawn on the pictures for verification.

All those steps are shown in Figure 3.5 (a-d).

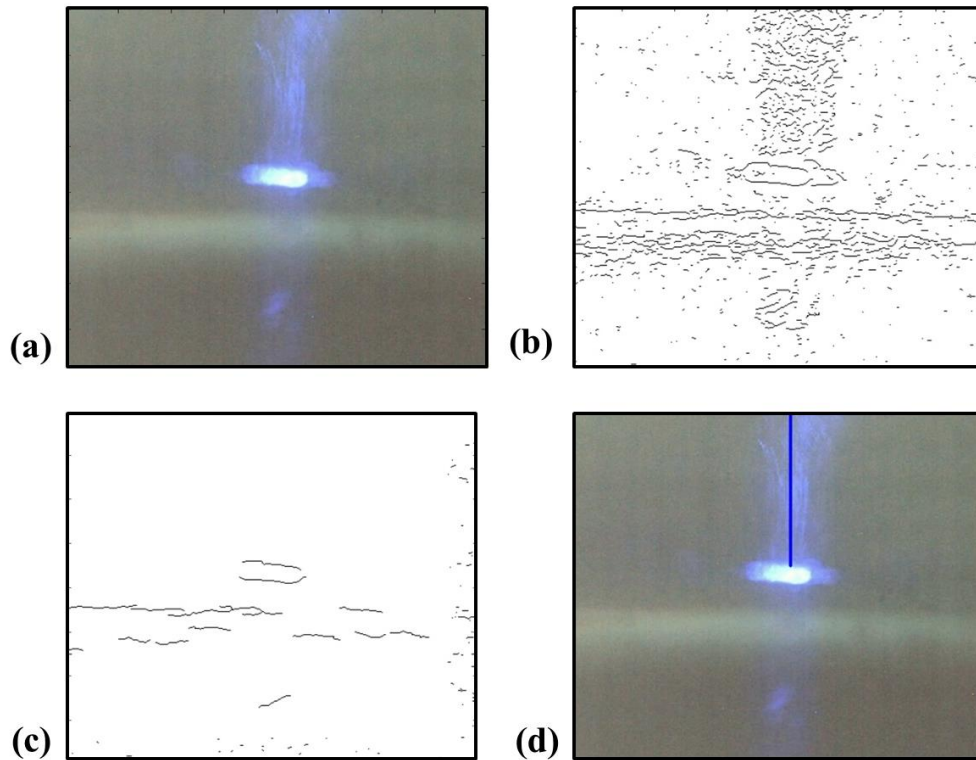


Figure 3.5 - The main steps of the procedure: In (a) the extraction of the frames from the video, in (b) the isolation of the contours, in (c) the filtering of the noisy contours and in (d) the measure of the interface position.

It is important to note that the interface position is measured in pixels. Consequently, we have to convert these measures in metric units. The pixel to centimeter can be easily achieved by placing a rule at the positions where the interface is tracked and tracing a line at this frame (Figure 3.6).

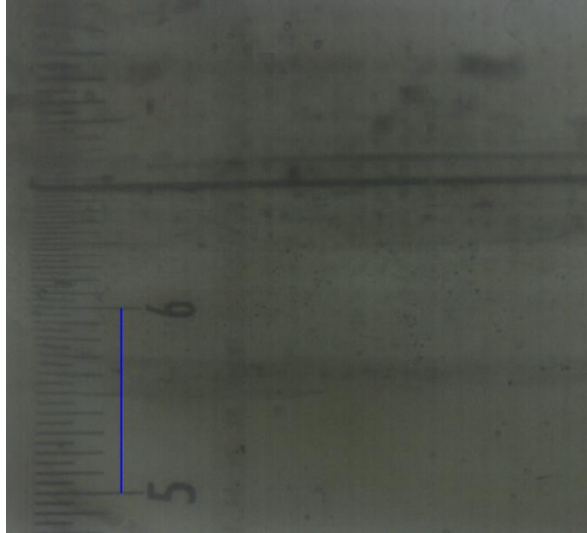


Figure 3.6 – Rule placed to determine the pixel to cm conversion factor.

With the length of the traced line we obtain the conversion factor by applying a proportionality rule as follows

$$d_{mm} = d_{pix} \frac{l_{mm}}{l_{pix}} \quad 3.14$$

Where d_{mm} is the distance in mm, d_{pix} is the distance in pixels, l_{mm} is the length of the traced line in mm and l_{pix} is the length of the traced lines in pixels.

3.4 Conclusions

In this chapter, we presented the physical experiments and methods used in this work. The results from the experiments will be used to validate the CFD model which can provide more details of the flows in the CC configuration. We have seen that the mathematical model can be validated based on the mean flow velocity, the rms velocity (which will give an estimation of the turbulence intensities in the domain), and the interface displacement.

We believe that these are key features to be checked before proceeding with further investigations based on the CFD results. The numerical methods are detailed in the next chapter.

4 Models and Numerical Methods

In this section, we will present the models and numerical methods used to build the CFD models to simulate our experiments. The code Thetis was used in this study and all the features needed to perform our simulations were already implemented and extensively validated, as we are going to see later. Hence, no new implementation on the CFD code was needed to accomplish the fluid flow description.

4.1 *The single fluid model*

4.1.1 Mass Conservation

The **law of mass conservation**, also known as **principle of mass/matter conservation**, states that the mass of the fluid of a closed system remains constant over time. Therefore, to model the evolution of this property, the first step is the mass balance among the fluid volume. The mass conservation equation or **continuity equation** is written as follows:

$$\frac{\partial \rho}{\partial t} + \nabla \cdot (\rho \vec{u}) = S_m \quad 4.1$$

Where ρ is the density, t is the time, u is the velocity vector and S_m is a source term representing the mass creation/consumption in the continuous phase, which in our case is considered null. Eq. (1.1) can be applied to compressible and incompressible fluids.

It is important to mention that the continuity equation, no matter in which form it is presented, is only a representation of the principle of mass conservation.

4.1.2 Momentum Conservation

The equation of momentum conservation, also called **momentum equation** came from the Newton's second law, which states that the ratio of momentum change in a fluid particle is equal to the sum of the forces acting on this particle. The Newton's second law says that the resulting force acting on a fluid particle is equal to its mass multiplied by its acceleration, as shown in Eq. (4.2):

$$\sum F_x = Ma_x = \frac{d(Mu_x)}{dt} \quad 4.2$$

In the unidirectional equation (4.2), $\sum F_x$ represents the sum of the forces acting on a body, M is its mass, and a_x is its resulting acceleration. The term on the right hand side of the equation is equal to the rate of change in momentum. The forces acting on a fluid are considered as any force capable of setting the fluid in motion, this will include forces derived from pressure, gravity, electromagnetic, added mass for accelerating flow as well as other forces such as buoyancy, surface tension and shear stresses.

4.1.3 Navier-Stokes Equation for Single Fluid Model

The multiphase flow of immiscible Newtonian fluids can be described with mathematical statements of conservation of mass and momentum. The continuity equation (1.1) is a statement of mass conservation, while the momentum equation is an embodiment of Newton's Second Law of Motion. From a mass and momentum balance, one can obtain the Navier-Stokes equations:

$$\frac{\partial \rho}{\partial t} + \nabla \cdot (\rho \vec{u}) = 0 \quad 4.3$$

$$\frac{\partial \rho \vec{u}}{\partial t} + \nabla \cdot (\rho \vec{u} \times \vec{u}) = -\nabla \vec{p} + \rho \vec{g} + \nabla \cdot \bar{\bar{T}} + S_m \quad 4.4$$

Where ρ is the density, \vec{u} is the velocity vector, p is the pressure, \vec{g} is the gravity, $\bar{\bar{T}}$ is the viscous stress tensor, $\bar{\bar{T}} = \mu_{eff}(\nabla \vec{u} + \nabla^t \vec{u})$ and S_m is a source term. In the viscous constraint tensor, the effective viscosity, μ_{eff} , is the sum of the molecular viscosity, μ , and the turbulent viscosity, μ_t , which will be discussed latter in the turbulence modeling section.

In our case of interest, the fluid is considered incompressible, meaning that there will be no density change in a given phase. Then, the continuity equation is reduced to

$$\nabla \cdot \vec{u} = 0 \quad 4.5$$

To accurately simulate multiphase flows, the interface between the fluids needs to be well computed. The interface is defined as a separation surface between two or more fluids, thus, the interfaces are locations with a very abrupt change in the fluid properties, such as density and viscosity.

The single fluid model allows us to track the interfaces by adding a phase function C which describes the interface shape/position evolution during the time by an advection function, described by Eq.(2.1).

$$\frac{\partial C_k}{\partial t} + \vec{u} \cdot \nabla C_k = 0 \quad 4.6$$

Where \vec{u} is the fluid velocity if there is neither phase change nor slip at the interface between phases. For each fluid k , the phase function has a value between 0 and 1:

$$C_k(x, t) = \begin{cases} 1 & \text{if } x \in \text{phase } k \\ 0 & \text{elsewhere} \end{cases} \quad 4.7$$

From this definition, the interface lies on the iso-surface where $C_k = 0.5$ and the phase properties across the interface, such as the density and the viscosity can be estimated with interpolation or phase functions; $f(C)$ and $g(C)$, for example. For that purpose, three schemes are commonly used for evaluating $f(C)$ [59]:

- Discontinuous averaging:

$$f(C) = f_1 \text{ where } C > 0.5, f(C) = f_2 \text{ elsewhere} \quad 4.8$$

- Arithmetic averaging:

$$f(C) = f_1 C + f_2 (1 - C) \quad 4.9$$

- Harmonic averaging:

$$f(C) = \frac{f_1 f_2}{f_2 C + f_1 (1 - C)} \quad 4.10$$

The choice of the best scheme depends on the nature of the flow been studied. Ritz and Caltagirone [60] used the arithmetic averaging for density and harmonic averaging for viscosity interpolation in the case of sedimentation of circular particles between two parallel walls. Pianet and Vincent [59] studied a set of four combinations to evaluate the best physical properties interpolation in the case of a rising compressible bubble in water column. These are, respectively, M1: discontinuous for both density and viscosity, M2: arithmetic averaging for both density and viscosity, M3: arithmetic averaging for density and harmonic averaging for viscosity, and finally M4: arithmetic averaging for density, arithmetic averaging when using diagonal components of the viscous stress tensor, and harmonic averaging when using extradiagonal components of the viscous stress tensor. They evaluated the accuracy of the methods by comparing terminal bubble velocities with corresponding error levels in comparison to experimental velocities. In this case, the best configuration found was the M2

(arithmetic average for both density and viscosity), which exhibits excellent interface cohesion as well as very little numerical fragmentation.

Then, the interpolation functions used to estimate physical properties at interfaces must be evaluated according to the case to be studied. In our case, not only the interface description but also the numerical diffusion of these physical properties must be evaluated. At a first attempt, we will adopt the same approach as adopted by Pianet and Vincent [59], thus, the physical properties will be estimated via an arithmetic average at the interface position. This configuration will be evaluated and changed if any considerable interface spreading is verified.

To complete the single phase model, the source term taken into account in the momentum equation is the surface tension, which is modeled using the Continuum Surface Force (CSF) method, based on the works of Brackbill *et al* [61]:

$$F_{ST}(C) = \sigma \kappa n \delta_i = \sigma \left(\nabla \cdot \frac{\nabla C}{\|\nabla C\|} \right) \nabla C \quad 4.11$$

Where the notation κ denotes the curvature, σ is the surface tension coefficient, \mathbf{n} the normal to the interface and δ_i the Dirac function indicating interface.

After that, the multiphase flow can be represented by an equivalent fluid and the single-fluid model Navier-Stokes equations are expressed as follows:

$$\nabla \cdot \vec{u} = 0 \quad 4.12$$

$$\frac{\partial \rho \vec{u}}{\partial t} + \nabla \cdot (\rho \vec{u} \times \vec{u}) = -\nabla p + \rho \mathbf{g} + \nabla \cdot (\mu_{\text{eff}} [\nabla \vec{u} + \nabla^T \vec{u}]) + \sigma \kappa n \delta_i \quad 4.13$$

$$\frac{\partial C_k}{\partial t} + \vec{u} \cdot \nabla C_k = 0 \quad 4.14$$

These models cannot be analytically solved in a complex 3D unsteady case. A numerical tool is needed to provide precise results in a time and space discretized domain. To solve multiphase simulations, there are two different methodologies generally used; the Lagrangian and Eulerian representation of the interface.

The first consists in discretizing one of the present fluids, and considering the interface between the fluids as a boundary condition of the problem. The Navier-Stokes equations in this domain allow the determination of the movement to this phase by taking into account the

fluids with the jump conditions at the interface. This method needs an adaptive mesh to track the interface. The interest in using this method is to be precise about the interface movement in time. The inconvenient is that it requires adapting the mesh in three dimension (remeshing procedure) that can be difficult or even impossible to deal with as soon as interfacial shape is complex, with for example coalescence or rupture. Also, this method is not adaptable to the droplet formation at the interfaces, which is crucial for industrial applications.

The second method, the Eulerian method, consists in discretizing the equations in the whole fluid domain. The boundary conditions are external and are not linked to the fluid interfaces. This method is very well adapted to the fixed Cartesian mesh, which is much more affordable than the adaptive one. It allows the description of the droplets formation and complex interface phenomena by solving the advection equation for the color function C .

The code Thetis developed at the laboratory I2M, allows the resolution of the single-fluid model equations presented in this chapter. The approximation of these conservation equations is carried out with an implicit finite volume technique of second order in time and space on a fixed Cartesian staggered grid. An implicit Augmented Lagrangian procedure is implemented to ensure the incompressibility constraint [62] [63] [64]. Centered schemes are used to discretize the space derivatives in the inertia and the viscous terms of the momentum equations. An iterative Bi-Conjugate Gradient Stabilized II solver [65], preconditioned under a modified and incomplete LU approach [66], is used to solve the linear system. The interfaces are simulated with the Volume of Fluid (VOF) Piecewise Linear Interface Construction (PLIC) interface tracking method of Youngs *et al.* [67]. The turbulence was computed via the Large Eddy Simulation (LES) approach with a mixed sub-grid scale (SGS) model. All these methods were extensively validated in previous works from S. Vincent *et al* [62] [68] [69] [70] [71] and are described in the next sections.

4.2 Turbulence modeling

4.2.1 General featuring's

Turbulence consists of fluctuations on the velocity fields in time and space. They are very complex processes, mainly because they are three-dimensional in most flow motions, unsteady and have a wide range of eddies. The turbulence is more significant when the fluid inertial forces become comparable with viscous forces, characterized by high Reynolds Number [72].

The Navier-Stokes equations are, *a priori*, capable of describing the laminar and turbulent flow without the need of additional information. The DNS, which uses directly the Navier-Stokes equations to solve fluid flows may be used in the future, but needs a lot of computational resources.

However, the turbulent flows in realistic Reynolds numbers cover a huge range of turbulent length and time scales, and usually involve length scales far smaller than the smallest mesh volume element used in a numerical analysis [73]. The smaller eddies are nearly isotropic and have a universal behavior (for turbulent flows at sufficiently high Reynolds numbers at least). On the other hand, the larger eddies, which interact with and extract energy from the mean flow, are more anisotropic and their behavior is dictated by the geometry of the problem domain, the boundary conditions and body forces [72].

Thus, the turbulent models are used to describe the effects of turbulence without the need of a fine mesh or huge computational resources. In general, the turbulence models modify the original unsteady Navier-Stokes equations by adding the average of the fluctuation quantities, so the majority of the turbulence models are statistic models (Reynolds averaged Navier-Stokes - RANS), except the LES (Large Eddy Simulation) and DES (Detached Eddy Simulation) models.

The models based on the turbulent viscosity consider that the turbulence consists of small vortices which are generated and dissipated, and where the Reynolds tensors are assumed to be proportional to the velocity gradients. The two equation models are largely used to numerically model many industrial applications; they offer a good compromise between numerical effort and computational accuracy. In these models the turbulence velocity scale comes from the turbulent kinetic energy, from the solution of a transport equation.

The RANS models provide statistic information about the turbulence, whereas the LES models are deterministic. As the interface description comes from the deterministic scheme of the single fluid model, we see the LES turbulence model as the more appropriate to this study. Also, it offers the possibility of increasing the accuracy of the calculations by directly solving the large eddy structures of the turbulent field, that are the most sensitive to the geometry of the flow, without the need of having a very fine mesh.

4.2.2 LES modeling for single fluid flows

The LES approach for the computation of turbulent flow accepts that the larger eddies need to be computed for each problem with a time-dependent simulation. The universal behavior of the smaller eddies, on the other hand, should hopefully be easier to be captured with a compact model. This is the essence of the **large eddy simulation** approach to the numerical treatment of turbulence [74].

In this turbulence model, the dynamic behavior of the large eddy structures are directly calculated, while the turbulence effect on the smaller eddies are modeled by the so called sub-grid scale (SGS) models. This methodology takes advantage of the fact that most of the transport momentum, energy and other scalars are realized by the larger eddies. The smallest eddies are just little affected by boundary conditions of the domain. These small scales are more isotropic than the big ones, statistically speaking and provide just a little contribution to the turbulent transport.

Hence, it is reasonable to expect that the LES turbulence model gives similar results compared to DNS, since the large eddies are numerically solved. But the LES is a simplification of the DNS given that the small scales are modeled. The LES is, then, an intermediate model between the DNS and the RANS models.

4.2.3 Spatial filtering of Navier-Stokes single-fluid model

To correctly apply the LES model, the domain must be filtered and the definition of what is a large eddy and a small eddy must be made. That can be achieved by applying filtering functions to the Navier-Stokes equations.

Filters are commonly used in electronics and process applications that are designed to split an input into a desirable, retained part and an undesirable, rejected part. To separate the large from the small scales in LES it is used a filtering function, $G(x, x', \Delta)$ which may be spatial, temporal or both. A filtered variable, denoted by an over bar, is defined as

$$\bar{\varphi}(x, t) = \int_{\Omega} G(x, x', \Delta) \varphi(x', t) dx' \quad 4.15$$

Where Ω is the entire domain, $\bar{\varphi}(x, t)$ is the filtered field, $\varphi(x', t)$ is the original (unfiltered) field and Δ is the filter cutoff width, which determines the size of the largest eddy removed by the filtering function and is usually defined as

$$\Delta = (\Delta x \Delta y \Delta z)^{1/3} \quad 4.16$$

where, Δx , Δy and Δz are the mesh size on x , y and z directions, respectively. This filter cutoff is chosen to ensure a cutoff length smaller than a grid size. Since only a single nodal value of each variable is retained on a grid cell, all the finer details are lost anyway.

The most commonly used filter functions in three-dimensional LES models are

- Gaussian filter:

$$G(x) = \sqrt{\frac{\gamma}{\pi \Delta^2}} \exp\left(-\frac{\gamma x^2}{\Delta^2}\right) \quad 4.17$$

Typical value for parameter $\gamma = 6$ [59]

- Top-hat or box filter:

$$G(x) = \begin{cases} 1/\Delta & \text{if } |x| \leq \Delta/2 \\ 0 & \text{otherwise} \end{cases} \quad 4.18$$

The top-hat filter is implemented in the code used in the present work and is the filter we used in our LES turbulence approach. Since the filtering function uses a cutoff length, scales smaller than that are eliminated from the filtered field, originating the sub-filtered field, denoted with a prime. Thus, the original unfiltered field can be expressed as a sum of the filtered and sub-filtered field:

$$\varphi = \bar{\varphi} + \varphi' \quad 4.19$$

The filtered equation, with scales larger than the cutoff length, forms the filtered single-fluid Navier-Stokes equation, which will be solved in LES.

4.2.4 Filtered Navier-Stokes equations for two-phase flows

Let us recapitulate the phase function C_k presented in Eq. (2.1) indicating the phase k ($C_k = 1$ in phase k and 0 elsewhere), G the low-pass filtering operator defining the spatial filtering of φ by $\bar{\varphi} = G \circ \varphi$, $\tilde{\varphi} = \overline{\sum_k \rho_k C_k \varphi_k} / \overline{\sum_k \rho_k C_k}$ the phase-weighted filtering of φ and $\bar{\bar{\varphi}} = \overline{\overline{\sum_k C_k \varphi_k}}$ the filtered average of φ . As a definition, $C_1 = C$ and $C_0 = 1 - C$.

The commutation between the spatial filter and the derivative is widely assumed in single-phase LES modeling [75] [76]. The same assumption is considered to apply for two-phase flows concerning $\bar{\varphi}$. Such assumption was verified by Vincent *et al* [77] and Larocque *et al* [78], even if the commutation error depends more on the topology of the mesh than on the characteristic of the flow [79] [80]. Under this assumption, the spatial filtering and averaging over phases of the incompressible Navier-Stokes equations (4.12 - 4.14) leads to the following set of equations

$$\nabla \cdot \tilde{u} = \frac{\rho_1 - \rho_0}{\bar{\rho}} \tau_0 \quad 4.20$$

$$\bar{\rho} \frac{\partial \tilde{u}}{\partial t} + \nabla \cdot (\bar{\rho} \tilde{u} \times \tilde{u}) + \nabla \cdot (-\bar{\mu}[\nabla \tilde{u} + \nabla^T \tilde{u}]) + \nabla \bar{p} - \bar{\rho} g - \bar{\sigma} \bar{\kappa} \bar{n}_i \delta_i = \sum_{i=1}^3 \tau_i \quad 4.21$$

$$\frac{\partial \bar{C}}{\partial t} + \tilde{u} \cdot \nabla \bar{C} = \tau_0 \quad 4.22$$

Four specific subgrid terms τ_0, τ_1, τ_2 and τ_3 appear due to the filtering and averaging operations of the momentum equations [81]. These subgrid terms are expressed with the following definitions [77]

$$\tau_0 = \overline{u \nabla C} - \tilde{u} \cdot \nabla \bar{C} \quad 4.23$$

$$\tau_1 = -\nabla \cdot (\overline{\rho u \times u} - \bar{\rho} \tilde{u} \times \tilde{u}) \quad 4.24$$

$$\tau_2 = -\nabla \cdot (\overline{\mu[\nabla \tilde{u} + \nabla^T \tilde{u}]} - \bar{\mu}[\nabla \tilde{u} + \nabla^T \tilde{u}]) \quad 4.25$$

$$\tau_3 = -\bar{\sigma} \left(\overline{\nabla C \nabla \cdot \left[\frac{\nabla C}{\|\nabla C\|} \right]} + \nabla \bar{C} \nabla \cdot \left[\frac{\nabla \bar{C}}{\|\nabla \bar{C}\|} \right] \right) \quad 4.26$$

The terms 4.23 to 4.26 must be modeled to close the LES equations for two-phase flows, as they depend on unsolved variables. They result from the Favre and filtered phase averages of velocity, density, viscosity and phase function. The subgrid stress tensor (4.24) and viscous term (4.25) are present in standard single-phase compressible LES equations, while the subgrid interfacial transport (4.23) and the subgrid surface tension force (4.26) are specific to two-phase flows. The magnitude of the different subgrid terms was *a priori* evaluated in the case of phase separation flows, turbulence bubble interactions [81] [69] or spray atomization [82]. Following these studies, the subgrid stress tensor τ_1 must be taken into account, while

the influence of τ_0 , τ_2 and τ_3 is highly dependent on the flow configurations and/or on the chosen two-phase description.

The contributions of these subgrid terms were studied by Vincent *et al* [77] and Larocque *et al* [78] with a fully resolved case, without using any subgrid scale model. Their results proved that the effects of the subgrid terms related to the interfacial transport, τ_0 , and surface tension, τ_3 , are important only in the cases with high droplet formation and interface fragmentation. Whilst the subgrid viscous term, τ_2 , is negligible compared to the subgrid stress tensor, τ_1 .

In the present study, we avoided the interface perturbations so we could measure the velocity field very close to the liquid/liquid interface. In this manner, it is expected that the subgrid terms related to the interfacial transport, τ_0 , and surface tension, τ_3 , may be negligible due to the low perturbations found at the interface. Accordingly, as the viscous term, τ_2 , was found to have negligible contribution as compared to ones of the subgrid stress tensor, τ_1 , we decided to keep only this subgrid term in our model. Hence, the LES turbulence model used in this study is reduced to single-fluid LES turbulence model.

The subgrid stress tensor, τ_1 , is modeled with a mixed subgrid scale (SGS) model implemented in Thetis and is based on the works of Zang *et al* [83]. The Mixed model can compute the energy dissipation from the large eddies to small ones (Smagorinsky SGS model [84]) as well as the energy transfer from subgrid scales to large eddies (Bardina SGS model [85]). More information is found in the works of Calmet [86] and Merle [87].

4.3 Fictitious Domain Method (FDM) for Obstacles and solid boundaries

The simulation of multiphase flows in complex geometries and/or obstacles in a structured mesh involves the definition of interfaces which not usually match with the mesh. Moreover, the same equations must be applied on both, liquids and solids, present in the domain during the calculations. Since the sub-domains defined by the different phases, liquids and solids, are distinguished by interfaces, those interfaces may not match with the cells walls at the boundaries of the domain, and they are, from a mesh and discretization point of view, fictitious. The single-fluid model can be adapted to deal with this double constraint of accurately describe all the liquid-liquid and solid-liquid interfaces by means of the Fictitious Domain Method (FDM).

The FDM consists of considering the real domain, defined by different sub-domains, as one single domain with physical properties varying in time and space. With this consideration, the real domain studied, named Ω , is studied as a continuous domain with its sub-domains represented by fictitious domains according to the different local properties.

These sub-domains are defined only to simplify the modeling by considering a single equation system for each physical variable such as velocity and temperature. Figure 4.1 shows the difference of the real domain and the domain from a FDM point of view.

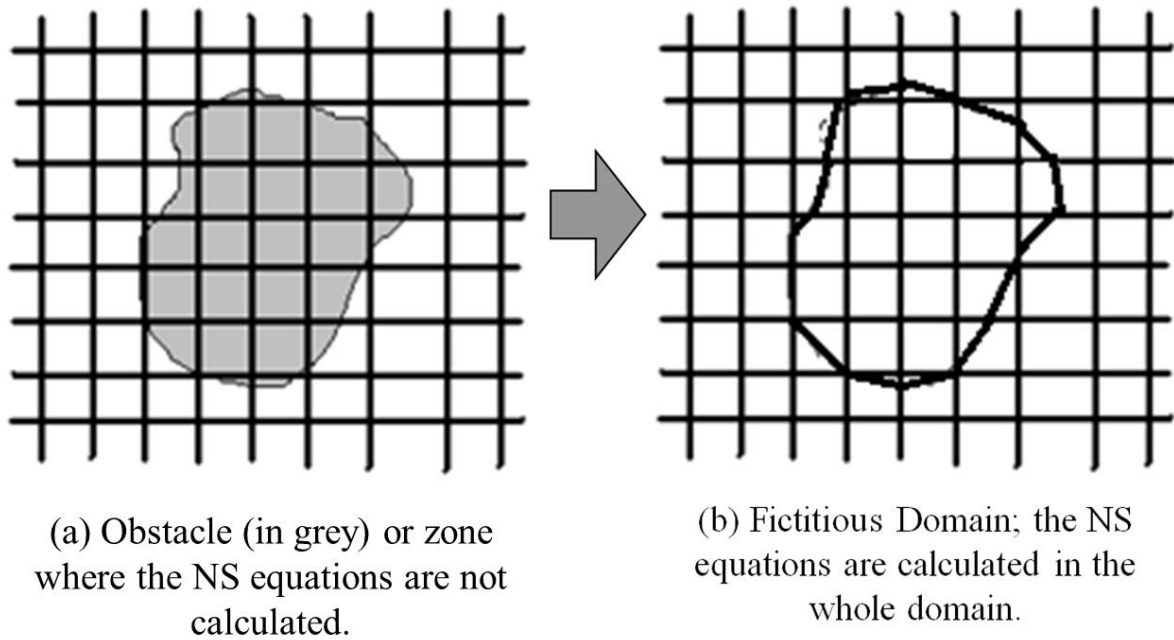


Figure 4.1 - Difference between the real domain (the physical one) and the fictitious domain (FDM).

This approach was firstly implemented at the code Thetis by Arquis and Caltagirone [88]. The single-fluid model can be tailored to this method and be used for both liquid-liquid and solid-liquid interaction. By adding a Darcy's term in the Navier-Stokes equation it is possible to treat solids as impermeable and very viscous fluids and yet having a single system of Navier-Stokes equations:

$$\frac{\partial \rho \vec{u}}{\partial t} + \nabla \cdot (\rho \vec{u} \times \vec{u}) = -\nabla p + \rho \vec{g} + \nabla \cdot (\mu_{\text{eff}} [\nabla \vec{u} + \nabla^T \vec{u}]) + \sigma \kappa n \delta_i + \frac{\mu}{K} \vec{u} \quad 4.27$$

$$\frac{K}{\mu} \left\{ \frac{\partial \rho \vec{u}}{\partial t} + \nabla \cdot (\rho \vec{u} \times \vec{u}) + \nabla p - \rho \vec{g} - \nabla \cdot (\mu_{\text{eff}} [\nabla \vec{u} + \nabla^T \vec{u}]) - \sigma \kappa n \delta_i \right\} = \vec{u} \quad 4.28$$

Where, K is the permeability of the solid. With this term, it is possible to define the position of a solid by defining its permeability or its porosity, and the continuity equation will be adapted.

4.4 Approximation of the turbulent single-fluid model

Two numerical approaches are commonly used to solve the conservation equations of incompressible flows. The main difference between them is the methodology of which they perform the velocity-pressure coupling of the Navier-Stokes equations.

The biggest difficulty comes from the presence of heterogeneities, due to the multiphase nature of the systems. The literature shows that the incompressibility constraint is very well attained when treating homogeneous and monophasic systems. Far from this ideal situations, the pressure-velocity coupling and incompressibility constrain represent a numerical issue, essentially when it comes to the resolution of linear systems.

In order to simulate multiphase incompressible flows, it is necessary to discretize the Navier-Stokes equation system from the incompressible single fluid model previously presented. We will see in this section these discretization schemes, the treatment of the incompressible constraint of the flow and which methods we selected to ensure accurate calculations in a reasonable computational cost.

4.4.1 Temporal discretization

By temporal discretization, we mean the repartition of the time axes in a finite number of time intervals (called time steps). These finite intervals may be symbolized by $[t_n, t_{n+1}]$ and the time step is noted as $\Delta t = t_{n+1} - t_n$. Each continuum variable, e.g. \vec{u} , will be noted as \vec{u}^n in its discrete form at $t = t_n$. In this manner, each continuum and temporal derivation will be approximated of the time t_{n+1} by a truncated Taylor series of order 1 (EULER scheme) or 2 (GEAR scheme) according to the precision desired.

If we discretize in time the term $\partial u / \partial t$, we obtain the general form as follows

$$\left. \frac{\partial \vec{u}}{\partial t} \right|^{n+1} = \frac{\alpha \vec{u}^{n+1} + \beta \vec{u}^n + \gamma \vec{u}^{n-1}}{\Delta t} \quad 4.29$$

where the coefficients α , β and γ allows the definition of the truncated order of the Taylor series (i.e. Table 4.4.1).

Table 4.4.1- Coefficients of the temporal discretization schemes.

	α	β	γ
Order 1 EULER	1	-1	0
Order 2 GEAR	3/2	-4/2	1/2

The second order scheme needs the allocation of more information because the access to the time t_{n-1} is mandatory, what implicates more physical memory consumption. The use of these schemes is indicated for the cases which the flow is highly transient (GEAR scheme) or stationary (EULER scheme).

The implicit treatment of the continuum system allows the expression of all the terms of the conservation equation at the time t_{n+1} , with the exception of the nonlinear advective term, which is linearized as

$$(\vec{u}^{n+1} \cdot \nabla) \vec{u}^{n+1} \approx (\vec{u}^n \cdot \nabla) \vec{u}^{n+1} = \nabla \cdot (\vec{u}^{n+1} \times \vec{u}^n) - \vec{u}^{n+1} (\nabla \cdot \vec{u}^n) \quad 4.30$$

As the numerical divergence is never null, for the incompressible flows the term $\nabla \cdot (\vec{u}^{n+1} \times \vec{u}^n) - \vec{u}^{n+1} (\nabla \cdot \vec{u}^n)$ will be spatially discretized in order to treat the nonlinearity of the advective term. If we take into account the values of the density and the viscosity at instant t_n , the discretized Navier-Stokes system becomes

$$\nabla \cdot \vec{u}^{n+1} = 0 \quad 4.31$$

$$\begin{aligned} & \rho^n \left(\frac{\partial \vec{u}}{\partial t} \right)^{n+1} + \nabla \cdot (\nabla \cdot (\vec{u}^{n+1} \times \vec{u}^n) - \vec{u}^{n+1} (\nabla \cdot \vec{u}^n)) \\ &= -\nabla p^{n+1} + \rho^n g + \nabla \cdot (\mu^n [\nabla \vec{u}^{n+1} + \nabla^T \vec{u}^{n+1}]) \\ & - \sigma^n \left(\nabla \cdot \frac{\nabla C^n}{\|\nabla C\|} \right) \nabla C^n \end{aligned} \quad 4.32$$

The pair solution to this system (\vec{u}^{n+1}, p^{n+1}) is to be determined. Many methods for uncoupling this velocity-pressure couple exist, with their pros and cons, both from a viewpoint of implementation and efficacy.

4.4.2 The incompressibility constraint – The velocity-pressure coupling

The incompressible constraint is one of the major points in the resolution of the conservation equations of motion. The velocity field at iteration t_{n+1} is the solution of two equations (4.31) and (4.32). Therefore, to respect this constraint is a coupling problem. Indeed, the pressure calculation is implicit by the pressure adjustment to the velocity field in order to the later to be divergence free, which is a crucial point. The absence of explicit formulations of the pressure p^{n+1} (only appears in the momentum equation) makes this calculation complex. Many methods were developed to solve this coupling problem, which is specific to the incompressible problems.

4.4.2.1 The projection method

For the single fluid method, the most commonly used method for the discretization is the projection method [64]. It consists of two steps of temporal integration. The first one is the velocity prediction, when the velocity field is estimated by explicitly solving the momentum equation, and the second step, called the pressure correction, is the pressure and incompressibility equation resolution.

Let Δt be the temporal discretization time step and n the reference index of the iteration of calculation in time. The pressure can be written at the time $(n+1)\Delta t$ as the sum of the pressure at the time $n\Delta t$ and a correction pressure p^* :

$$p^{n+1} = p^n + p^* \quad 4.33$$

By using Eq. (4.33) and discretizing the partial derivative in time of the velocity in a first order Euler scheme, the mass conservation and momentum equations are derived as:

$$\nabla \cdot \vec{u}^{n+1} = 0 \quad 4.34$$

$$p^n \left(\frac{\vec{u}^{n+1} - \vec{u}^n}{\Delta t} + \vec{u}^n \cdot \nabla \vec{u}^{n+1} \right) = -\nabla(p^n + p^*) + p^n \mathbf{g} + \nabla \cdot \left[\mu^n (\nabla \vec{u}^{n+1} + \nabla^T \vec{u}^{n+1}) \right] + F_V^n \quad 4.35$$

where F_V^n is the surface tension. At a first step, the velocity field is estimated by explicitly solving the momentum equation where the pressure gradient is described at time $n\Delta t$:

$$p^n \left(\frac{\vec{u}^{n+1/2} - \vec{u}^n}{\Delta t} + \vec{u}^n \cdot \nabla \vec{u}^n \right) = -\nabla p^n + p^n \mathbf{g} + \nabla \cdot \left[\mu^n (\nabla \vec{u}^n + \nabla^T \vec{u}^n) \right] + F_V \quad 4.36$$

The resolution of equation (4.36) gives an estimation of the velocity $u^{n+1/2}$ in a non-zero divergent condition. Therefore, the velocity temporal derivative should be assigned to the gradient of pressure correction:

$$\frac{\vec{u}^{n+1} - \vec{u}^{n+1/2}}{\Delta t} = -\frac{1}{\rho} \nabla p^* \quad 4.37$$

The divergence operator is applied on equation (4.37) to impose $\nabla \cdot \vec{u}^{n+1} = 0$. The pressure correction, which allows the mass conservation, is described by the Poisson equation (4.38), projecting the velocity field to a divergence free subspace of velocities. In this case, the pressure is a Lagrangian accumulation variable that accounts for incompressibility:

$$\nabla \cdot \vec{u}^{n+1/2} = \nabla \cdot \left(\frac{\Delta t}{\rho} \nabla p^* \right) \quad 4.38$$

After the prediction and projection steps, we have the velocity and pressure solutions of (4.34) and (4.35):

$$\vec{u}^{n+1} = \left(\vec{u}^{n+1/2} - \frac{\Delta t}{\rho} \nabla p^* \right) \quad 4.39$$

$$p^{n+1} = p^n + p^* \quad 4.40$$

The procedures above demonstrated the pros and cons about using the projection method, which requires a very small time step for the definition of an initial pressure field and, since the fluid flow is very unsteady, it introduces an error of consistence due to the time splitting. In addition, it requires boundary conditions to be specified for pressure, that is sometimes not straightforward. An alternative method is the Augmented Lagrangian, which is described in the following section.

4.4.2.2 The Augmented Lagrangian Method

The works from Fortin and Glowinski were reinterpreted by Caltagirone [64], Khadra [89] and Ritz [60] to give a physical meaning in the field of the fluid dynamics of unsteady compressible and incompressible fluid flow. The Augmented Lagrangian Method or Standard Augmented Lagrangian (SAL) was implemented for multiphase flows in the code Thetis by Vincent et. al [63]. The present work is based on this method.

The hypothesis of a quasi-compressible and isothermal flow, where the constraint $\nabla \cdot \vec{u} = 0$ is not satisfied, allows us to rewrite the conservation equation (4.12) in a relation that couples the velocity field and the volume force applied by the pressure on the fluid as

$$\frac{\partial p}{\partial t} + r \nabla \cdot \vec{u} = 0 \quad 4.41$$

where, r is a positive constant inversely proportional to the local compressibility coefficient. It means that a high r value indicates low compressibility of the fluid in that region. By using an Euler Scheme of first order, the time derivative of the equation (4.41) is discretized as follows:

$$\frac{p^{n+1} - p^n}{\Delta t} + r \nabla \cdot \vec{u} = 0 \quad 4.42$$

With these considerations, it is possible to couple the pressure and velocity fields in the Navier-Stokes Equations. That can be achieved by an implicit temporal integration of the momentum equation, as shown below:

$$\begin{aligned} \rho^n \left(\frac{\vec{u}^{n+1} - \vec{u}^n}{\Delta t} + \vec{u}^n \cdot \nabla \vec{u}^{n+1} \right) \\ = \nabla p^{n+1} + \rho^n \mathbf{g} + \nabla \cdot \left[\mu^n \left(\nabla \vec{u}^{n+1} + \nabla^T \vec{u}^{n+1} \right) \right] + F_V^{n+1} \end{aligned} \quad 4.43$$

The SAL method consists of replacing the implicit value of the pressure in Eq.(4.43) by a value given from Eq.(4.42) which depends on the pressure at the time $n\Delta t$ and the divergence of the velocity at the time $(n + 1)\Delta t$. So, the momentum equation takes the following form

$$\begin{aligned} \rho^n \left(\frac{\vec{u}^{n+1} - \vec{u}^n}{\Delta t} + \vec{u}^n \cdot \nabla \vec{u}^{n+1} - r \nabla (\nabla \cdot \vec{u}^{n+1}) \right) \\ = \nabla p^n + \rho^n \mathbf{g} + \nabla \cdot \left[\mu^n \left(\nabla \vec{u}^{n+1} + \nabla^T \vec{u}^{n+1} \right) \right] + F_V^{n+1} \end{aligned} \quad 4.44$$

The term $r \nabla (\nabla \cdot \vec{u}^{n+1})$ is called the **Augmented Lagrangian Term**. The major advantage of this method is that it describes implicitly the pressure and velocity in a single equation system. It is more precise than the projection method because the system is resolved in one single step and thus, generates lower residues. Hence, for a multiphase system with high density ratios, the Augmented Lagrangian is a more robust method.

4.4.2.3 Adaptive Augmented Lagrangian (AAL)

Constant values are usually attributed to r . Vincent and Caltagirone [62] showed, from numerical experiments, that to accurately solve the transport equations in the fluid zones, the optimal values of r are of the order of ρ_i or μ_i . However, high values of r can act as penalty terms, inducing the numerical solution to satisfy only the divergence free constrain [63].

If considering the very common case where water and air are taken into account, the ratio of the densities $\rho_i/\rho_j = 1000$ and if a constant value of r is used, for example $r = \rho_i$, to impose the divergence free property in the denser fluid, the asymptotic equation system solved in the predictor step is

$$\begin{aligned} \rho_1 \left(\frac{\vec{u}^{n+1} - \vec{u}^n}{\Delta t} + \vec{u}^n \cdot \nabla \vec{u}^{n+1} - r \nabla (\nabla \cdot \vec{u}^{n+1}) \right) \\ = -\nabla p^n + \rho_1 \mathbf{g} + \nabla \cdot \left[\mu^n (\nabla \vec{u}^{n+1} + \nabla^T \vec{u}^{n+1}) \right] + F_v^{n+1} \end{aligned} \quad 4.45$$

in the fluid 1's domain, Ω_1 , and

$$\frac{\vec{u}^{n+1} - \vec{u}^n}{\Delta t} - r \nabla (\nabla \cdot \vec{u}^{n+1}) = 0 \text{ in } \Omega_2 \quad 4.46$$

The idea of the AAL is to locally estimate, at each time step, the values of r based on the fluid properties in such a way that r becomes a function $r(t, R)$, where t is the time and R is the position in space. Vincent *et al* [63] affirm that the value of r must be two or three orders of magnitude higher than the highest term in the conservation equations.

Based on the AAL idea, the momentum equation can be rewritten in a non-dimensional form, considering L_0 , t_0 , u_0 , C_0 and p_0 as reference space length, time, velocity, volume fraction and pressure, respectively, as

$$\begin{aligned} \rho \frac{\vec{u}_0 \vec{u}^{n+1} - \vec{u}^n}{t_0 \Delta t} + \rho \frac{\vec{u}_0^2}{L_0} \vec{u}^n \cdot \nabla \vec{u}^{n+1} - \rho \frac{u_0}{L_0^2} r \nabla (\nabla \cdot \vec{u}^{n+1}) \\ = \rho g - \frac{p_0}{L_0} \nabla p^n + \frac{\vec{u}_0}{L_0^2} \nabla \cdot \left[\mu^n (\nabla \vec{u}^{n+1} + \nabla^T \vec{u}^{n+1}) \right] + \frac{1}{L_0^2} F_v^{n+1} \end{aligned} \quad 4.47$$

And to compare the magnitude of the Augmented Lagrangian parameter with the other terms of the equation, one can divide both sides by u_0/L_0^2 , obtaining the following equation:

$$\begin{aligned}
\rho \frac{L_0^2 \bar{\mathbf{u}}^{n+1} - \bar{\mathbf{u}}^n}{\Delta t} + \rho \bar{\mathbf{u}}_0 L_0 \bar{\mathbf{u}}^n \cdot \nabla \bar{\mathbf{u}}^{n+1} - \rho r \nabla (\nabla \cdot \bar{\mathbf{u}}^{n+1}) \\
= \rho \frac{L_0^2}{\bar{\mathbf{u}}_0} \mathbf{g} - \frac{p_0 L_0}{\bar{\mathbf{u}}_0} \nabla p^n + \nabla \cdot [\mu^n (\nabla \bar{\mathbf{u}}^{n+1} + \nabla^T \bar{\mathbf{u}}^{n+1})] + \frac{1}{\bar{\mathbf{u}}_0} F_v^{n+1}
\end{aligned} \tag{4.48}$$

It can be noticed that r is comparable to a viscosity coefficient. It is then defined as

$$r(t, R) = K_{\max} \left(\rho(t, R) \frac{L_0^2}{t_0}, \rho(t, R) \bar{\mathbf{u}}_0 L_0, \rho(t, R) \frac{L_0^2}{\bar{\mathbf{u}}_0} \mathbf{g}, \frac{p_0 L_0}{\bar{\mathbf{u}}_0}, \mu(t, R), \frac{\sigma}{\bar{\mathbf{u}}_0} \right), 10 < K < 1000 \tag{4.49}$$

With this, the AAL method ensures that the Lagrangian term is at list 10 to 1000 times higher than the other contributors to the momentum equation; inertia, viscosity, pressure and gravity, in both domains. Vincent *et al* [63] showed several examples of applications and comparisons between SAL and AAL. It turns out that, for multiphase flows, it is very important to correctly choose the value of r in order to avoid parasite currents, which deteriorate the fluid and interface prediction.

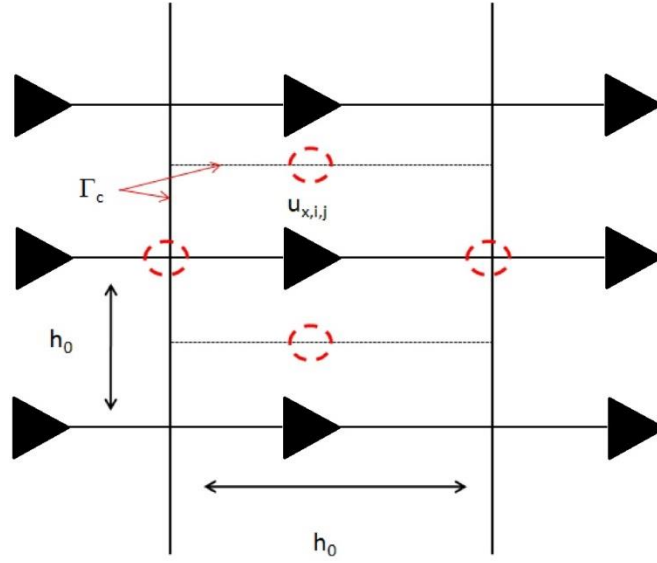
4.5 Spatial Integration

The resolution of the Navier-Stokes in the single fluid formulation with the time integration method presented will also need a spatial discretization. The code Thetis bases on a finite volume approach in the continuum phase context to discretize the domain Ω . This technique is very well adapted to take all the physical phenomena into account. The finite volume method consists in integrating the momentum equations in its conservative form in each control volume of the mesh. Therefore, to transform the integral in the control volumes, we use the divergence theorem, also known as Gauss's theorem

$$\int_{\Omega} \nabla \cdot \psi dV = \int_{\Gamma} \psi \cdot \mathbf{n}_p dS \tag{4.50}$$

Where the left hand side is a volume integral of the continuously differentiable vector field ψ over the volume V and the right hand side is the surface, Γ , integral over the boundary of the volume.

The finite volume approach consists in estimating the flux in the direction normal to the faces of the control volumes $V_{c,i,j}$ to satisfy the conservation law. To characterize the mass balance through each surface $\Gamma_{c,i,j}$, we define the space steps h_x , h_y and h_z respectively in the directions x , y and z .



⊖ Flux to be determined centered at the faces
 — Control volume associated with u_x

Figure 4.2 - Finite Volume discretization - Control volume of u_x .

To simplify the writing, the fluxes are represented in 2D and in a uniform mesh of size h_0 . If we explicit the surface integrals for each component and for each control volume, we obtain the following relations:

$$\begin{aligned}
 & \left(\frac{u_x^{n+1} - u_x^n}{\Delta t} V_{c,i,j} + u_x^n h_0 [u_x^{n+1}]_{\Gamma_{c,i}} + u_y^n h_0 [u_x^{n+1}]_{\Gamma_{c,j}} \right) - \frac{h_0}{\rho} \left(\left[\mu \frac{\partial u_x^{n+1}}{\partial x} \right]_{\Gamma_{c,i}} + \left[\mu \frac{\partial u_x^{n+1}}{\partial y} \right]_{\Gamma_{c,j}} \right) \\
 & - \frac{r' h_0}{\rho} \left(\left[\frac{\partial u_x^{n+1}}{\partial x} \right]_{\Gamma_{c,i}} + \left[\frac{\partial u_y^{n+1}}{\partial y} \right]_{\Gamma_{c,j}} \right) = \frac{h_0}{\rho} [p^n]_{\Gamma_{c,i}} + \int_{V_{c,i,j}} F_V dv
 \end{aligned} \tag{4.51}$$

$$\begin{aligned}
 & \left(\frac{u_y^{n+1} - u_y^n}{\Delta t} V_{c,i,j} + u_x^n h_0 [u_y^{n+1}]_{\Gamma_{c,i}} + u_y^n h_0 [u_y^{n+1}]_{\Gamma_{c,j}} \right) \\
 & - \frac{h_0}{\rho} \left(\left[\mu \frac{\partial u_y^{n+1}}{\partial y} \right]_{\Gamma_{c,i}} + \left[\mu \frac{\partial u_y^{n+1}}{\partial x} \right]_{\Gamma_{c,j}} \right) \\
 & - \frac{r' h_0}{\rho} \left(\left[\frac{\partial u_x^{n+1}}{\partial x} \right]_{\Gamma_{c,i}} + \left[\frac{\partial u_y^{n+1}}{\partial y} \right]_{\Gamma_{c,j}} \right) \\
 & = - \frac{h_0}{\rho} [p^n]_{\Gamma_{c,j}} + \int_{V_{c,i,j}} F_V dv
 \end{aligned} \tag{4.52}$$

$$(p^{n+1} - p^n)V_{c,i,j} + \frac{r}{\Delta t} h_0 \left([u_x^{n+1}]_{\Gamma_{c,i}} + [u_y^{n+1}]_{\Gamma_{c,j}} \right) = 0 \quad 4.53$$

The estimation of the balance of $[\psi^{n+1}]_{\Gamma_{c,i}}$ or $[\psi^{n+1}]_{\Gamma_{c,j}}$ can be described in a general manner by the difference between the quantities acting on the faces of each control volume:

$$\psi_{\Gamma_{c,i}}^{n+1} = \psi_{i+1/2,j}^{n+1} - \psi_{i-1/2,j}^{n+1} \quad 4.54$$

$$\psi_{\Gamma_{c,j}}^{n+1} = \psi_{i,j+1/2}^{n+1} - \psi_{i,j-1/2}^{n+1} \quad 4.55$$

Based on the continuity equation and the fundamental principle of the fluid dynamics, the expression (4.55) translates the flux conservation across the faces of the control volume. Every exceeding amount in one face is balanced by a losing amount in another face. Finally, we choose one discretization scheme for $\psi_{i+1/2,j}^{n+1}$ (centered, upwind or hybrid) to accurately compute the fluxes. In this study, we selected a centered scheme already implemented in Thetis in order to ensure the maximum accuracy of the calculations.

4.6 Interface Tracking Methods

4.6.1 Interface tracking with reconstruction – VOF-PLIC

In order to represent the different interfaces present in the domain, one can develop a phase function, called C , to describe the motion and the properties of the interfaces in a continuous approach in space and time. This function may have different values in the cells of the mesh for each phase, for example, to represent the liquid slag and steel flow, this function can assume for the liquid steel phase the unit value, and for the liquid slag a value equal to 0. Based on these values, one can presume that the interfaces might be in the cells whose values range between 0 and 1, precisely in $C = 0.5$.

This function can be physically interpreted as the volume fraction of a determined phase in a cell or the Volume of Fluid (VOF) as it is called. Therefore, the volume fraction needs to be transported into the domain and this can be achieved by solving its advection equation (4.14). The Navier-Stokes equation provides the velocity field, which allows the calculation of the current distribution of the phase function and its gradients in the domain as well as the physical and thermodynamic properties of the fluids.

The very abrupt changes in the phase function values and physical properties close to the interface are very difficult to reproduce numerically without loss of accuracy. If the chosen scheme is very diffusive it is possible to create some zones with numerical disturbing (nonphysical phenomena). To avoid these possible problems, it was chosen the Volume of Fluid Piecewise Linear Interface Construction (VOF-PLIC) scheme developed by Youngs *et al* [67]. The VOF-PLIC consists of a geometric linear reconstruction by pieces of the interface in each mesh cell.

4.6.2 Capillarity effects Smooth Volume of Fluid - SVOF

Because the gradients the VOF function are conceptually restricted to one cell, it is common to have the generation of nonphysical blobs when the characteristic length scale of interfaces is comparable to the local grid size. Additionally, the discretization of the surface tension model requires second order derivatives of the VOF function, and this implies that the CSF approach developed by Brackbill [61] will have incomplete local discretization compact support, i.e. the centered discretization stencil of a Laplacian operator for curvature, as C function is varying only on one cell length from 0 to 1.

To overcome this problem and complete the compact support of the discrete surface tension force from Brackbill, Pianet *et al* [59] proposed the usage of an auxiliary Smooth VOF (SVOF) function, called C^S , which is obtained from the function C of the VOF model, but do not replace this sharp function, to ensure the right mass conservation achieved with the PLIC numerical algorithm of Youngs *et al*. [67]. Moreover, the new function C^S have to match the value $C^S = 0.5$ with $C = 0.5$, and then the averaging procedures required to build ρ and μ can be based on C^S and will characterize the same fluid sub-domains as C .

The basic idea which leads to the development of the SVOF came from an analogy with the unsteady diffusion equation used to compute thermal transfers:

$$\frac{\partial T}{\partial t} + \nabla \cdot a \nabla T = 0 \quad 4.56$$

where $a > 0$ is the diffusivity coefficient. It is known that the diffusion length δ is equal to $\sqrt{a\tau_d}$, where τ_d is the characteristic time scale of diffusion. Assuming $a = 1$, τ_d and δ^2 are of the same order. If Eq. (4.56) is discretized in time, it becomes

$$-\nabla \cdot \tau_d \nabla T^{n+1} + T^{n+1} = T^n \quad 4.57$$

When Eq. (4.57) is solved N times, with $1 \leq n \leq N - 1$, $\tau_d = N\Delta t$ and the initial temperature field $T^0 = C$, it is ensured that T diffuses on a length equal to δ and that $T = T^0$ far from the diffusion zone; the zone where temperature gradients are zero [59].

By analogy, the SVOF consists of creating a smooth VOF function, C^S , by iteratively solving the Helmholtz equation with the initial condition $C^{S_0} = C$, the sharp function:

$$-\nabla \cdot D \nabla C^{S,n+1} + C^{S,n+1} = C^{S,n} \quad 4.58$$

Where D is the diffusion coefficient equals to $L_i \Delta h^2$. This parameter is fixed in order to ensure that the VOF function C^S spreads over a distance L_i on each side of the interface, where $C^S = C = 0.5$. The coefficient Δh is the local characteristic size of the grid cell.

An example of SVOF function obtained on a grid sample is presented in Figure 4.3, from the works of Pianet *et al* [59]. This figure compares functions C and C^S , where it is demonstrated that iso-line $C^S = 0.5$ is smoother than $C = 0.5$ and that the diffusion zone associated to C^S following the normal to the interface is of regular thickness.

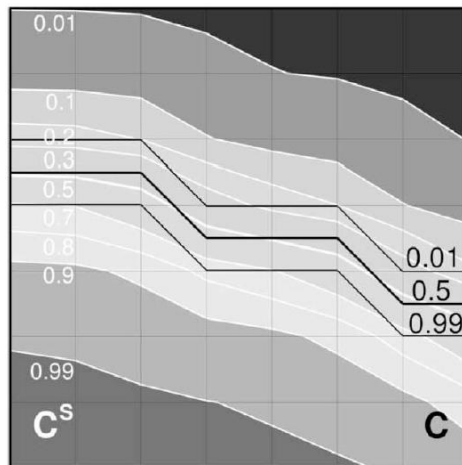


Figure 4.3 - Comparison of SVOF and VOF iso-surfaces by Pianet *et al* [59].

4.7 Conclusion

In this chapter, we presented a few methodologies to model multiphase flows for numerical simulations. Since we are concerned about the mass transfer phenomenon with resolved scale interfaces, which occurs at multiphase interfaces, it is of major importance to select the methods that produce the least numerical and interface thickness diffusion in the regions close to the interface. The code Thetis is used in this work. The Navier-Stokes equations are spatially discretized based on the finite volume approach and solved with a centered scheme.

The Adaptive Augmented Lagrangian (AAL) method is used for the velocity-pressure coupling, since we believe it is the most robust method to be used when high density/viscosity ratio are present. The interfaces are tracked with the VOF-PLIC method and the capillary effects are taken into account by the SVOF. The fluid physical properties at the interface are computed with an arithmetic average for the density and harmonic average for viscosity. To have a detailed description of the turbulence in an affordable time, we used the LES turbulence model with a Mixed SGS model for the interactions between the different scales present in the flow. The results of the simulations will be presented in subsequent chapters.

5 Continuous Casting – Hydrodynamic Characterization

In this chapter we will present the experimental and numerical results. The main validation concern was the velocity at the interface region. The description of the velocity field close to the interface must be precise since the mass transfer models we aim at implementing are based on these local parameters.

The water model described in Chapter 3 was adapted. To achieve good interface stability with a mold width corresponding to an industrial configuration, the SEN was moved towards the side wall as shown in Figure 5.1. We proceeded by measuring the horizontal and vertical components of the velocity field with the LDA technique explained in Chapter 3. The velocities were measured during 10 minutes with an average data frequency acquisition of 80 Hz for each point. We believe this time is sufficient to capture all the phenomena involved, including those with low frequencies. The mean velocities and random mean square (rms) were calculated. The measurement position is indicated in Figure 5.1 and was taken at the symmetry plane in the z direction. The experimental conditions are detailed in Table 5.1.

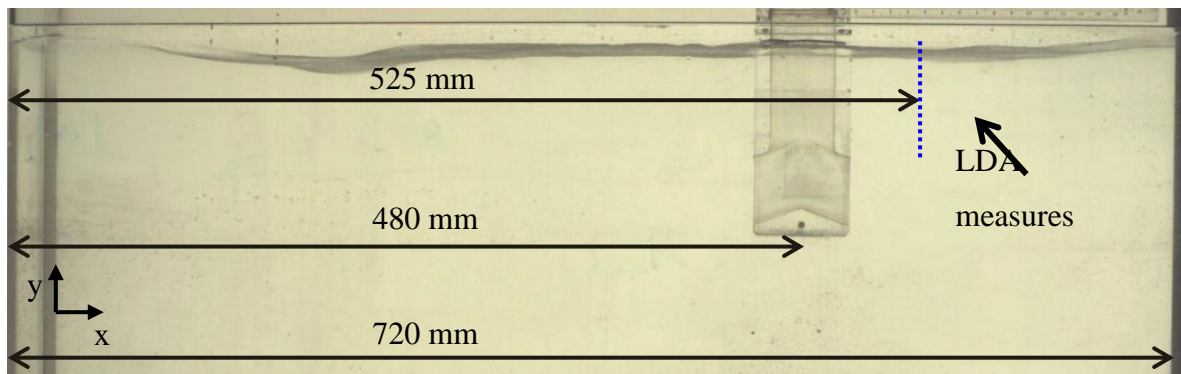


Figure 5.1- Schematic view of the water model configuration.

Table 5.1 - Experimental conditions and physical properties.

Mold Size	720 _w x100 _t mm	
Water Flow Rate, Q	1.60 and 2.00 m ³ /h	
Nozzle Depth, h _w	68 mm	
Oil layer thickness, h _o	4.0 and 15 mm	
Physical Properties of the Oil Layer	Silicon Oil A	$\rho = 950 \text{ kg.m}^{-3}$ $\nu = 20 \text{ cSt}$
	Silicon Oil B	$\rho = 970 \text{ kg.m}^{-3}$ $\nu = 350 \text{ cSt}$

Due to difficulties intrinsic to the technique, the velocities at the exact interface position could not be measured. A distance of less than 1.0 mm was achieved for the horizontal velocities and we are going to consider the first measure point as the interface average position. In the case of the vertical velocities, the minimum distance from the first measure point to the interface was about 3.0 mm. This distance is due to the laser beams angle as shown in Figure 5.2, which illustrates the location of the closest vertical component measured. The distance measured between the two laser beams at the external mold wall is 6 mm, hence, by geometric approximation we conclude that the distance from the volume of measure to the interface is half the external distance of the laser beams.

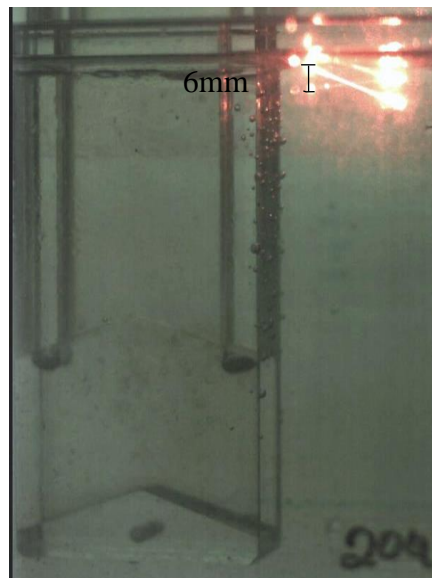


Figure 5.2 - LDA limit for the vertical velocity.

During this first set of experiments we analyzed the effects of water flow rate (simulating different casting speeds), oil layer viscosity (simulating different slag viscosities), and the oil

layer thickness (to evaluate the influence of the slag volume). The results are presented in the next sections.

5.1 Experimental Analysis

5.1.1 Effect of water flow rate

At the oil/water interface, the oil layer acts as a stagnant phase at the top of the water field. Its presence will change the conditions from a nearly zero stress ($\partial U/\partial y = 0$ for air/water interface) to one of wall bounded flow like. In consequence, the viscous oil layer offers much more resistance to the flow, producing a boundary layer close to the interface, as schematically shown in Figure 5.3.

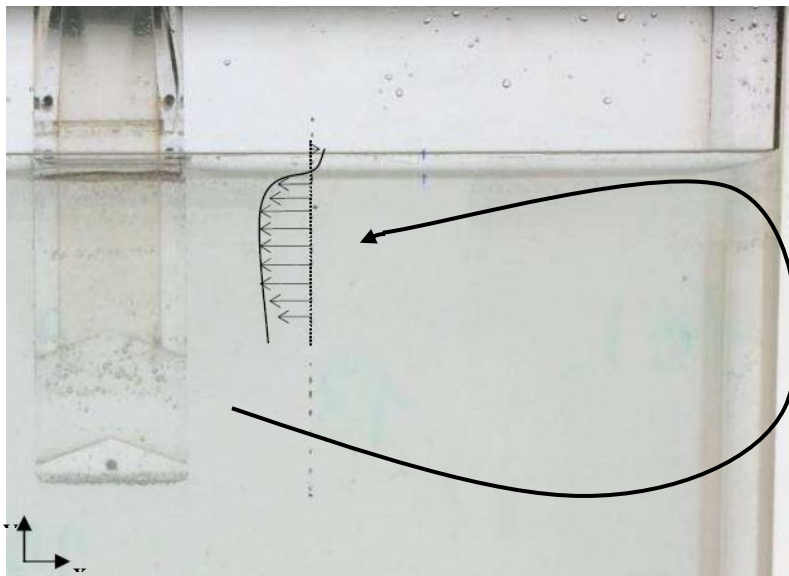


Figure 5.3 - Schematic view of the horizontal velocity profile with the boundary layer close to the interface.

Measurements have shown that, for both oils, an increase in the water flow rate will increase the horizontal velocities in the bulk flow and the turbulence intensity, estimated by the rms of the measured velocities, as shown in Figure 5.4 and Figure 5.5. One should note the high values found for the measured rms. These values are going to be further examined later in this chapter. The increase in the water flow rate also promoted an increase of the shear stress, which we considered as $\tau = \mu \partial U/\partial y$, where μ is the water molecular viscosity. The water

flow rate did not present any effect on the vertical component, apart from the turbulence enhancement, as observed in Figure 5.6 and Figure 5.7

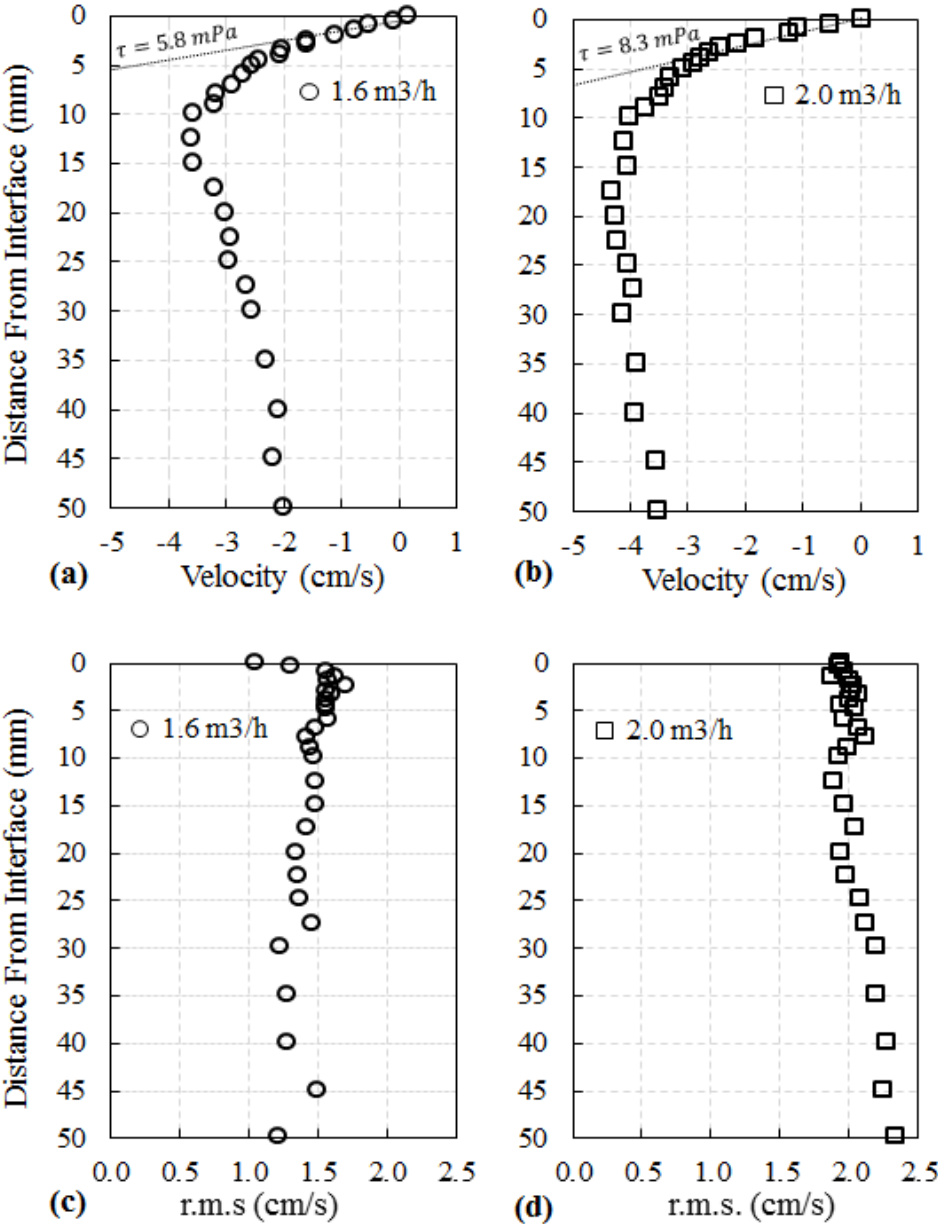


Figure 5.4 - LDA measures of the horizontal component of the velocity field with Oil A (350 cSt). Mean values from the water flow rate $Q=1.6$ and $2.0 \text{ m}^3/\text{s}$ are presented in (a) and (b), respectively. The r.m.s. values are displayed at (c) and (d).

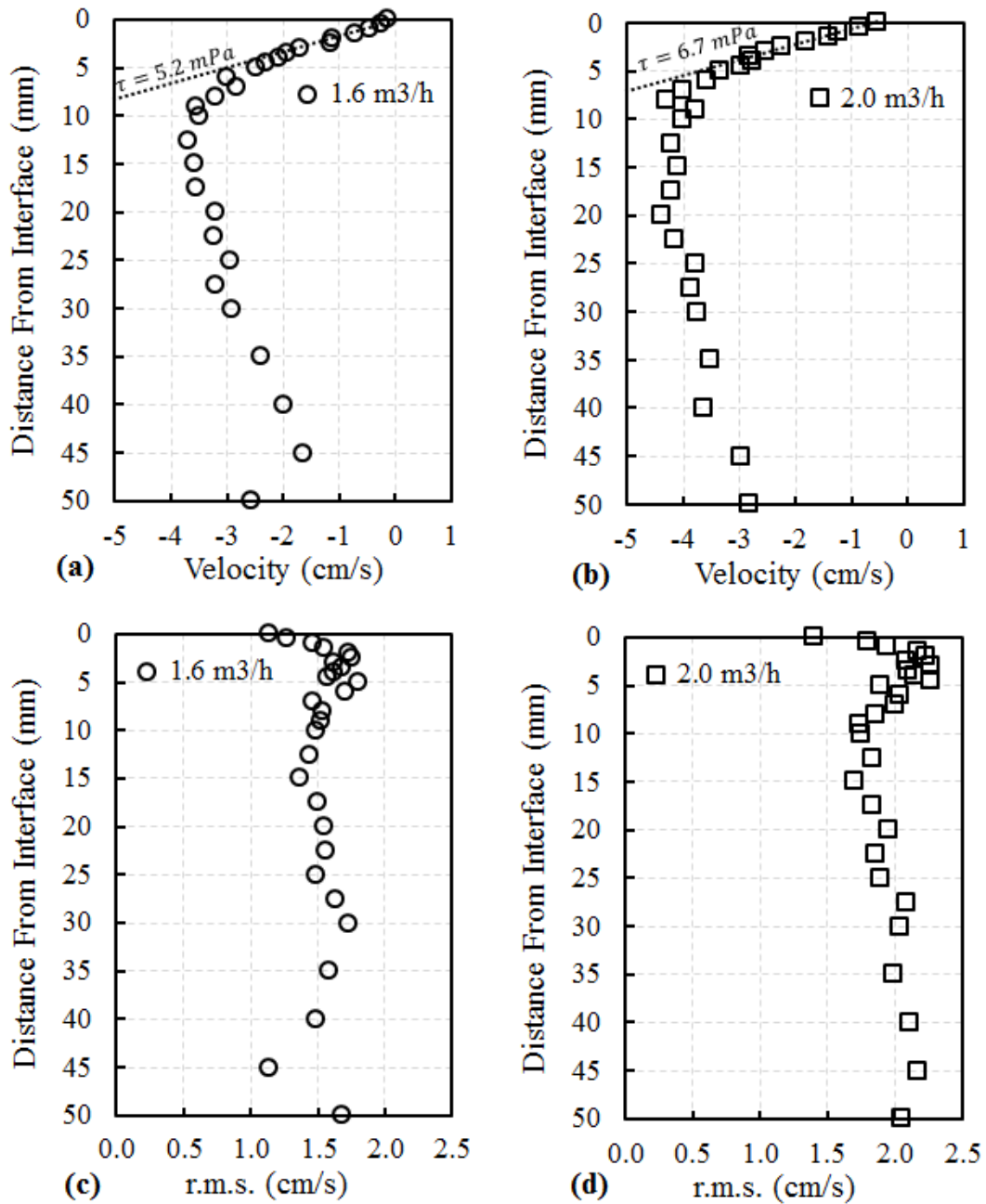


Figure 5.5 - LDA measures of the horizontal component of the velocity field with Oil B (20 cSt). Mean values from the water flow rate $Q=1.6$ and $2.0 \text{ m}^3/\text{s}$ are presented in (a) and (b), respectively. The r.m.s. values are displayed at (c) and (d).

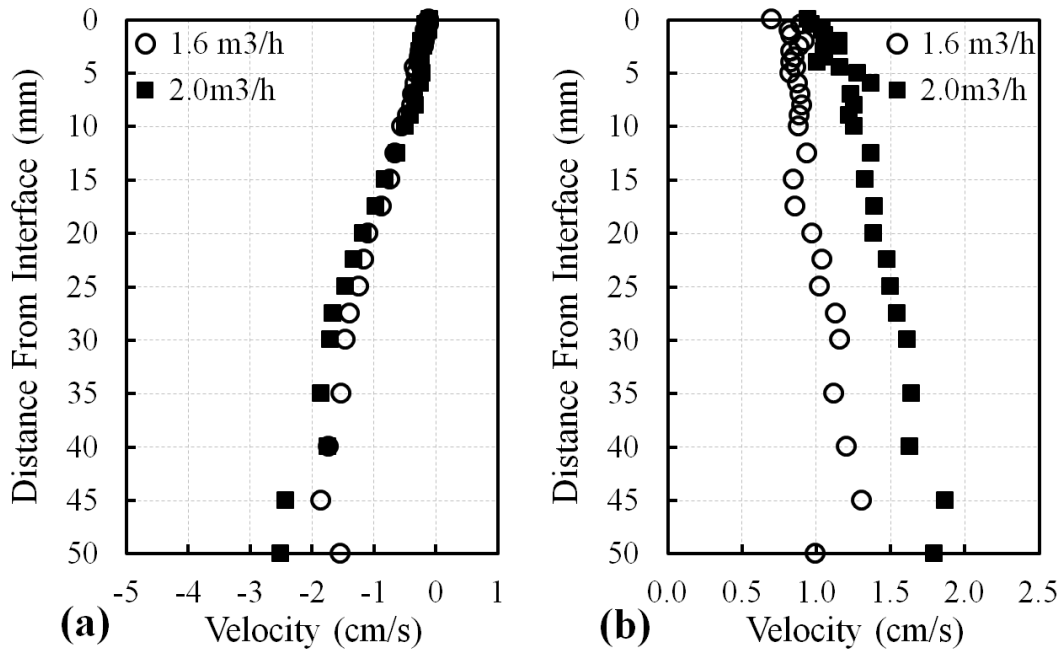


Figure 5.6 - LDA measures of the vertical component of the velocity field with Oil A (350 cSt). Mean values from the water flow rate $Q=1.6$ and 2.0 m³/s are presented in (a) and the r.m.s. values are displayed in (b).

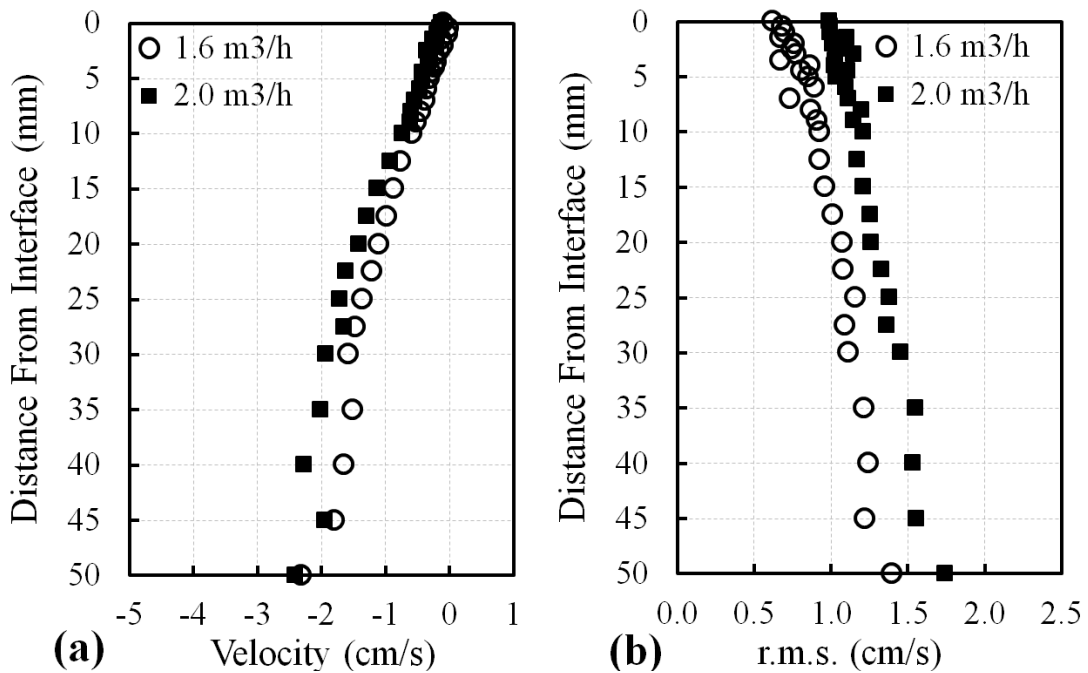


Figure 5.7 - LDA measures of the vertical component of the velocity field with Oil B (20 cSt). Mean values from the water flow rate $Q=1.6$ and 2.0 m³/s are presented in (a) and the r.m.s. values are displayed in (b).

We found a boundary layer near the liquid/liquid interface of these configurations. The main difference of this boundary layer with a wall boundary layer is the rms value, which is null in the second case but keeps an almost stable value at the water/oil interface. Even though the

mean horizontal velocities at the liquid/liquid interface are slim to none, there is, indeed, some oscillatory movement at the interface, which is one of the reasons for the rms values higher than mean velocities. We will discuss more about these oscillations in the following sections.

In both, horizontal and vertical velocity components, the increase of the water flow increased the fluctuations in the velocity values (rms), which suggests that the turbulence intensity should somehow correlate to the flow rate into the mold.

5.1.2 Effect of oil layer viscosity

We evaluated the effect of the oil layer viscosity in both water flow rates. It was found that, for the lowest water flow rate ($Q = 1.6 \text{ m}^3/\text{h}$), the oil layer viscosity has no substantial influence on the flow near the liquid/liquid interface nor on the turbulence intensities of the system (Figure 5.8). However, in the highest water flow rate, $Q = 2.0 \text{ m}^3/\text{h}$, we verified a slight increase in the shear stress when increasing the oil layer viscosity (Figure 5.9 (a) and (b)). Moreover, the oil layer viscosity has no effect on the turbulence intensity even in the highest water flow rate experiments (Figure 5.9 (c) and (d)).

In a real process, when the shear stress is high enough, the molten metal carries some slag droplets to the bulk flow [90]. These slag droplets if big enough will float to the interface otherwise they will be captured by the solidifying shell and form the undesirable inclusions which are detrimental to the steel performance. We have seen that in high turbulence regimes, the shear stress at the interface is more sensitive to changes in the upper phase viscosity. During the casting, the flow reaches very high turbulence regimes in order to improve productivity. In such cases, the slag chemical composition may vary due to mass transfer from the molten steel to the slag and vice versa, altering the viscosity of the slag phase and changing the shear at the liquid steel/slag interface. Therefore, the present results show the importance of controlling slag viscosity to prevent inclusions entrapment and ensure the appropriate mold lubrication.

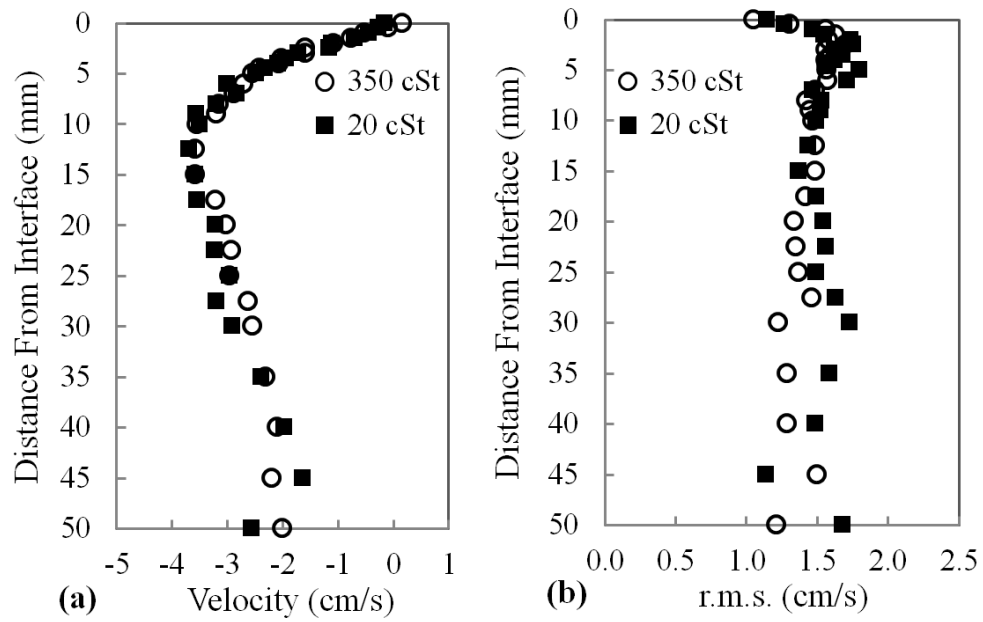


Figure 5.8 - LDA measurements of the horizontal component of the velocity field with the lowest water flow rate, $Q = 1.6 \text{ m}^3/\text{h}$. Mean values from the configuration with oil viscosities $\nu = 20$ and 350 cSt are presented in (a) and the r.m.s. values are displayed in (b). No remarkable influence is found.

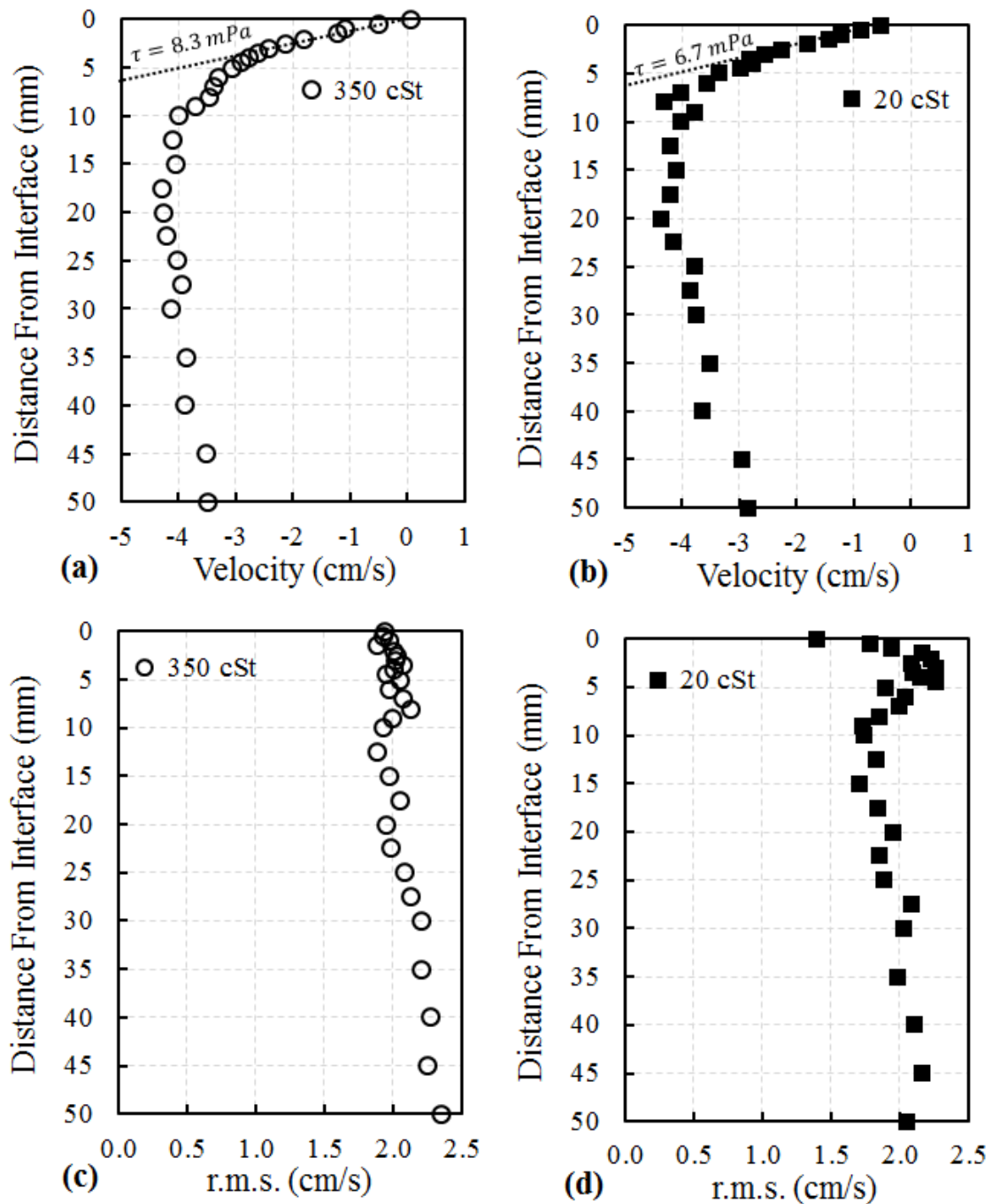


Figure 5.9 - LDA measurements of the horizontal component of the velocity field with the highest water flow rate, $Q = 2.0 \text{ m}^3/\text{h}$. Mean values from the configuration with oil viscosities $\nu = 350$ and 20 cSt are presented in (a) and (b) respectively. The r.m.s. values are displayed at (c) and (d).

A negligible effect of the oil viscosity was observed on the vertical velocity component, as shown in the figures below:

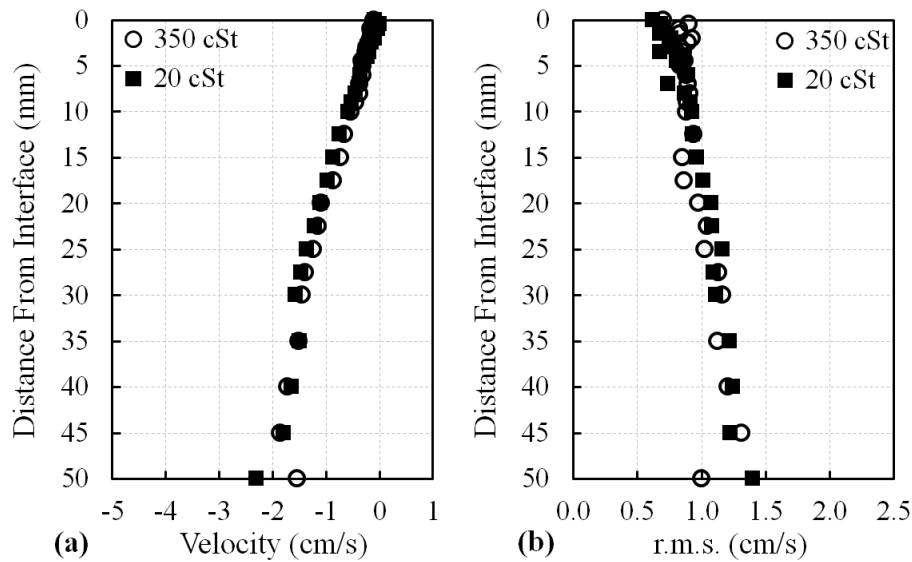


Figure 5.10 - LDA measurements of the vertical component of the velocity field with the lowest water flow rate, $Q = 1.6 \text{ m}^3/\text{h}$. Mean values from the configuration with oil viscosities $\nu = 20$ and 350 cSt are presented in (a) and the r.m.s. values are displayed in (b).

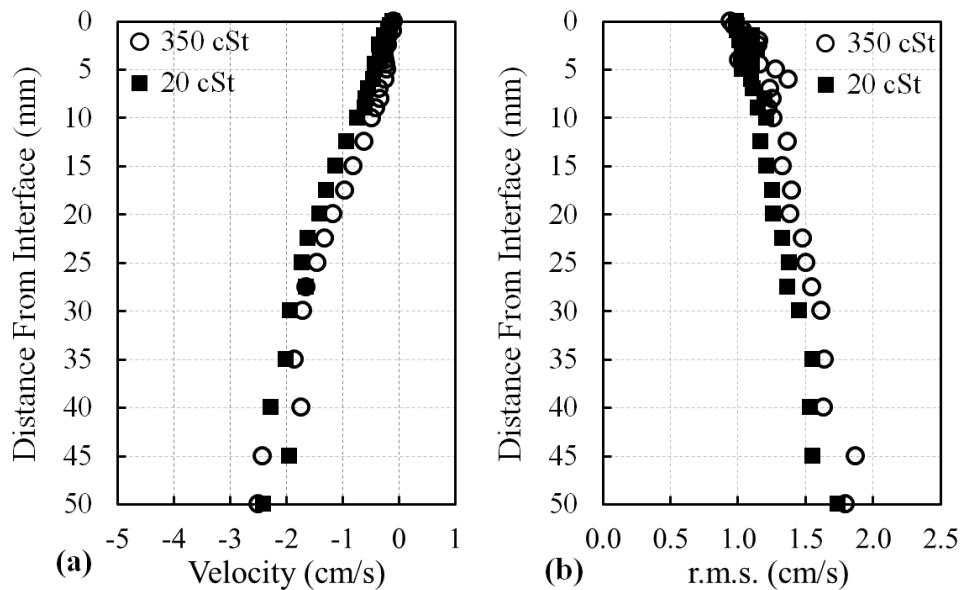


Figure 5.11 - LDA measurements of the vertical component of the velocity field with the lowest water flow rate, $Q = 2.0 \text{ m}^3/\text{h}$. Mean values from the configuration with oil viscosities $\nu = 20$ and 350 cSt are presented in (a) and the r.m.s. values are displayed in (b).

5.1.3 Effect of oil layer thickness

The velocity fields measured with an oil layer of 4.0 mm and 15 mm thickness were compared. We performed the measurements with both water flow rates. The shear stress was found to be higher in the region near the interface of the thinner oil layer for the lowest water flow rate, as shown in Figure 5.12:

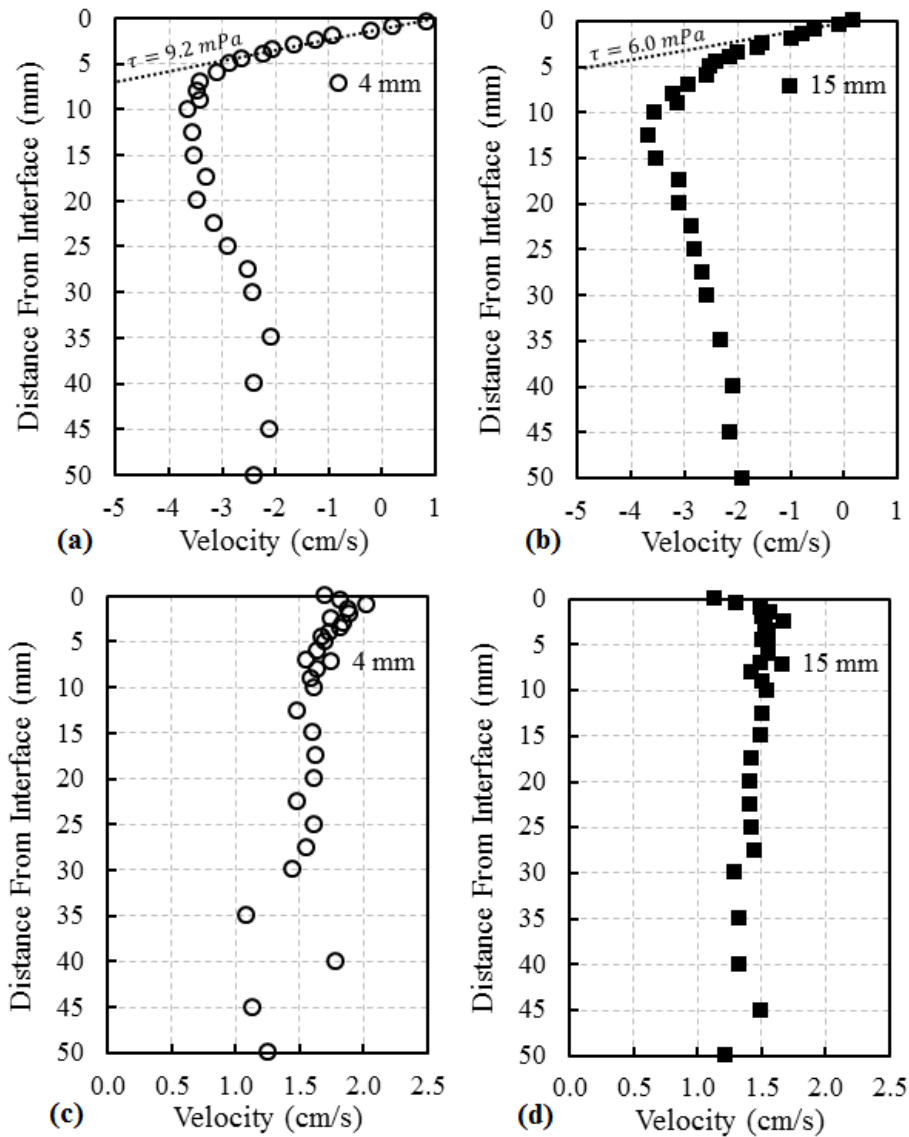


Figure 5.12 - LDA measures of the horizontal component of the velocity field with the lowest water flow rate, $Q = 1.6 \text{ m}^3/\text{h}$ with oil layer viscosity $\nu = 350$. Mean values from the configuration of 4 and 15 mm oil layer are presented in (a) and (b) respectively. The r.m.s. values are displayed at (c) and (d).

The higher shear stress found at the configuration with 4.0 mm oil layer thickness is due to the presence of a recirculation zone encountered near the SEN, as schematically displayed in Figure 5.13 (a). The recirculation zone is indicated by the sudden change in the sense of the horizontal component (from negative to positive relative to the axis direction).

The counter-flow, from the mold left side, acts as a barrier to the average flow at the mold right side in such a way that the averaged flow at each side is similar to that inside a cavity. This barrier effect creates a stagnant zone around the SEN, and its size may vary according to the flow rate intensities and even oscillate with the jet fluctuations (we are going to discuss

more about the jet fluctuation later). The CFD model provided the necessary insights to explain these phenomena and its results will be presented in the following sections.

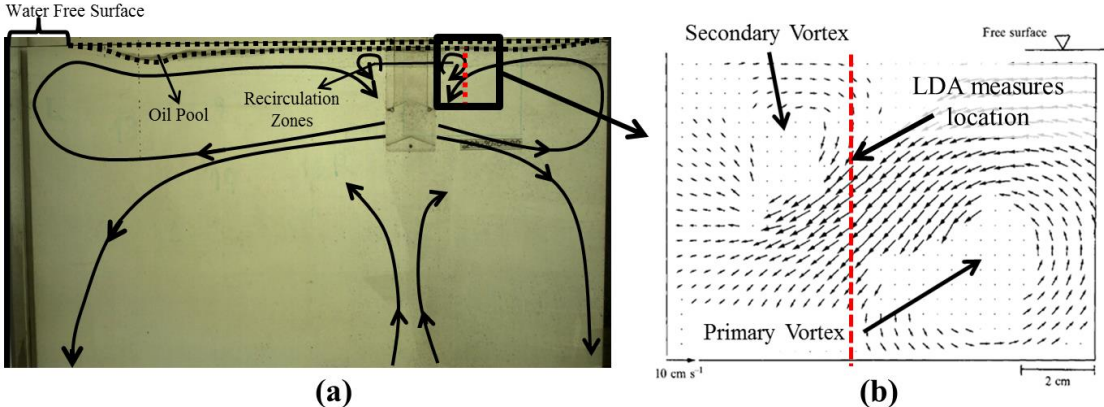


Figure 5.13 - Schematic view of the flow at the regions where the velocity measures were taken.

Another phenomenon occurs when the oil layer is not sufficiently thick or the flow velocity is too high; the water flow pushes the oil layer away from the lateral walls and creates oil pools and water free surface regions. These oil pulls change the flow, anticipating the position where the flow is detached from the interface. This flow detachment generates a small vortex with opposed direction to the flow (Figure 5.13 (a) and (b)). If the flow is higher, e.g. 2.0 m³/h, it pushes the recirculation zone towards the SEN, and no recirculation zone was observed at the position where the measurements were taken, as schematically shown in Figure 5.14.

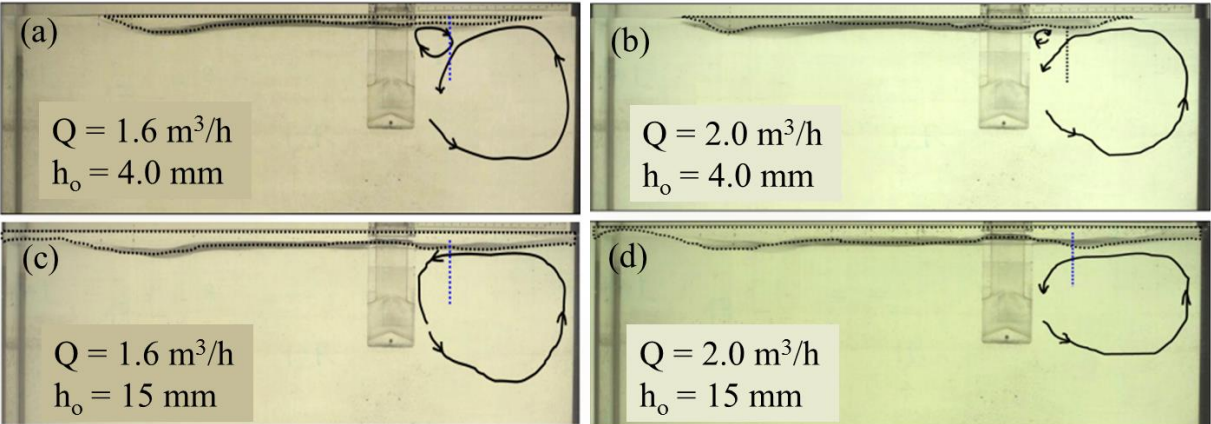


Figure 5.14 – Schematic view of the effects of oil layer thickness on the flows near the interface region where the LDA measures were performed.

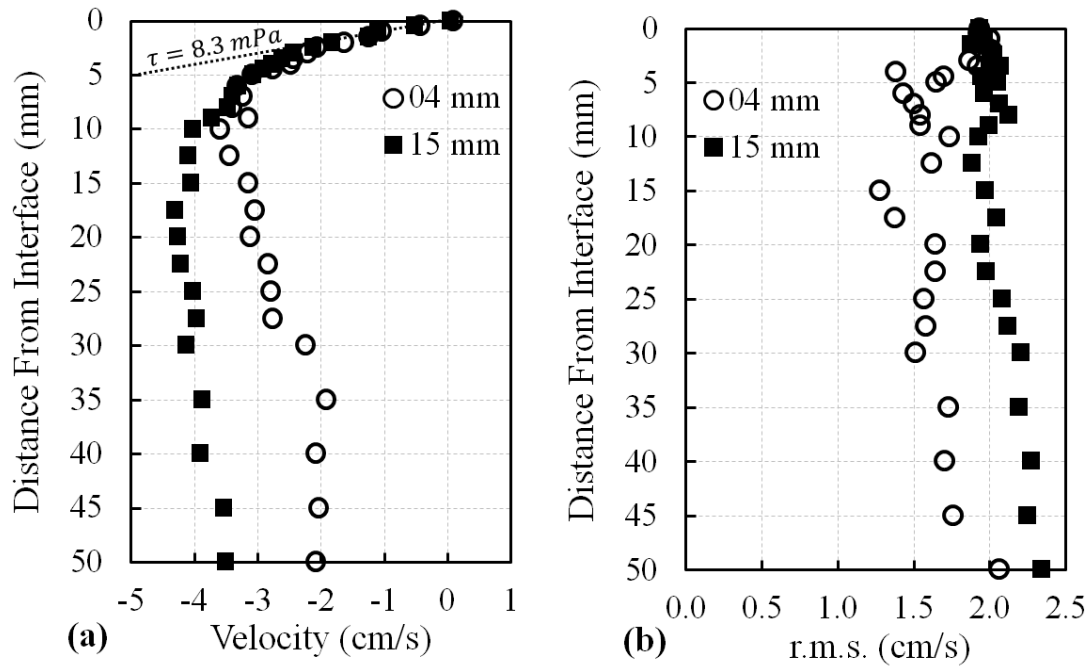


Figure 5.15 – Velocity profiles and rms for different oil layer thickness. The water flow rate is $Q = 2.0 \text{ m}^3/\text{h}$ and the oil viscosity is $\nu = 350 \text{ cSt}$.

Figure 5.15 shows that, for the highest water flow rate, the shear stresses are the same no matter the thickness of the oil layers. However, the horizontal velocities in the bulk flow are attenuated with the 4 mm oil layer configuration. That can be explained by the flow behavior observed, which was schematically illustrated above, in Figure 5.14 (b) and (d), where we can see a more vertical flow due to the interface shape. In this case, the horizontal component is slightly reduced and the vertical component increases.

In Figure 5.14 (a) and (b), one can note that with high water flow rates the water free surface is increased and the recirculation zone is pushed towards the SEN in a region outside the LDA location. The difference in the measures taken with the recirculation zone and without can be observed in the vertical velocity components (Figure 5.16). The velocity fluctuations are higher close to the interface with the recirculation zone and the mean velocity does not present the linear evolution found in all the cases without this recirculation zone.

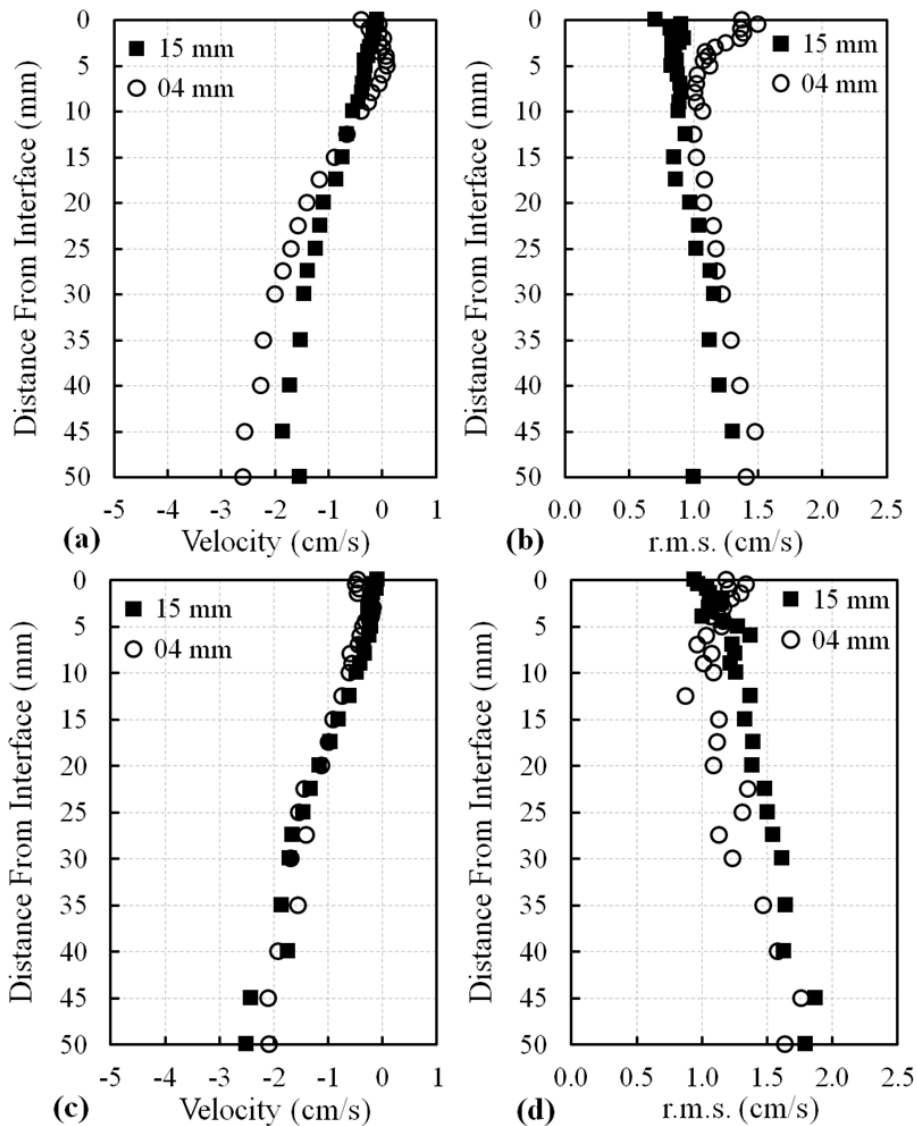


Figure 5.16 – LDA measures of the vertical velocity components, V , with different oil layer thickness for $1.6\text{m}^3/\text{h}$ (a-b) and $2.0\text{m}^3/\text{h}$ (c-d) water flow rate and oil layer viscosity $\nu = 350$ cSt.

5.1.4 Conclusions

During these preliminary experiments, we evaluated the effect of the water flow rate, oil layer viscosity and oil layer thickness on the interface behavior and interface shear. However, the evaluation was performed in a single point and may not be representative of the effects on the water/oil interface as a whole. Only the CFD could provide such analysis and we will evaluate these effects in the following sections after discussing about the CFD results. In summary, the LDA measures suggest the effects above:

Water Flow Rate

- An increase in the water flow rate would increase the shear stress at the interface.

- Increasing the water flow rate would increase the turbulence in the system no matter the oil layer thickness.

Oil Layer Viscosity

- Increasing the oil layer viscosity would increase the shear stresses at the interface.
- The oil layer viscosity would not have any influence on the turbulence of the system.

Oil Layer Thickness

The oil layer thickness would have a huge effect on the flow at the upper part of the mold and this effect must be analyzed according to the water flow rate:

- Low water flow rates:
 - When there is a low flow rate, the oil layer thickness may have no effect on the mean velocities in the bulk flow.
 - However, for a thin layer, a recirculation zone may be created. In this case, the interface shear would be locally intensified.
- High water flow rates:
 - When the water flow is sufficiently high, the recirculation zone may be compressed towards the SEN or even suppressed. Without the presence of this vortex, the oil layer thickness may have no effect on the interface shear.

5.2 Proposed configuration for mathematical modeling

Based on the stability found in the mold right side interface, we decided to reduce the mold width, keeping a symmetric SEN position based on its dimensions. To avoid high interface oscillations, we used the most viscous oil (350 cSt) and we chose an intermediate oil layer thickness (as compared to the previous 04 and 15 mm), here defined as 10 mm. As the lower water flow rate is sufficient to produce shear at the interface and provide turbulence to the system, we decided to run the new trials with the lower water flow rate (1.6 m³/h). The new configuration is represented in Figure 5.17 and Table 5.2 below. With this configuration, the interface was sufficiently stable, therefore we could take measurements in two different positions, e.g. 3.5 and 7.0 cm to the right of the SEN.

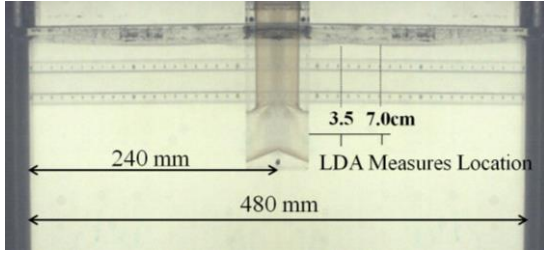


Figure 5.17 - Physical apparatus with the indication of the LDA measurement position and a schematic view of the average flow pattern in CC mold.

Table 5.2 - Experimental conditions and physical properties.

Mold Section Area (WxT)	480 _w x100 _t mm ²
Water Flow Rate, Q_w	1.60 m ³ /h
Nozzle Depth, h_w	60 mm
Oil layer thickness, h_o	10 mm
Silicon Oil Layer	$\rho = 970 \text{ kg/m}^3$ $\nu = 350 \text{ cSt}$

The CFD model was built based on this configuration and we are going to refer to it as the water oil interface (WOI) configuration. Trials were also performed without the oil layer and we will refer to this configuration as the water free surface (WFS) configuration. The interest in these two configurations is explained by the different aspects found in an industrial case. In the liquid steel/slag interface there is high viscosity and density ratios, with the upper phase being the more viscous one. Thus, the WFS provide us the high density ratio case and the WOI interface the high viscosity ratio. Combining the features found in both configurations we may have a good understanding of the liquid steel/slag interface hydrodynamics.

The results of the experimental and the CFD simulations are presented in the next sections.

5.3 Interface Characteristics

The dynamics of deformable interfaces are intimately linked with the nature of the flow below it. Waves may be developed depending on the intensity of the interfacial shear stress caused by the underlying turbulence. Brocchini & Peregrine [91] [92] showed that the action of this shear is balanced by two stabilizing factors: one due to gravity and one caused by surface tension.

To characterize these wavy interfaces, it is used the second moments of the joint probability density of the surface displacement $P(f(x_1), f(x_2))$. We define the covariance or autocorrelation function of the interface displacement at a fixed location as a function of time:

$$Z(t) = \overline{f(x, t_0), f(x, t_0 + t)} \quad 5.1$$

A more complete method to characterize it is by analyzing the spectral signal of the interface displacement. We measured the water/oil interface displacement with the EIT technique developed and described in Chapter 3. The water/oil interface measure was performed at the same position where the LDA measures were taken, *i.e.* 3.5 and 7 cm from the right of the SEN and they were performed during 10 minutes to ensure the measure of all the low frequency phenomena. The maximum wave amplitude observed in the WOI experiments and simulations was 2 mm and very low perturbation was found in the WFS configuration. Thus, we will not consider the WFS configuration for the interface characterization.

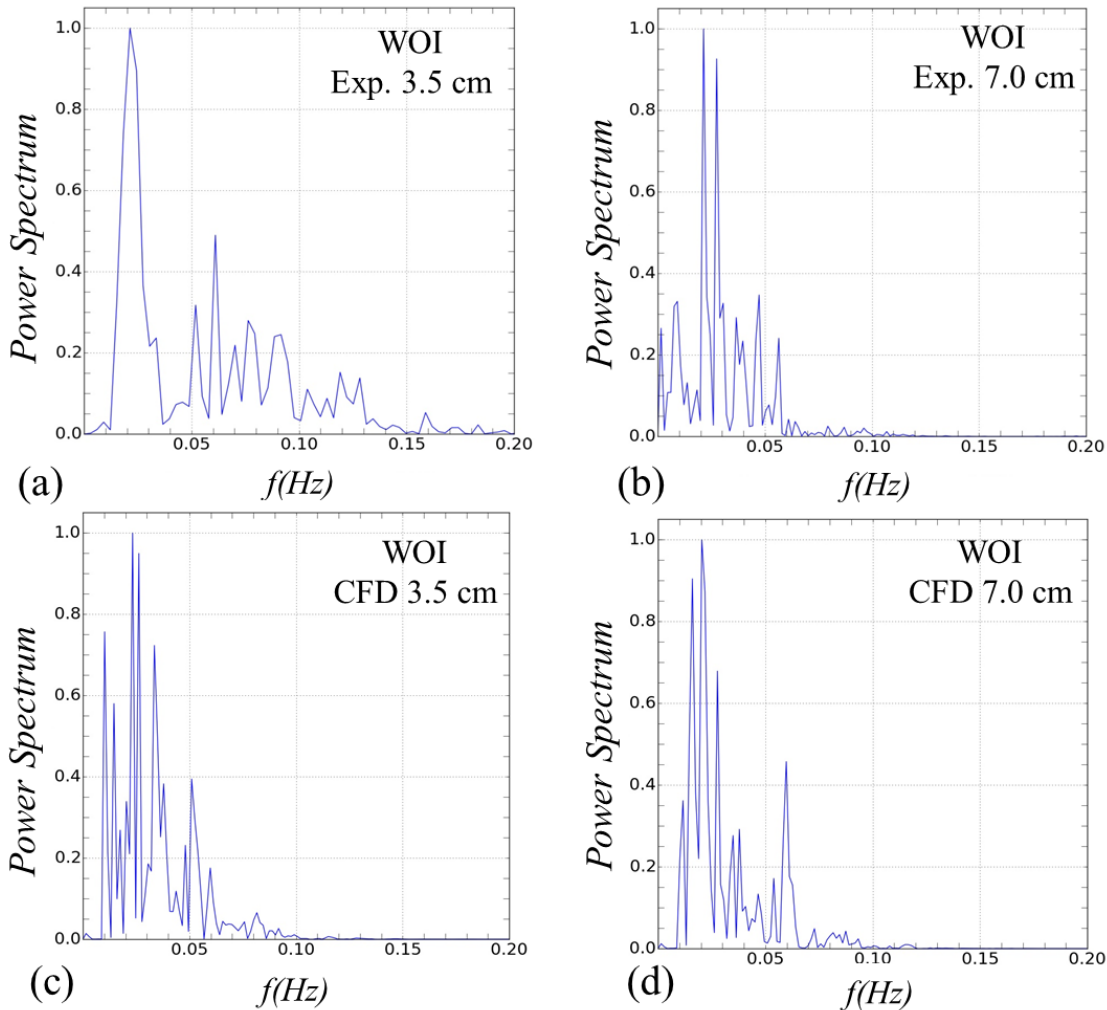


Figure 5.18 – Normalized spectrum of the interface displacement in the WOI configuration. Figures (a) and (b) concern the interface displacement in the experimental model. Figures (c) and (d) show the interface displacement in the mathematical model.

We define the integral time scale with the characteristic frequency, which is determined by the highest peak that indicates the frequency of the dominating wave. It is seen that the

dominating frequencies found in both positions are roughly the same and about 0.020 to 0.025 Hz, indicating a time scale of approximately 40 to 50 seconds (Figure 5.18). This time indicates that, if we want to accurately describe the low frequency phenomena, we may need to have more than, let's say, five times the characteristic time, which means a simulation time of 250 seconds. However, 90 days of calculation time on 128 processors did not exceed 170 seconds. This time may not be sufficient to have accurate data to fully describe the physical phenomena observed, but may afford sufficient data to analyze the hydrodynamics of this liquid/liquid interface. The mathematical results indicate a characteristic period of the interface waves of about 50 seconds, in good agreement with the values from experiments.

5.4 Mean Flow Description

The time averaged data from LDA measures and CFD calculations were compared for validation. In this case, the CFD code computed 170 seconds of physical time with a time step of 1×10^{-4} seconds between iterations and a sampling frequency of 0.1 seconds whilst the LDA measures were taken over 600 seconds in each position.

5.4.1 Water Oil Interface (WOI) configuration

The velocity fields of the experiment and its respective simulation are shown in Figure 5.19 to Figure 5.22. The maximum horizontal velocity is reached at about 10 mm from the interface, and then is dissipated in a viscous boundary layer close to the water/oil interface. The flow close to the interface is predominantly horizontal, with very low perpendicular component. Good agreement was found between the CFD and the experimental data.

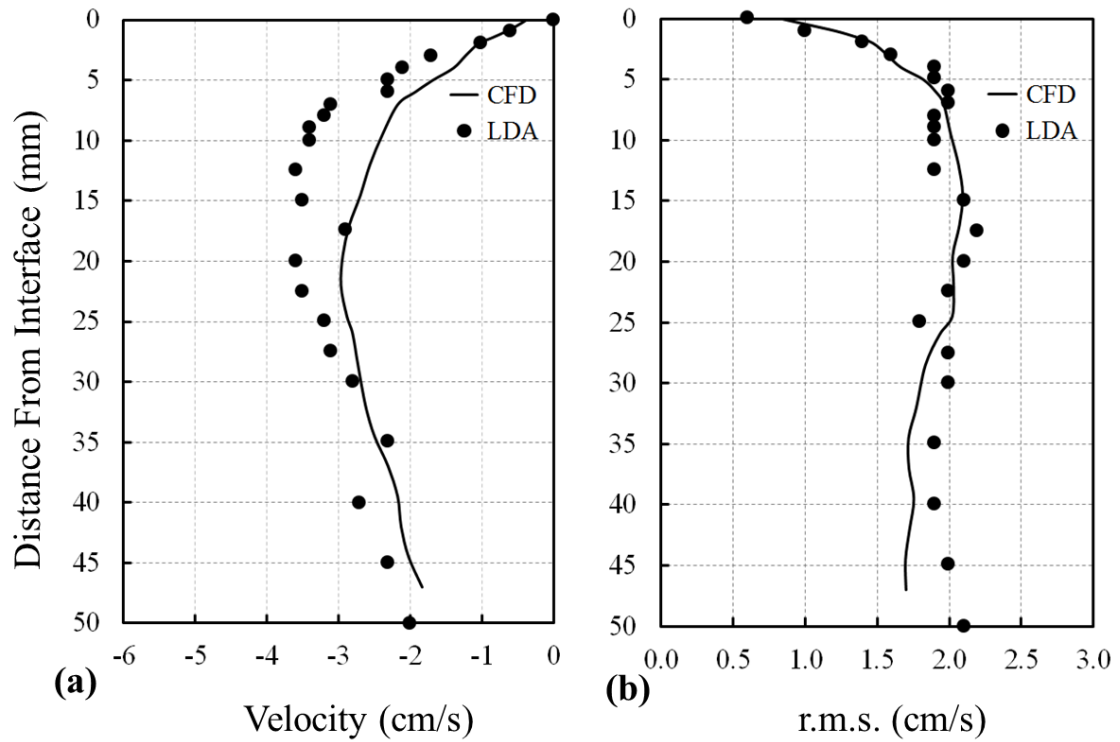


Figure 5.19 - Velocity field of the WOI experiment vs CFD at 3.5 cm from the SEN. (a) shows the streamwise component and its rms values are displayed in (b).

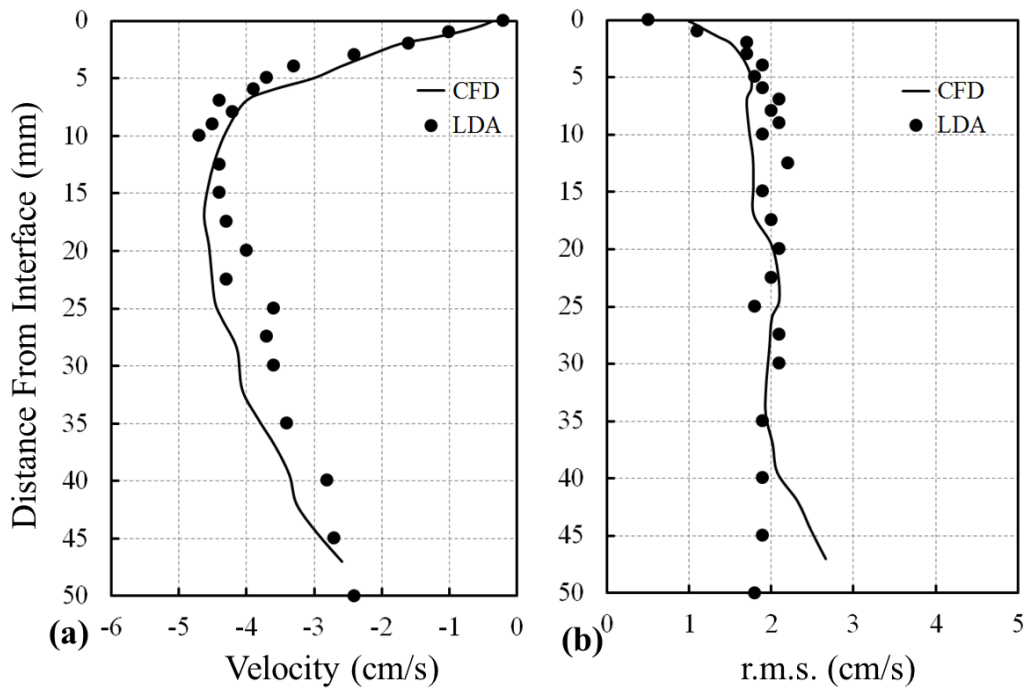


Figure 5.20 - Velocity field of the WOI experiment vs CFD at 7.0 cm from the SEN. (a) shows the streamwise component and its rms values are displayed in (b).

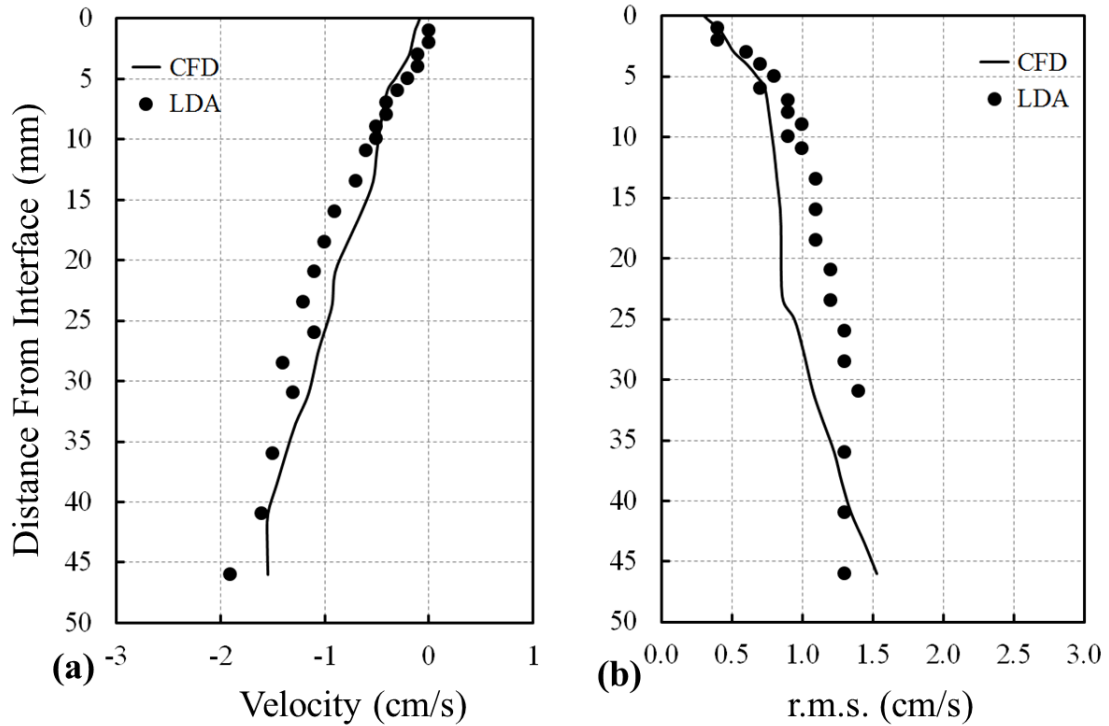


Figure 5.21 - Velocity field of the WOI experiment vs CFD at 3.5 cm from the SEN. (a) shows the vertical component and its rms values are displayed in (b).

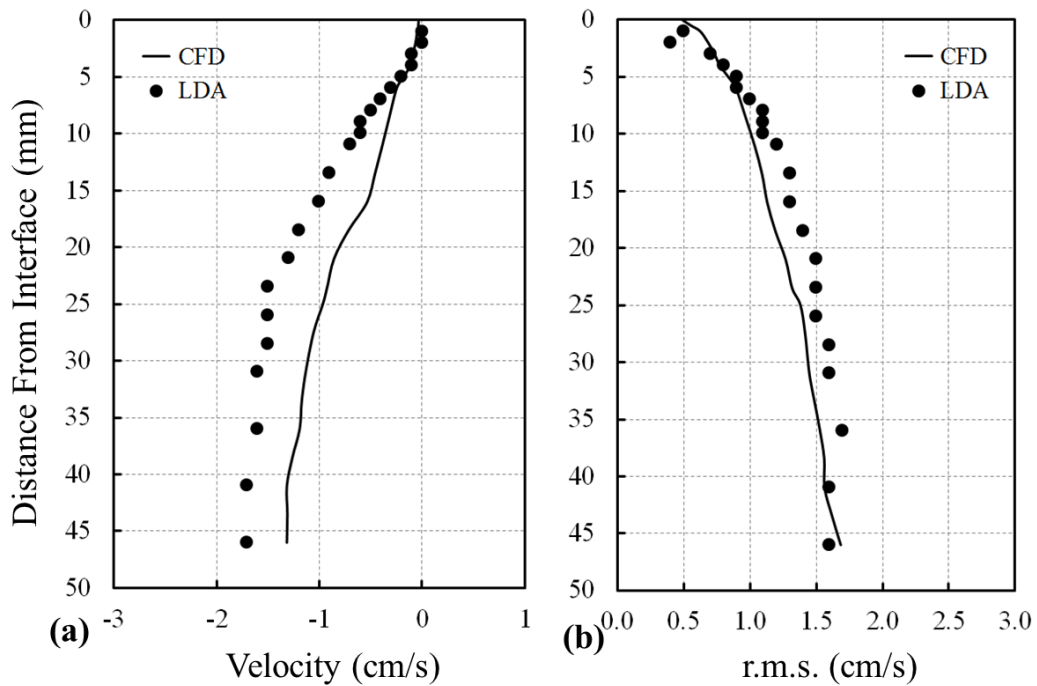


Figure 5.22 - Velocity field of the WOI experiment vs CFD at 7.0 cm from the SEN. (a) shows the vertical component and its rms values are displayed in (b).

In this case, the lighter phase behaves as a movable wall due to its high viscosity. A boundary layer is formed all beneath the interface, where the velocity decreases to reach very low

values at the water/oil interface. Although the mean values are low, the oil layer presents an oscillatory movement, and, differently from wall bounded flows, the rms does not reach zero value at this interface. This observation suggests that most of the turbulence, but not all of it, is damped beneath the interface and a minimum amount is transferred to the oil layer. Further analysis of the turbulent field will be provided in this chapter.

According to the wall boundary theories, the viscous boundary layer thickness is determined as the layer where the normalized velocity is equal the normalized distance from the interface ($u^+ = y^+$). The velocity is normalized by the friction velocity, $u^* = \sqrt{\tau/\rho}$ where τ is the shear stress given by the Newton's law of viscosity, which states that $\tau = \mu \partial u/\partial y$, where μ is the molecular viscosity. The normalized distance from the interface is given by $y^+ = y u^*/\nu$. The normalized velocity profiles for the positions studied are plotted in Figure 5.23.

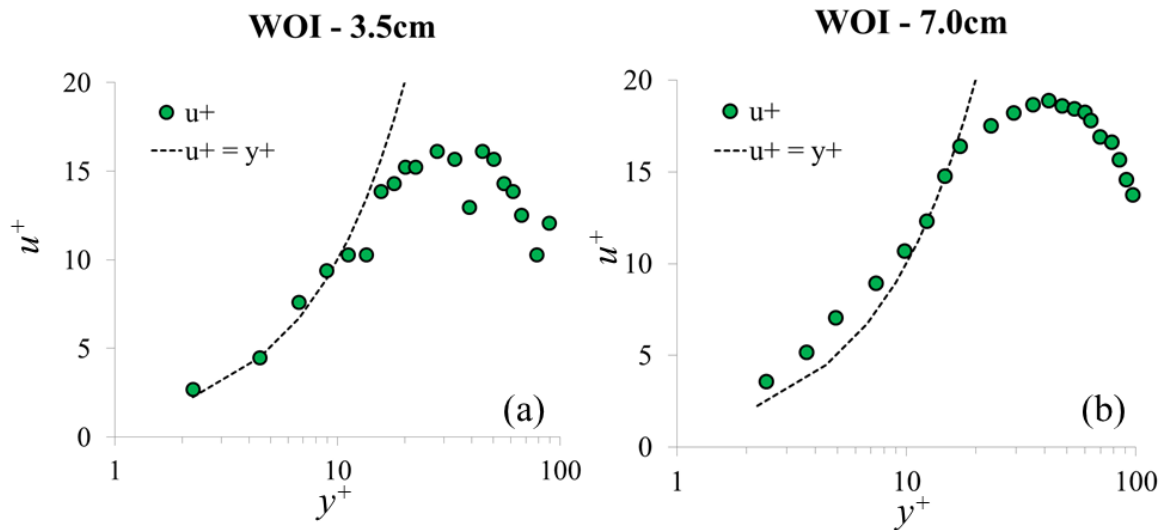


Figure 5.23 - Normalized velocity profiles.

We can see that in both positions the boundary layer thickness is about $y^+ \approx 10$. Table 5.3 shows these normalized and absolute thicknesses in those positions.

Table 5.3 - Boundary layer thicknesses and the related physical values.

	u^* (m/s)	y^+	δ_* ($\times 10^{-3}$ m)
3.5 cm	0.0023	13.4	6.9
7.0 cm	0.0027	11.2	5.5

The boundary layer is thicker than that found in wall bounded flows, where the viscous boundary layer thickness is 5 wall units. In practice, this information suggests that the mesh required to accurately compute the velocities close to a liquid/liquid interface is more affordable than that required to calculate the flow close to a wall.

5.4.2 Water Air (WFS) Configuration

As we have done for the WOI configuration, the velocity fields from calculation and experiment of the WFS configuration were compared. We also found good agreement between experiment and calculation:

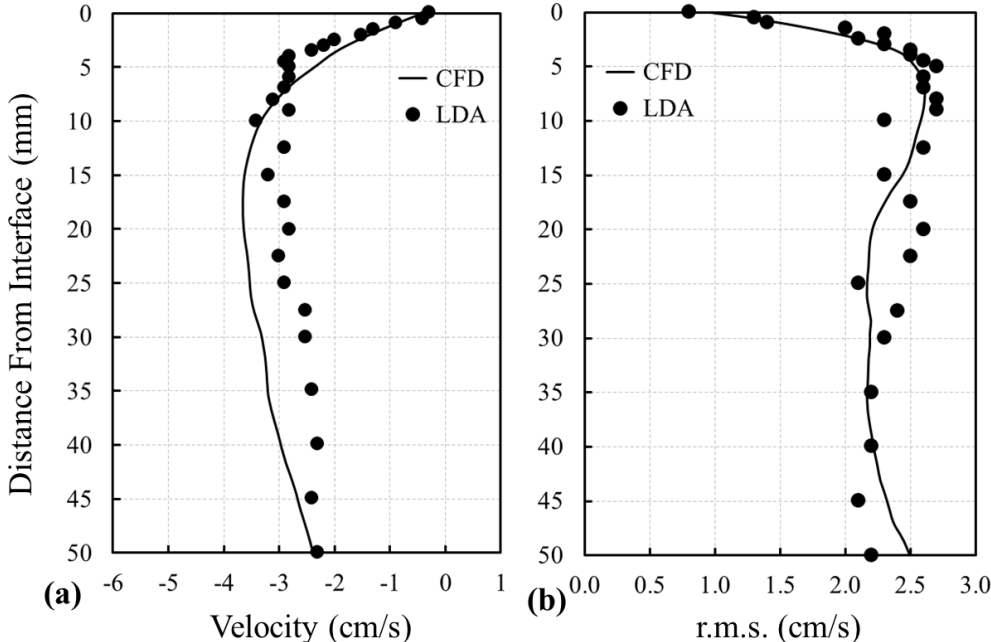


Figure 5.24 - Velocity field of the WFS configuration at 3.5 cm from the SEN. (a) shows the comparison between the CFD and the LDA values of the streamwise component (b) the comparison of the rms values.

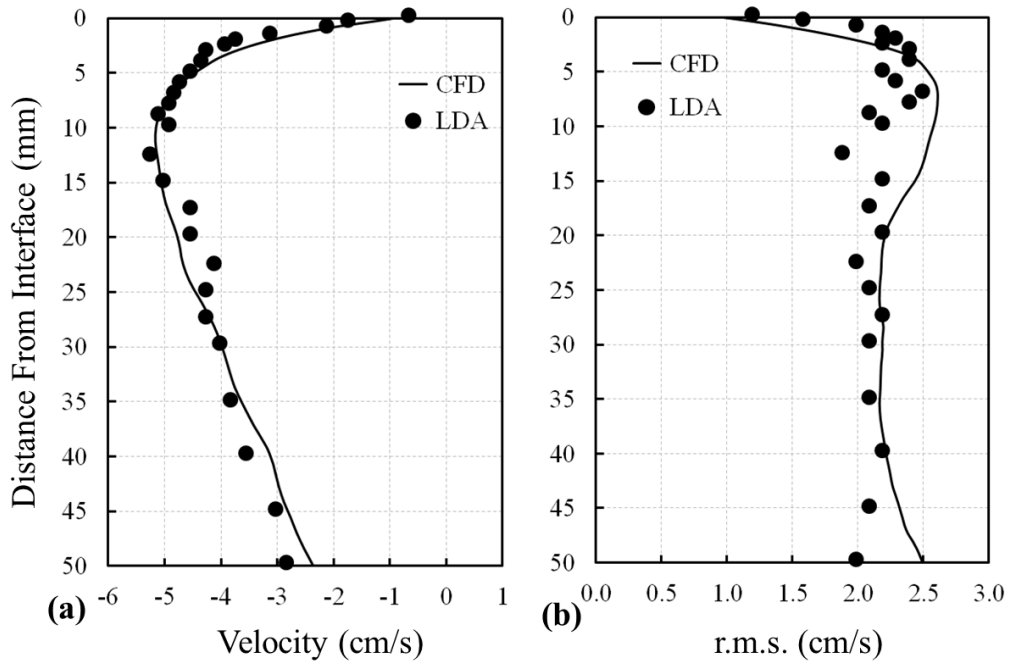


Figure 5.25 - Velocity field of the WFS configuration at 7 cm from the SEN. (a) shows the comparison between the CFD and the LDA values of the streamwise component (b) the comparison of the rms values.

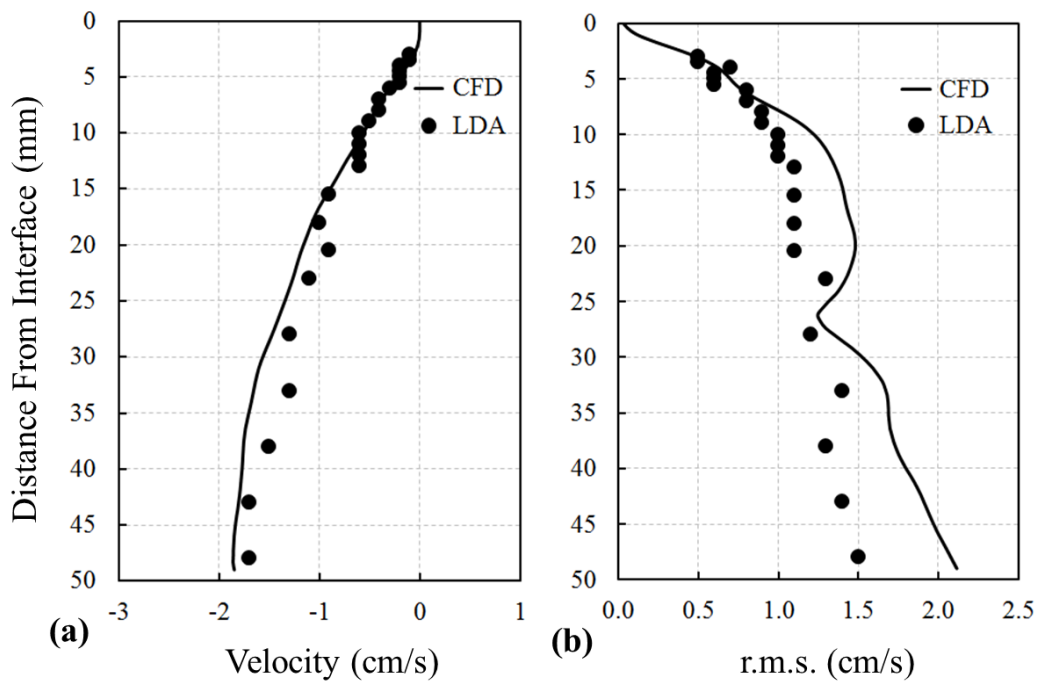


Figure 5.26 - Velocity field of the WFS configuration at 3.5 cm from the SEN. (a) shows the comparison between the CFD and the LDA values of the vertical component (b) the comparison of the rms values.

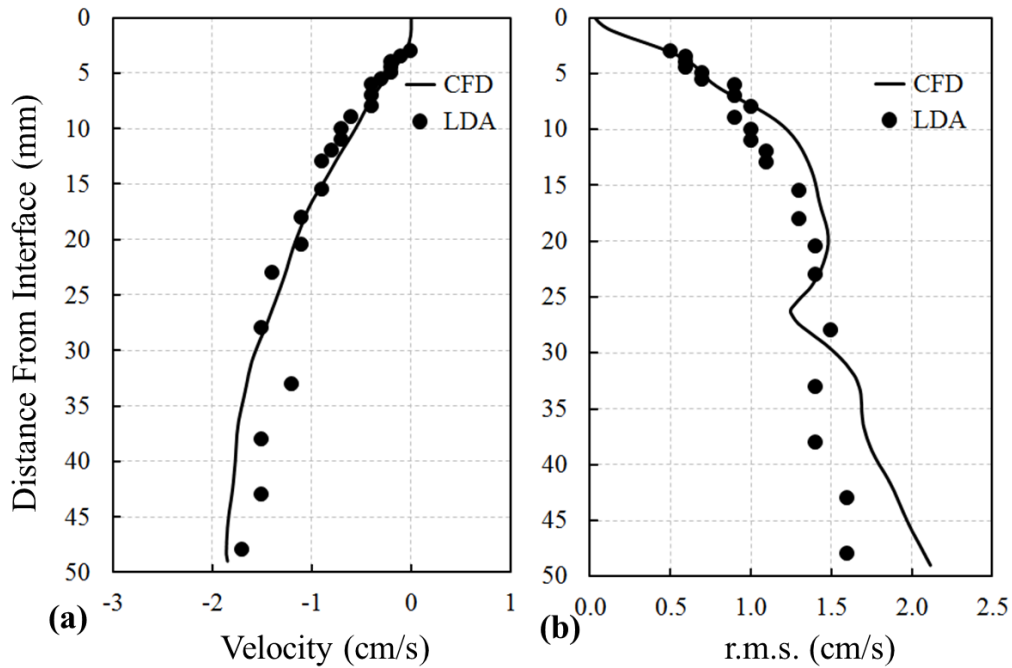


Figure 5.27 - Velocity field of the WFS configuration at 7 cm from the SEN. (a) shows the comparison between the CFD and the LDA values of the vertical component (b) the comparison of the rms values.

We observe here that the velocity profile is similar to that observed in the WOI even if no viscous phase is surrounding the water interface. This is an effect due to the averaging of the velocity field. The instantaneous velocity profiles do not constantly show such low velocities at the interface. In reality, many vortexes are seen reaching the interface in a very complex three-dimensional flow. At the detachment point of these vortexes the velocities are indeed very low, and the time and space average of this velocity field produces an average flow which looks like a boundary layer. The schematic view of these flows is shown in Figure 5.28.

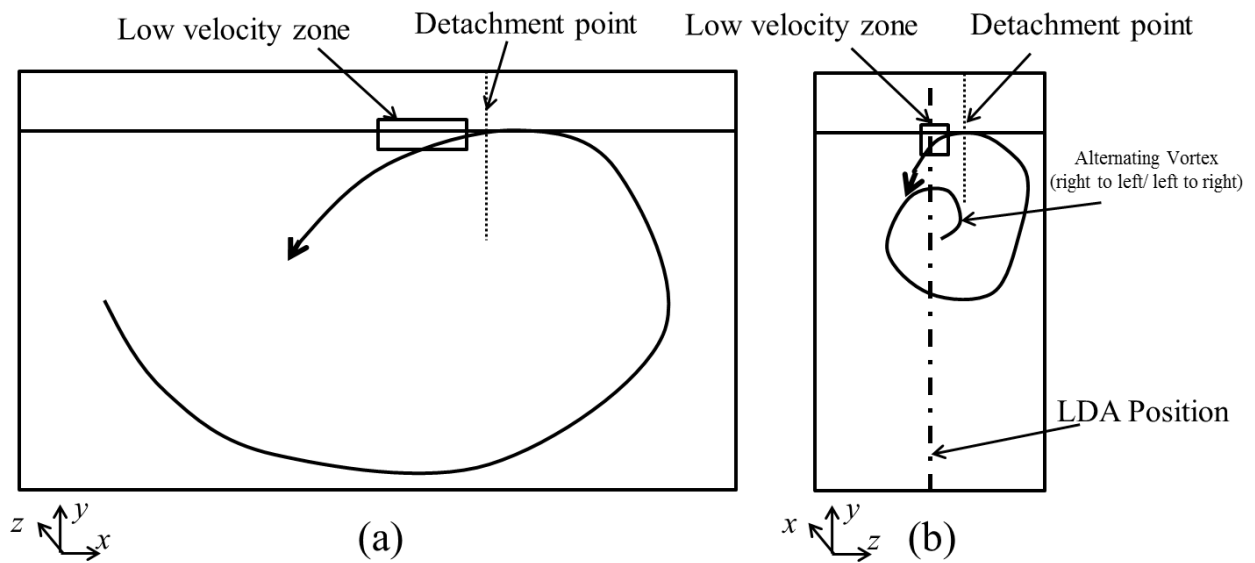


Figure 5.28 – Scheme of the instantaneous flow and the origins of the low velocities at the interface of the WFS configuration. (a) the front view and (b) the perpendicular view.

We can use the CFD model of this configuration to visualize the vector field and evaluate this conclusion. The vector field is shown in Figure 5.29 where one can see the vectors reaching the interface with non-zero values.

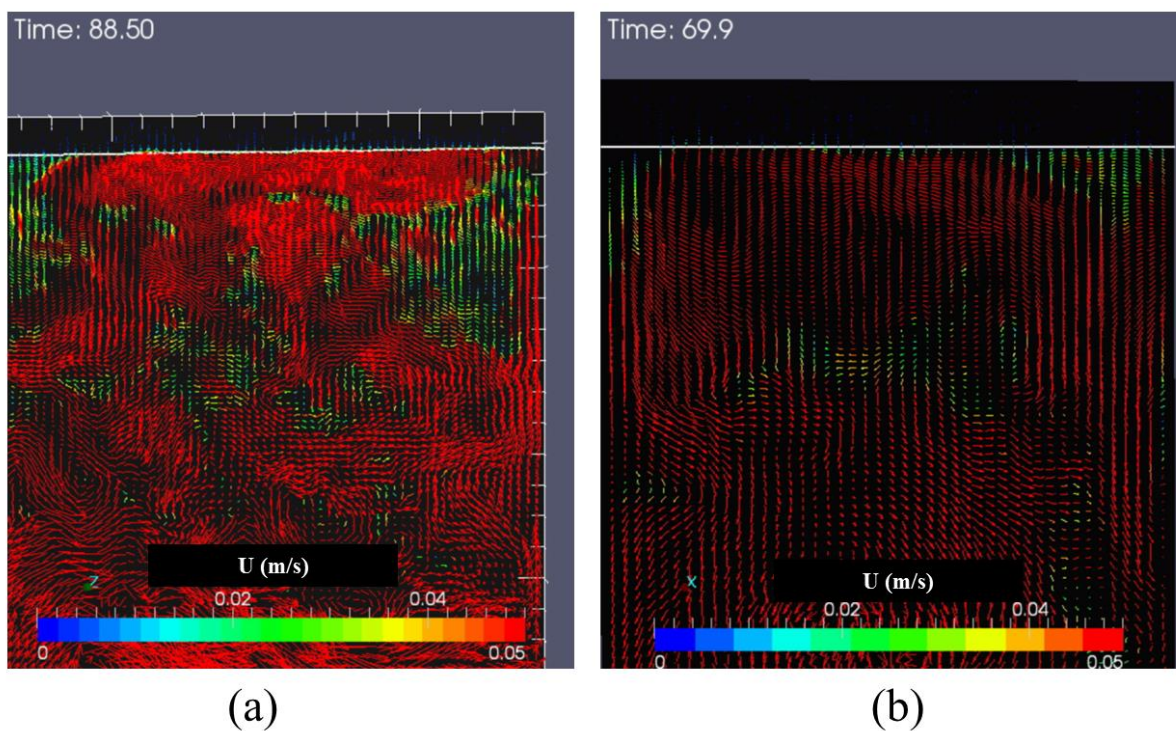


Figure 5.29 – Instant vector field of the WFS simulation. The front view is shown in (a) and a perpendicular view is shown in (b). The non-zero values of the velocity field are identified by the vectors in red touching the water/air interface.

We may compare these instantaneous velocity fields with the averaged ones. Figure 5.30 shows the averaged velocity field in the symmetry plane and in a perpendicular plane. By comparing these pictures, the averaging affects are readily seen.

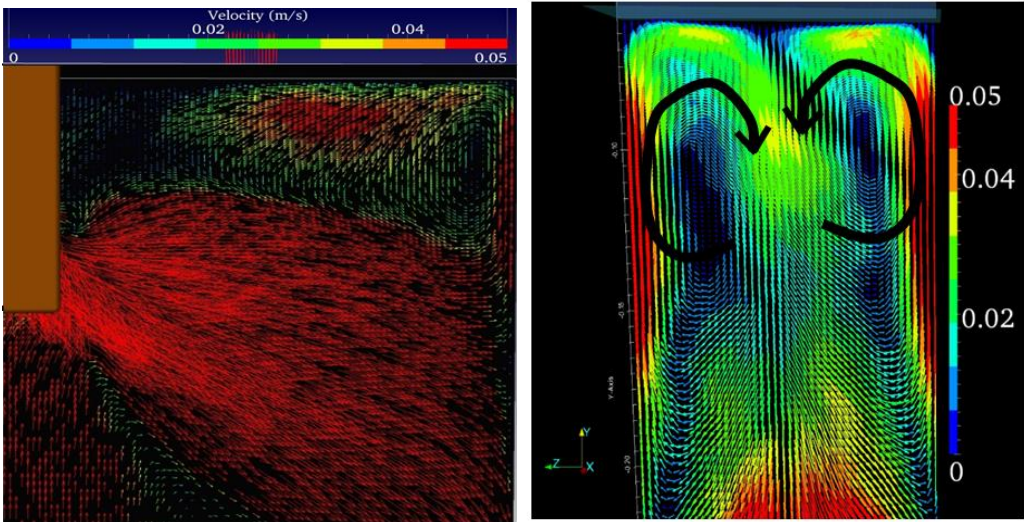


Figure 5.30 – Averaged velocity profiles of the WFS configuration

With the average effect in mind, we carry on the analysis of the flows as done before for the WOI configuration. The normalized velocity profiles of the average velocity field of the WFS configuration for the positions studied are plotted in Figure 5.31.

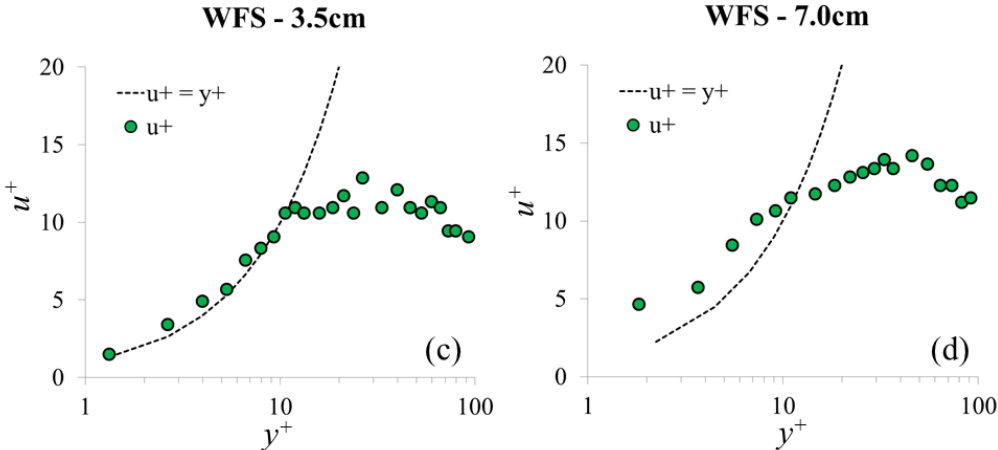


Figure 5.31 - Normalized velocity profiles.

One can see that in both cases the boundary layer thickness is about $y^+ \approx 10$. Table 5.4 shows these normalized and absolute thicknesses in different positions. In this simulation, the perpendicular mesh size at the interface in both sides is 0.5 mm, which is appropriate to compute the flow in the region of interest, with at least 5 mesh elements in the viscous boundary layer.

Table 5.4 - Average layer thicknesses.

	y^+	δ_* ($\times 10^{-3}$ m)
3.5 cm	10.6	3.5
7.0 cm	11	2.5

5.5 Turbulence Characterization

With the good agreement found between CFD results and experiments we are going to use the mathematical simulation to explore the turbulence of the system.

The very low velocities found at the interface with high rms values are a result of the characteristic oscillations in these CC configurations. The low frequencies of these periodical oscillations are generated from the oscillations of the two SEN jets [93] and add a third component to the velocity field. Consequently, the measured velocities, $u(t)$, can be decomposed as

$$u(t) = \bar{u} + [u' + \tilde{u}] \quad 5.2$$

where \bar{u} is the time averaged velocity and the term in brackets is the measured rms velocity, composed by u' , the fluctuating velocity due to turbulence, and by \tilde{u} , the low frequency induced component. The low frequencies responsible for these oscillations can be determined by a spectral analysis and suppressed from the rms values to investigate the turbulent fluctuations only. Figure 5.32 shows the spectra of the velocity measured with the LDA in one of the points beneath the interface (a), the water/oil interface oscillation measured in the experiments (b) and the water/oil interface oscillation in the CFD simulation (c).

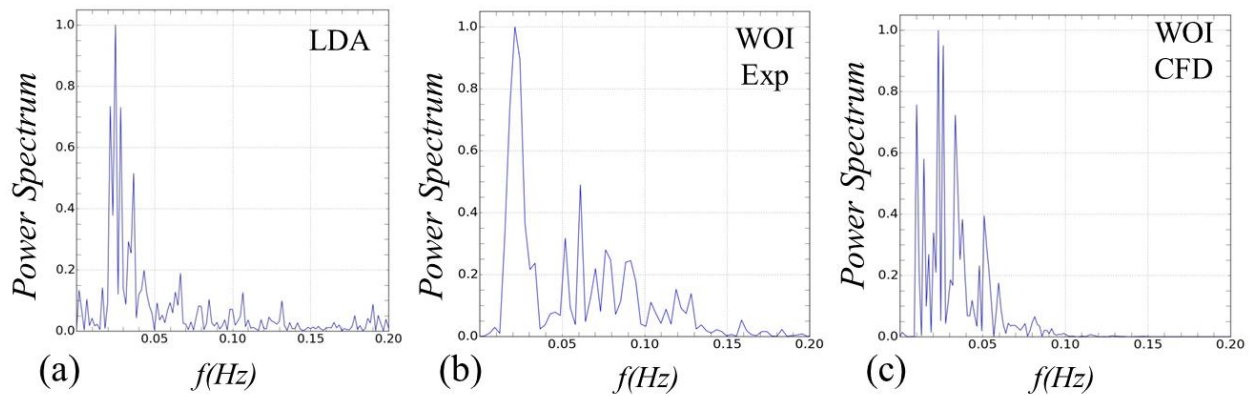


Figure 5.32 - Spectral signal of the LDA in (a), the experimental interface displacement in (b) and the CFD interface displacement in (c).

These low frequencies are the same as the ones from the interface oscillation, presented in the previous chapter. The dominant frequency is about 0.025 Hz. Gardin *et al* [93] attributed these dominant frequencies to the alternating periodical oscillations of the two SEN jets. Once these jets impinge the interface they generate waves with the same frequencies. By comparing the characteristic frequencies found in the wave characterization we can verify that both, wave interface and velocity frequencies, are closely related.

Knowing the low frequencies that characterize the SEN jet flapping, we can suppress the low frequency oscillations and reconstruct the signal. The superposition of all spectral signals (Figure 5.33) suggests that we can eliminate most of the low frequencies of the system by filtering the frequencies lower than 0.2 Hz.

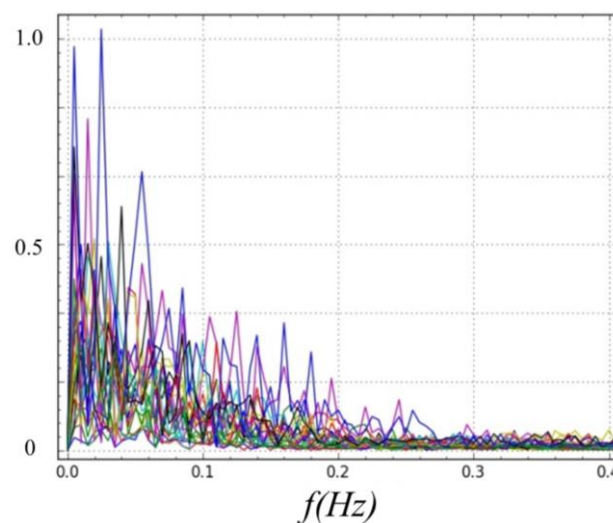


Figure 5.33 - Superposition of the normalized spectrum signal of the velocity measured at each point of a velocity profile.

To proceed with the filtering, the brut signal from the LDA is resampled to ensure equally spaced data. Then the LDA and CFD signal are smoothed with a moving average to eliminate the signal noise and, then, the low frequencies are filtered. In Figure 5.34 (a), the filtered signal is shown in green whilst the reconstruction of the low frequencies is shown in red. Hence, by adding both, the filtered signal and the low frequency signal, we have the brut signal in blue. This procedure is applied at each point and then we calculate again the mean and rms values. Since the majority of the low frequencies are under the value of 0.2 Hz we did not take the risk of destroying the quality of the signal by filtering frequencies higher than that. As an example, one may refer to Figure 5.34 (b), to see the effect of applying different filters on the rms signal.

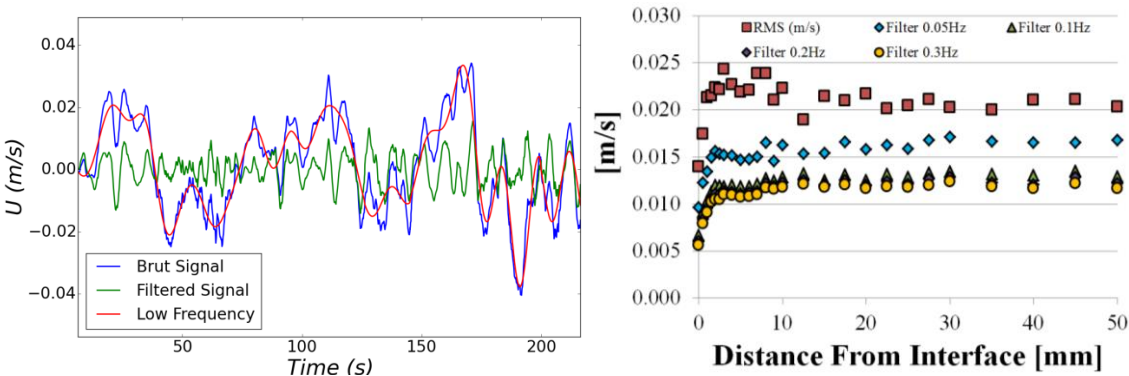


Figure 5.34 - Brut signal and its different components in (a) and the different filters applied to the RMS profile of the horizontal component of the WFS configuration at 7cm from the SEN.

The new profile after filtering the points of the WOI configuration at 7 cm is shown in Figure 5.35.

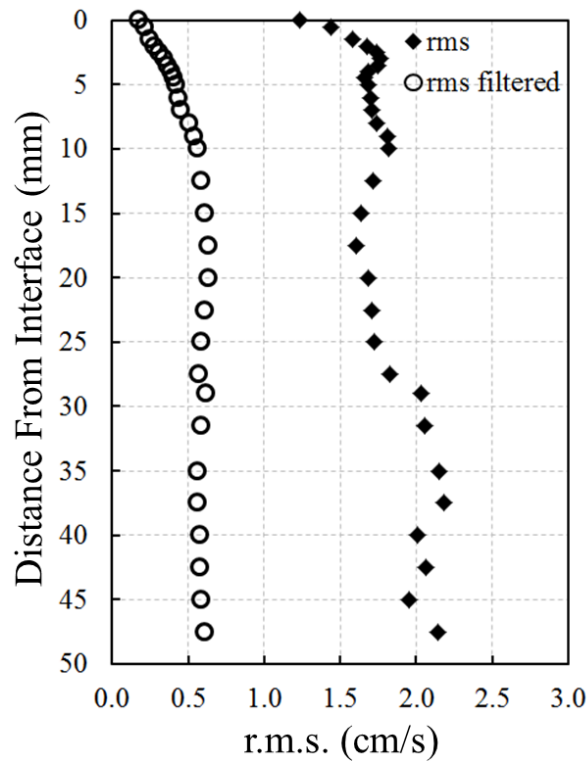


Figure 5.35 – rms profile after filtering the low frequency fluctuation values.

The comparison highlights the influence of the low frequency oscillations on the velocity fluctuation field. It was observed that the velocity fluctuations decrease near the liquid/liquid interface (Figure 5.35). The region where there is this damping in the velocity fluctuations matches with the viscous boundary layer described before. With the filtered field, the turbulence was separated from the influences of the low frequency oscillations of the CC system and we could proceed with the analysis of the turbulence field and its implications on mass transfer.

We used the filtered fields of the CFD results, which provide us the third velocity component that was not measured with the LDA, to evaluate some aspects of the turbulence near the interface of a CC mold. Figure 5.36 (a) to (d) show the turbulence intensities, here represented by the rms velocities, normalized by their respective shear velocity.

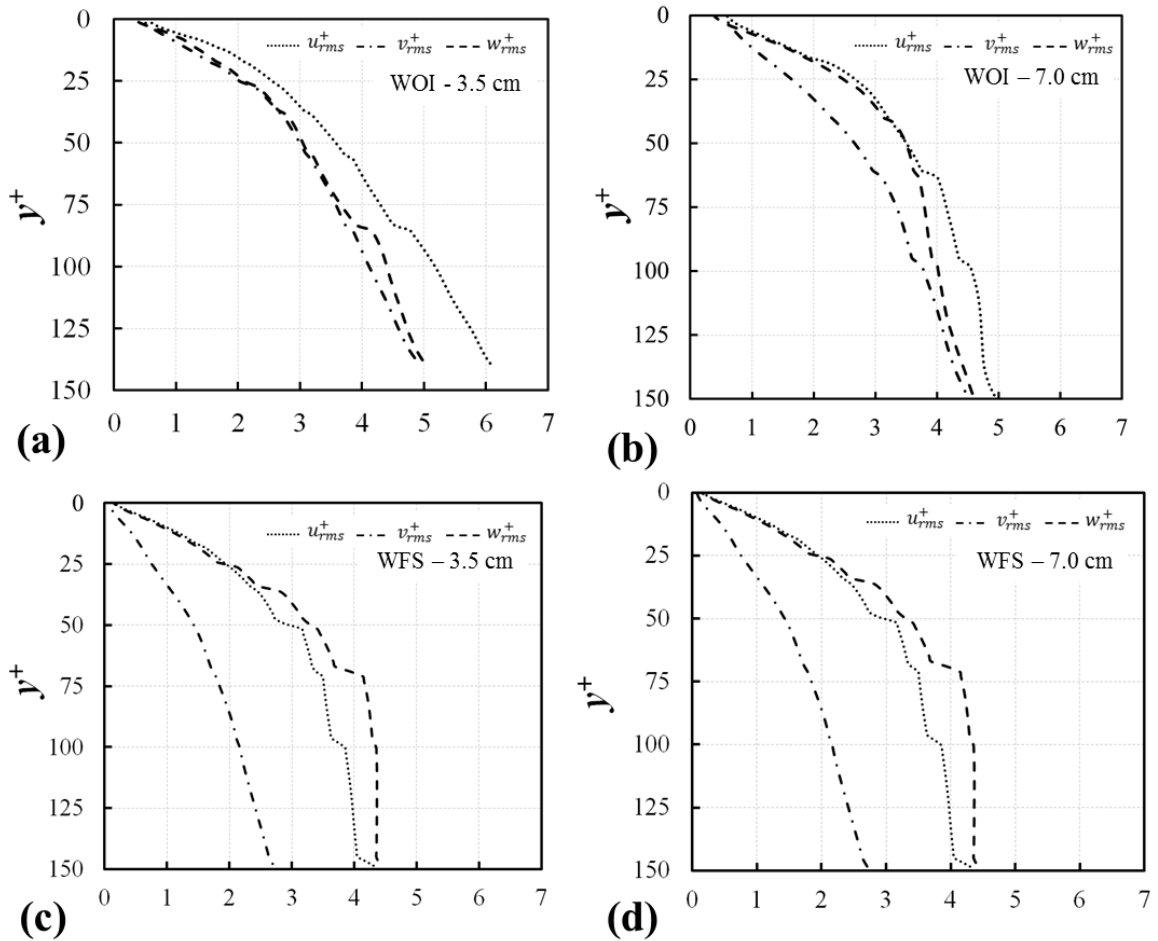


Figure 5.36 – Normalized rms velocities of WOI (a and b) and WFS (c and d) in the liquid-side.

We see a decrease of the turbulence intensities of the three velocity components near the interfaces. But one should note the difference in the values of the turbulent velocity fluctuations close to the interface position. For the WFS the turbulence is almost completely damped at the viscous boundary layer, whilst a little more turbulence remains in the liquid/liquid interface. The remained turbulence in WOI configuration is probably absorbed by the upper phase and dissipated by the oil layer (Figure 5.37 (a) and (b)).

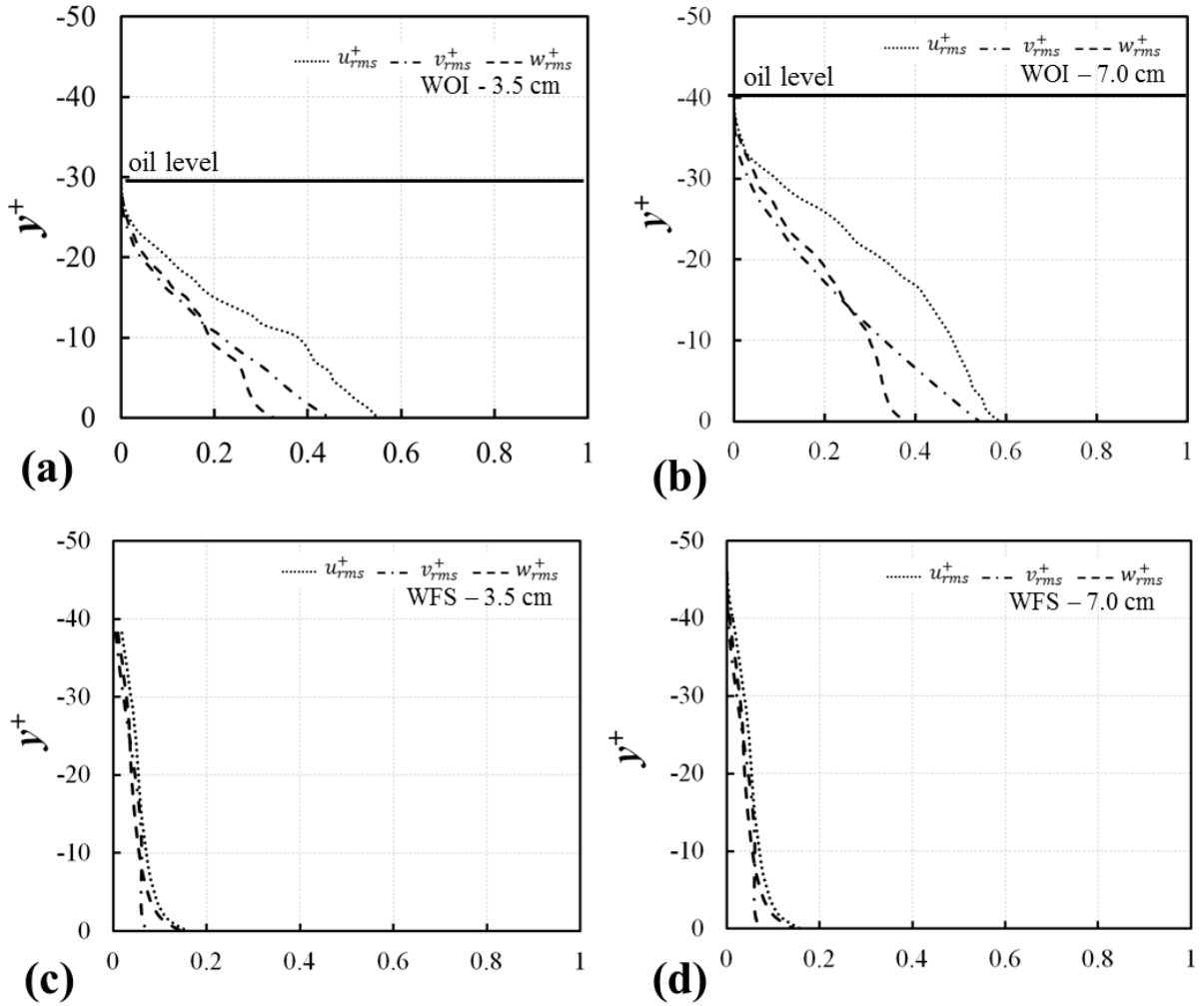


Figure 5.37 - Normalized turbulence intensities of WOI (a and b) and WFS (c and d) in the upper phase-side.

We also evaluated the total kinetic energy, \bar{K} , and the turbulent dissipation, ε , given by

$$\bar{K} = \frac{1}{2} (\overline{u'^2} + \overline{v'^2} + \overline{w'^2}) \quad 5.3$$

$$\varepsilon = \nu \overline{\omega_i'^2} = \nu (\overline{\omega_1'^2} + \overline{\omega_2'^2} + \overline{\omega_3'^2}) \quad 5.4$$

respectively. Here $\overline{\omega_i'^2}$, is the mean square of the vorticity fluctuations.

The kinetic energy is dissipated in the viscous boundary layer of both configurations, as shown in Figure 5.38.

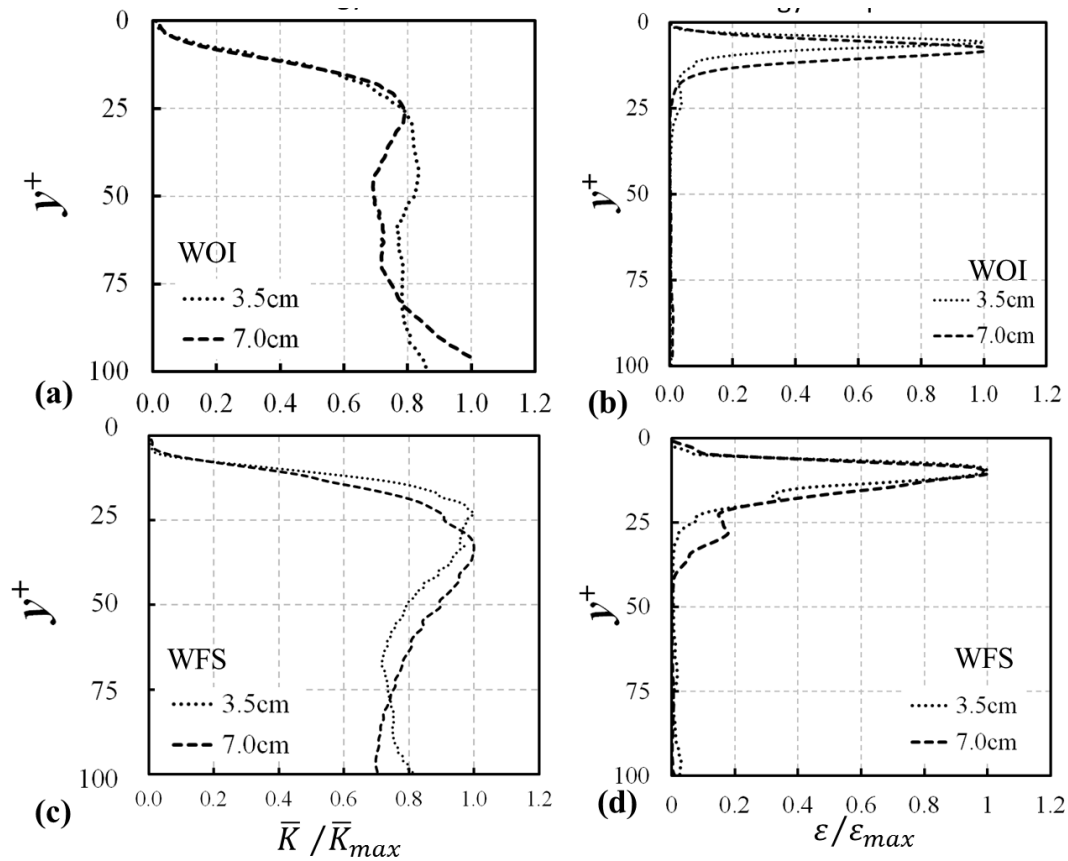


Figure 5.38 – Evolution of the Kinetic energy (a) and (c) and the energy dissipation (b) and (d) close to the WOI and WFS.

Even though the pictures look similar, the maximum values used for normalization in each configuration are fairly different. Table 5.5 shows the referred values. It can be seen that, for the WOI configuration, much more kinetic energy remains at the interface and much less dissipation occurs at this position. In the WFS configuration, the environment is quite different, with less kinetic energy and more dissipation. This observation is in accordance with Figure 5.37, which shows that some turbulence is transferred to the oil layer in the WOI configuration, while only a negligible value is transferred to the air layer in the WFS configuration.

Table 5.5 – Maximum values used for normalization of the kinetic energy dissipation, ε , and the kinetic energy, K .

	WFS		WOI	
	3.5 cm	7.0 cm	3.5 cm	7.0 cm
$\varepsilon_{max} [\times 10^{-5} m^2/s^3]$	8.3	47	5.8	12.2
$K_{max} [\times 10^{-4} m^2/s^2]$	5.5	7.6	16	13

5.6 Turbulence implications on Mass Transfer Coefficients

The mass transfer models presented in Chapter 2 depend on hydrodynamic characteristics which are intimately linked with the turbulence field. We may use the CFD calculations to examine the parameters needed in those models before calculating the mass transfer itself. One of the main contributions of the present work is the evaluation of the applicability of those mass transfer models in a liquid/liquid framework. Thus, we are going to investigate the parameters with the WOI configuration.

We start by considering that inside the viscous boundary layer the turbulence is statistically in equilibrium and uniquely determined by the parameters ε and ν . This state of equilibrium emphasizes that the character of the turbulence in this region does not depend on any specific mechanism of the mean flow. The only parameters that play any role in the description of the turbulence are the viscosity and the dissipation. With these considerations, we defined the Kolmogorov length scale, which is the smallest scale of the dissipative structures, using dimensional analysis as

$$\eta = \left(\frac{\nu^3}{\varepsilon} \right)^{1/4} \quad 5.5$$

And the velocity scale is

$$u_\eta = (\nu\varepsilon)^{1/4} \quad 5.6$$

In the same manner, we can estimate the Kolmogorov time scale, τ_η , as

$$\tau_\eta = (\nu/\varepsilon)^{1/2} \quad 5.7$$

We have the relation between the diffusive boundary layer thickness, δ_c , to the viscous boundary layer, δ_u , demonstrated by Calmet and Magnaudet [25] as

$$\delta_c \propto \sqrt{\delta_u} Sc^{-1/2} \quad 5.8$$

This shows that, for high Sc numbers the concentration boundary layer is much thinner than the velocity boundary layer. Hence, from the definition of integral time scales, which is the time needed to the turbulent signals to decorrelate, it is possible to infer that this time will also be the time needed to the fluid packets near the interface to be completely replaced by new fresh fluid packets. In this sense, the integral time scale can be tough as the renewal time. Therefore, τ_η is the renewal time due to the small eddies. This time scale can be used to

estimate the mass transfer coefficients with the renewal theory, based on the Small Eddy Model (SEM).

The renewal time derived from the large eddies is obtained by the integral time scale relation

$$T = \bar{K}/\varepsilon \quad 5.9$$

and is analogous to a renewal time based on the large eddies and we can use it in the Large Eddy Model (LEM) described in Chapter 2.

To define a Reynolds number we need a length scale which characterizes the size of the large structures containing the kinetic energy. In CC configurations, it is customary used the thickness of the CC mold as the characteristic length scale of the system. Based on this quantities, we define our turbulent Reynolds number as

$$Re_t = \frac{u^*L}{\nu} \quad 5.10$$

which can be applied on normalized versions of the mass transfer models.

The quantities related to the turbulence field to be used on the mass transfer models are potted in Table 5.6 below.

Table 5.6 – Kolmogorov and Integral Scales at the liquid/liquid interface.

	\bar{K}_t ($\times 10^{-4} \text{ m}^2/\text{s}^2$)	ε_t ($\times 10^{-5} \text{ m}^2/\text{s}^3$)	η ($\times 10^{-4} \text{ m}$)	u_η ($\times 10^{-3} \text{ m/s}$)	τ_η (s)	L (m)	u_L ($\times 10^{-3} \text{ m/s}$)	T (s)	Re_t	u^* ($\times 10^{-3} \text{ m/s}$)
3.5 cm	2.8	3.6	4.1	2.4	0.2	0.1	13	8	1,286	2.3
7.0 cm	2.7	2.1	4.7	2.1	0.2	0.1	8	13	778	2.7

Applying these values on the mass transfer models presented in Chapter 2, for a species diffusivity of $D = 1 \times 10^{-10} \text{ m}^2/\text{s}$ ($Sc_{water} = 1 \times 10^4$), which is the range found in steelmaking industry, we obtain the values summarized in Table 5.7. These values are in agreement with the values commonly used in steelmaking modeling [94] (we can compare them because of the similarity of the Sc number and the kinematic viscosity of liquid steel and water).

Table 5.7 - Mass Transfer Calculations.

Mass Transfer Model	Equation	3.5 cm	7.0 cm
LEM	$\bar{k} = \sqrt{D/T}$	$\bar{k} = 3.5 \times 10^{-6}$	$\bar{k} = 2.8 \times 10^{-6}$
Normalized LEM	$\bar{k} = 1.07 u_L Sc^{-1/2} Re_t^{-1/2}$	$\bar{k} = 3.9 \times 10^{-6}$	$\bar{k} = 3.1 \times 10^{-6}$
Simplified LEM	$\bar{k} = 0.108 u^*$	$\bar{k} = 2.5 \times 10^{-4}$	$\bar{k} = 2.9 \times 10^{-4}$
SEM	$\bar{k} = \sqrt{D/\tau_\eta}$	$\bar{k} = 2.2 \times 10^{-5}$	$\bar{k} = 2.2 \times 10^{-5}$
Normalized SEM	$\bar{k} = 0.25 u_L Sc^{-1/2} Re_t^{-1/4}$	$\bar{k} = 5.4 \times 10^{-6}$	$\bar{k} = 3.8 \times 10^{-6}$
SDB	$\bar{k} = 0.30 u_L Sc^{-1/2} Re_t^{-1/2} [0.3(2.83 Re_t^{3/4} - 2.14 Re_t^{2/3})]^{1/4}$	$\bar{k} = 3.5 \times 10^{-6}$	$\bar{k} = 2.5 \times 10^{-6}$

In these results we see that there is not a big difference between the values found with the LEM and the normalized form of it. However, its simplified form provided us a very different value, much higher than the ones found in the complete version of the LEM. The values from the SEM are more sensitive to the normalization and the calculations showed very different values depending upon the parameters used. The mass transfer values found by applying the SDM match very well the ones of the LEM in both dimensional and normalized form.

5.7 Mass Transfer distribution at the liquid/liquid interface

With the values in Table 5.7 we identified the heterogeneous distribution of the mass transfer coefficients by observing divergent values when comparing the coefficients at the two positions where the velocity field was measured. Therefore, it should be important for steelmakers to know where the liquid slag composition will be more affected in order to predict and prevent eventual interferences on the process by, for example, rapid changes in the slag viscosity and loss of its lubricant properties.

In order to visualize the mass transfer coefficients distributions in the whole liquid/liquid interface, we applied the simplified form of the LEM, as proposed by Banerjee *et al* [95] where

$$k = 0.1 u^* Sc^{-1/2} \tag{5.11}$$

and the dimensional form of the SDM as stated in Eq. (2.17) and restated below

$$k = 0.71\sqrt{D\gamma'} \quad 5.12$$

The mass transfer coefficient was calculated in the whole interface of the CFD model based on for a Schmidt number of 1×10^4 . The values predicted remain in the range typically employed in steelmaking studies [94], as shown in Figure 5.39.

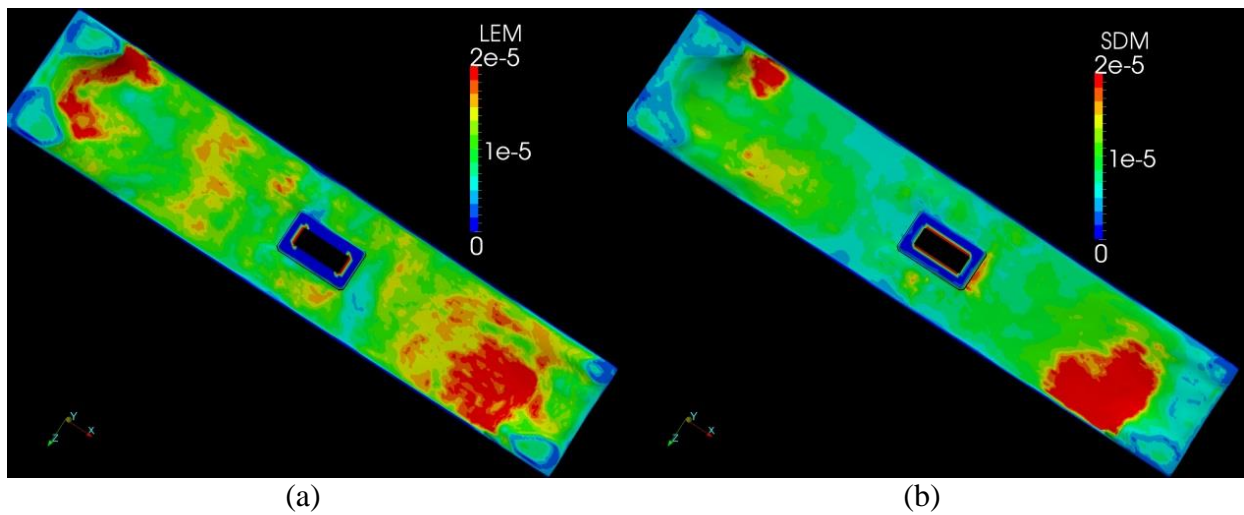


Figure 5.39 - Prediction of mass transfer coefficients, k [m/s], in a CC water model. Results in (a) are calculated by Large Eddy Model and in (b) by Surface Divergence Model.

One may note that the mass transfer coefficients are not homogeneously distributed at the interface, being much more intense in the regions close to the narrow faces, where the impinging jets reach the interface. It is expected that during the casting of steels with high alloy elements, such as manganese and aluminum, the liquid slag in those regions may suffer the greatest changes in chemical composition and physical properties. At most casters, the starting mold slag viscosity might be adjusted to account for the predicted changes in chemical composition in such a way that these oxides generation can be controlled.

These chemical changes expected to happen during the casting have, in the past, been characterized by sampling the mold slags during trials of different mold fluxes. This trial and error procedure is associated with risks of break-outs and degradation in product quality [94]. If the liquid steel/slag mass transfer rates are accurately predicted, considerable gains can be made in terms of casting new grades and designing new mold fluxes. The prediction of the mass transfer coefficients achieved in this work may be of good usage to steelmakers to optimize continuous casting of steels.

5.8 Influence of process parameters on mass transfer coefficients

The preliminary tests in water models showed the possible influence of many industrial parameters based on a single point where the velocity field was measured. In order to examine those conclusions we used the CFD model to investigate the influence of the casting speed and liquid slag layer viscosity on the mass transfer coefficient at the liquid/liquid interface.

As mentioned in Chapter 2, the application of the SDM in cases where the interface is perturbed and droplets are formed inserts uncertainty when performing the divergence statistics. Since we are concerned about developing mass transfer models to predict mass transfer rates in industrial process, we are not willing to afford such ambiguous definitions. Instead, we opted to adopt the simplified version of the LEM derived by Banerjee *et al* [95] in such studies.

Hence, the CFD model was used to evaluate the influences of the casting speed and upper phase viscosity on mass transfer rates based on Eq. (5.11). The results are presented in the following discussions.

5.8.1 Casting Speed

The casting speed is controlled by the mass flow of liquid steel during the casting. In the case of the physical model, this flow is represented by the water flow injected through the SEN. As mentioned before and summarized in Table 5.2, the reference casting speed is represented by the water flow rate of 1.6 m³/h. We evaluated the effect of increasing the water flow from 1.6 to 3.0 m³/h. Figure 5.40 shows the mass transfer coefficient distribution over the water/oil interface. We observe that, by increasing the water flow rate, the area with the more intense mass transfer rate increases. The maximum mass transfer coefficients are found in the regions where the SEN jets impinge the interfaces. This jet impinging is capable of uncovering the water surface, exposing the heavier liquid to the atmosphere. This uncovering is seen by the black regions near the narrow faces of the CC mold.

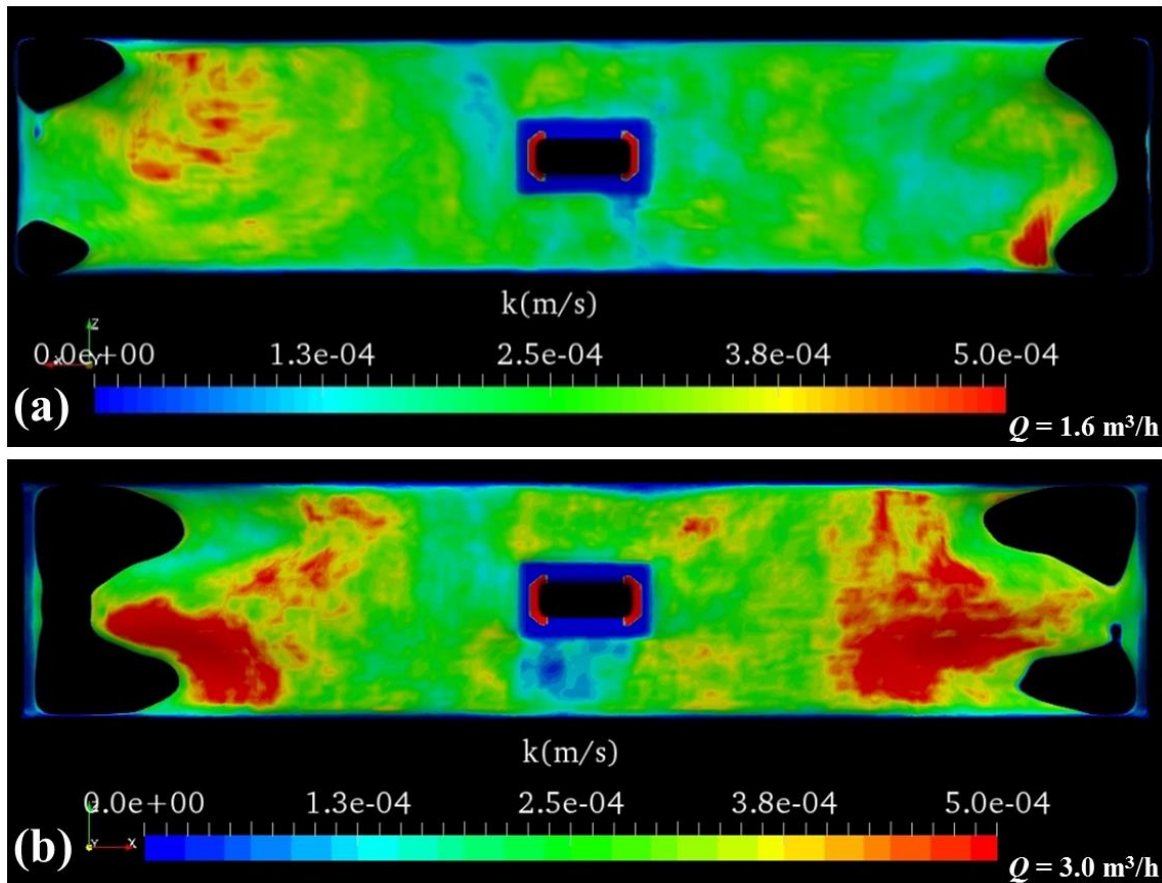


Figure 5.40 – CFD mass transfer coefficient at the WOI for a water flow of $1.6 \text{ m}^3/\text{h}$ (a) and $3.0 \text{ m}^3/\text{h}$ (b). The images show the average values over 10 seconds.

By averaging the values of the mass transfer coefficients over the entire liquid/liquid surface, we quantified the mass transfer enhancement due to the water flow increase in about 30%. This augmentation will produce faster changes in slag composition and in its viscosity, having an influence on the flux lubricant properties. This trend confirms the conclusions from the preliminary water model trials, which suggested that an increase in the water flow rate would increase the shear stresses at the interface.

For practical applications, it suggests that, when trying to improve CC performance by increasing the casting speed, it is necessary to change the flux powder for the most suitable one in order to maintain the desired lubricant properties of the melted flux.

5.8.2 Slag viscosity

During the casting, the melted flux will react with the liquid steel and mass transfer will occur. The liquid slag will invariably change its composition and physical properties throughout the process. It is, then, of great interest to evaluate the slag composition evolution

during the CC operations in order to design the best flux powder capable of achieving and maintaining the appropriate viscosity to ensure the mold lubrication. To evaluate the influence of the changes in slag viscosity, we used the CFD model to simulate the case with the less viscous oil layer (oil 2 in Table 3.2), with kinetic viscosity of 20 cSt. The mass transfer coefficient distribution over the entire liquid/liquid interface is presented in Figure 5.41.

It is indicated that the overall mass transfer will be enhanced if the upper phase viscosity is increased. Our CFD studies were performed with a fixed Sc number ($Sc = 1 \times 10^3$), which means that the real effect of the viscosity, in these experiments, was in the friction velocity, u^* . This is stated here because in a real situation, the transfer of species from the liquid steel to the slag will change the viscosity of the fluids near the interface and, consequently, it will change the Sc number.

By averaging the values of the entire interface, we could quantify the increasing of the mass transfer rate with the increase of the upper phase viscosity. It was seen that, by increasing the viscosity from 20 to 350 cSt, the average mass transfer coefficient was increased by 150%. This trend confirmed the conclusions from the preliminary water model trials that showed that an increase in the upper phase viscosity will increase the shear stress at the interface. This quantification will be particularly interesting when designing flux powders for steel grades with high alloy elements, which may locally change the slag properties and the mass transfer rates. The initial powder composition should be designed as to attain its appropriate properties after melted and reacted with the liquid steel.

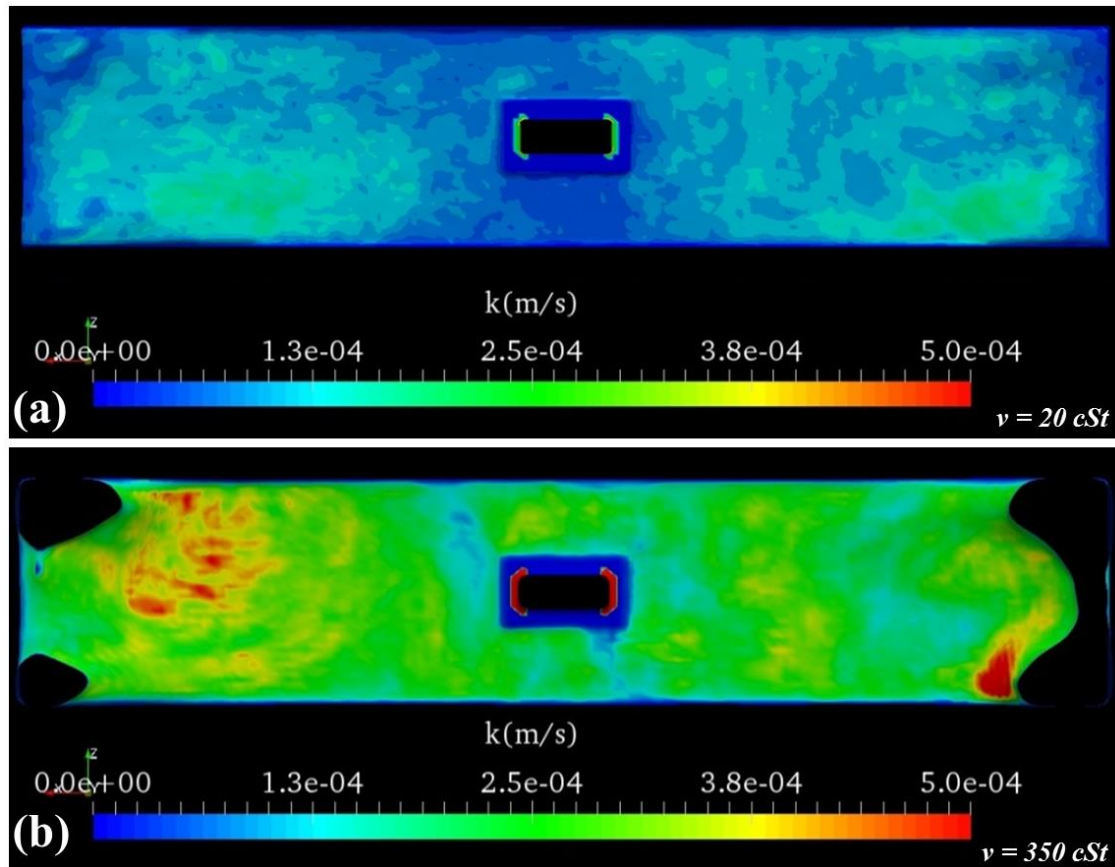


Figure 5.41 – CFD mass transfer coefficient at the WOI for an oil layer viscosity of 20 cSt (a) and 350 cSt (b). The images show the average values over 10 seconds.

Another possible applicability of this model would be to design different mold fluxes to be used according to the positions where it will be fed during the casting, allowing the optimization of the process.

5.9 Conclusions

In this chapter we presented the results from the experimental trials which identified the possible influence of some key parameters of CC flow on the interface region based on a single measured location. We saw that the water flow rate is the turbulence source of the system, that the upper phase viscosity would have some effects on the interface shear and that the thickness of the oil layer could locally change the flows and alter the recirculating flow close to the SEN. Based on these first trials we proposed a configuration to be used in the mathematical studies.

The CFD results of the proposed CC configuration agreed very well with the experimental data. It was validated for both mean and fluctuation velocity values of the vertical and horizontal components. We saw that the oil layer is regarded as a movable wall by the water phase, generating a viscous sub-layer all beneath the oil interface. This liquid/liquid boundary layer was found to be thicker than that of wall bounded flows. Moreover, differently from the wall bounded flows, the turbulence is not completely damped in the viscous boundary layer and some turbulence is transferred to the oil layer.

With the validated velocity field computed by our model, we analyzed the turbulence field in order to identify the parameters used in the mass transfer models. We could apply these models on the positions where the measures were taken and locally obtain the values of the mass transfer coefficients. We observed a difference between the values at the different positions. Therefore it might be expected to have a heterogeneous distribution of the mass transfer coefficients in the liquid/liquid interface. This heterogeneity was confirmed after applying the mass transfer models over the liquid/liquid interface. We could see higher values for the mass transfer rate in the regions close to the narrow faces, where the jets coming out from the SEN impinge the interface.

The effect of casting speed and upper phase viscosity on the mass transfer rate was investigated based on the CFD results. It was seen that the mean mass transfer coefficient is increased when the casting speed is increased. The same behavior was observed when increasing the upper phase viscosity.

The mass transfer models are ready to be used in CFD models to calculate the mass transfer coefficients. However, it is important to compare the results from these mathematical models to experimental liquid/liquid mass transfer to verify the coefficients of these models. This is the topic of the next section.

6 Liquid/Liquid Mass Transfer

Experiments

In the last chapter, we presented the hydrodynamics of the CC water model and we validated the CFD velocity field based on experimental measurements. The mass transfer coefficients were calculated over the entire interface based on the simplified form of the LEM and the SDM. However, these models were developed in a gas/liquid mass transfer framework, and were validated based on DNS [33] and LIF [96] measurements. The suitability of these models for liquid/liquid mass transfer calculations is still uncertain and experimental data are necessary to evaluate the accuracy of these models.

In this chapter, we are going to present some techniques used to characterize liquid/liquid mass transfer. This type of investigation has been of interest of metallurgical researches since long time ago, and is usually performed by curve fitting data from industrial or laboratory scale experiments.

6.1 Liquid/Liquid Experiments

In the metallurgical community, chemical reactions between two immiscible liquids (*e.g.*, slag and metal) in gas stirred systems are the subject of considerable interest and importance. Thus, innumerable experimental studies have been carried out and reported to investigate slag-metal-gas interactions in gas stirred ladle systems, expressing widely varying experimental conditions, such as vessel geometry, gas flow rate, gas injection devices, etc.

To validate the mass transfer models, we can rely on those ladle experiments where the liquid/liquid mass transfer was the main focus. In such experiments, water and organic fluids (oil, benzene, cyclohexane, etc.) were used to represent the metal and slag phases respectively. Usually, the rate of the liquid/liquid reaction is measured by monitoring the concentration of tracer which has an equilibrium partition ratio between water and the upper phase liquid. In these systems, it is extremely difficult to precisely define the interface area of the liquids, and it is usually used a volumetric mass transfer coefficient ($K_w A$; K_w = aqueous phase mass transfer coefficient) to quantify the experimental results.

Flow visualization studies on bubble stirred oil-water systems indicate that the oil-water interface can undergo high disturbance effects, hosting complex physical phenomena such as

oil droplet formation and oil entrainment. Thus, at low gas flow rates, the interface remain stable but with increasing flow rates, oil ligaments and droplets tend to form at the liquid/liquid interface, leading to a significant increase in the oil/water interface area for mass exchange [14] [97] [98]. At higher gas flow rates, the oil layer may break down into numerous droplets leading to the formation of an oil-water emulsion. Volumetric mass transfer coefficients experimentally measured are plotted as a function of the gas flow rate in Figure 6.1. There, corresponding to these three operating regimes, different functional relationships are seen to govern the mass transfer phenomenon. Also, the flow rates at the transition points in Figure 6.1 are a function of the volume as well as the thermophysical properties of the upper phase fluid and therefor, would vary from one physical system to another.

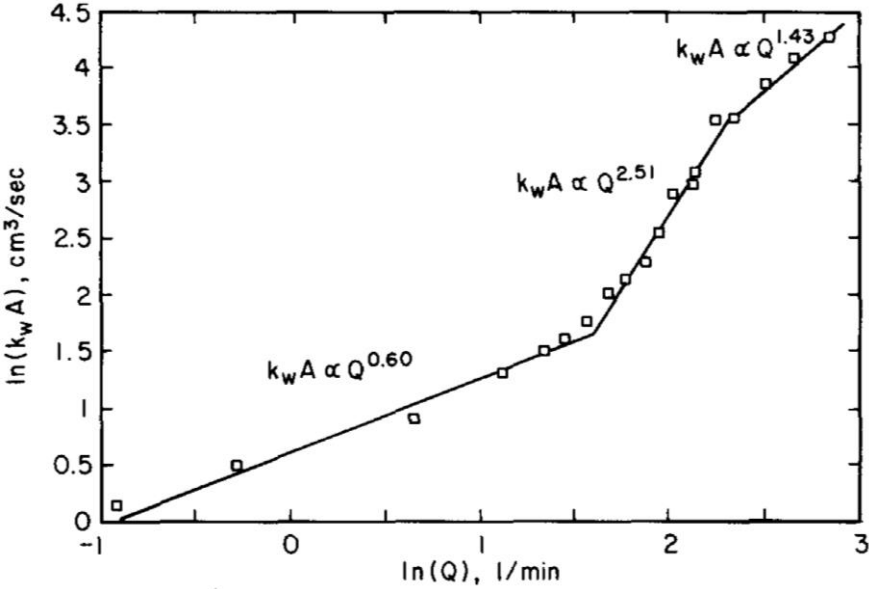


Figure 6.1 – The experimental work of Kim *et al* [14] showing the variation of $K_w A$ as a function of gas flow rate for central tuyeres injection.

We could take advantages of the works form Kim *et al* [14] which is very well documented and presents values for the volumetric mass transfer of a liquid/liquid system with different gas flow rates, nozzle diameters and positions and oil layer viscosity. However, even though the dimensions of such used system are reduced as compared to the ones of an industrial system, they would still make the calculation time and mesh requirements prohibitive to be fully modeled in the framework of the present PhD study. For that reason, we reproduced the works from Kim *et al* [14] in a reduced scale. We will present in more details the Kim

configuration as well as the model proposed to extract physical data to validate the mass transfer models in the following sections.

6.1.1 Mass Transfer in a Ladle Model

To measure liquid/liquid mass transfer Kim *et al* [14] used a scaled model of a ladle with dimensions as schematic described in Figure 6.2. The model preserved the shape of a real ladle, with a conical section with smaller bottom diameter as compared to the upper diameter. The partition ratio of sulfur between slag and metal is on the order of 200 to 500 [14], resulting in the liquid phase mass transfer controlled by metal phase resistance. Therefore, an ideal cold model system using water to simulate the liquid steel, thymol ($C_{10}H_{14}O$) as a tracer, and a 50/50 mixture (by volume) of paraffin oil and cottonseed oil as the slag phase was adopted because the partition ratio of thymol in this system is high (>350).

Typically, 75 l of water containing 120 to 130 ppm thymol was placed in the ladle model followed by placing 2.5 l of oil on top. This is the approximate steel to slag volume ratio used in actual practices. After gas stirring is started, samples are taken out of the water as a function of time. The samples were analyzed by a UV-spectrophotometer to determine the concentration of the transferred species in water.

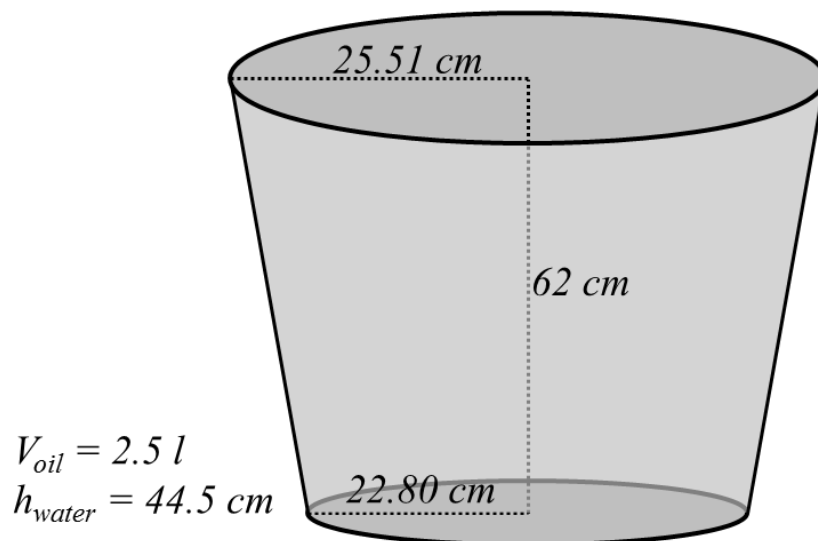


Figure 6.2 - Scheme of the dimension of Kim's experiments.

The mass transfer equations for the model system are the same as for a real system. The mass transfer equation in the case of liquid phase mass transfer due to the resistance of the water phase boundary layer can be expressed as:

$$\frac{dC_w}{dt} = \frac{k_w A}{V_w} (C_w - C'_w) \quad 6.1$$

Where C is the concentration, A is the area of mass exchange, k the mass transfer coefficient and the subscripts w refers to the water phase and o to the water phase. The superscript $[']$ refers to the interface position. As the interface concentration cannot be determined, we refer to the partition ratio as

$$h = \frac{C'_w}{C_o} \quad 6.2$$

And the mass balance for the transferred species

$$(C_w^0 - C_w)V_w = C_o V_o \quad 6.3$$

Therefore, by combining the above equations, we have

$$\int_{C_w^0}^{C_w} \frac{dC_w}{(1 + h V_w/V_o)C_w - h C_w^0 V_w/V_o} = \frac{k_w A}{V_w} \int_0^t dt \quad 6.4$$

The integration of Eq.(6.4) yields the following form of mass transfer equation for a constant partition ratio

$$\frac{\ln[(1 + h V_w/V_o) C_w/C_w^0 - h V_w/V_o]}{1 + h V_w/V_o} = \frac{k_w A}{V_w} t \quad 6.5$$

The expression of Eq.(6.5) can be expressed in a simplified manner as

$$L. H. S. = f(C_w) = K_w A t \quad 6.6$$

And by measuring the concentrations during the time of the experiments one will find the mass transfer parameter $K_w A$ as the slope of the curve, as demonstrated in Figure 6.3:

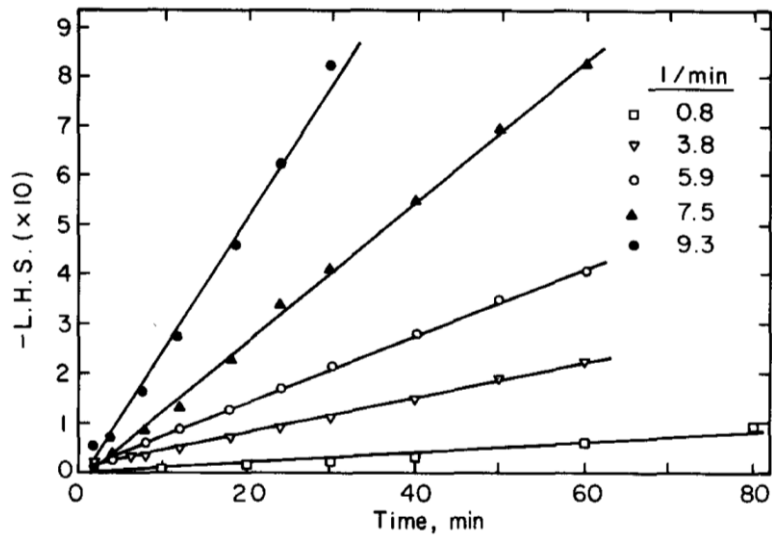


Figure 6.3 - Relationship between L.H.S. of mass transfer Eq. (6.6) and time from Kim *et al* [14].

Kim *et al* [14] performed this experiment for different water flow rates, nozzle positions and nozzle diameters. The results of the trials with the centered nozzle are presented in Figure 6.1. As it shows, many mass transfer experiments could be modeled from Kim's work. However, in order to reduce the computational requirements and reduce the calculation time, we decided to reproduce the experiments proposed by Kim *et al* [14] [14] in a simplified version. Our liquid/liquid mass transfer experiments are presented in the following sections.

6.1.2 Simplified liquid/liquid mass transfer experiments

To reduce the scales and the posterior computation domain, a small model with a squared section is proposed. The squared section representation of the ladle was chosen to simplify the meshing requirements. The reduced model is 270 mm height with sides' length of 200 mm. The water volume used in these experiments was 8 l which were covered with 400 ml of an oil layer. The water and oil layer height was 200 mm and 10 mm respectively. The same 50/50 mixture (by volume) of paraffin oil and cottonseed oil was used to simulate the slag. Similarly, the tracer substance used was thymol, which was firstly dissolved to the saturation level of 0.9 g/l in the water phase.

The air was injected through a 3/16 inch diameter nozzle and the flow rate was defined with the modified Froude Number used to correlate the flow rate between Kim's model and the present one. The equation used to correlate the gas flow rates between the two models is presented in (6.7) and the corresponding air flow rates are in Table 6.1 as:

$$Q_{model} = 1.038\lambda^{5/2}Q_{kim}$$

6.7

Table 6.1 – Corresponding gas flow rates from Kim *et al* [14] to the present model.

Q_{kim} (l/min)	Q_{model} (l/min)
2.954	0.4
3.692	0.5
4.431	0.6
5.169	0.7
5.908	0.8
6.646	0.9
7.385	1
10.338	1.4
14.769	2

The simplified model is presented in Figure 6.4. The structure is built in acrylic, which is inert to the fluids used and the tracer, provoking no reactions during the trials. The thymol concentration was measured with a refractometer, depicted in Figure 6.5.



Figure 6.4 - Physical model used to perform the mass transfer experiments



Figure 6.5 - Light Refractometer used to measure thymol concentration from samples in trials.

Twelve experiments were conducted in order to evaluate the effects of the gas flow rate on the mass transfer parameter. During the experiments, water samples were taken and analyzed

every 5 minutes. The evolution of the LHS of Eq.(6.5) from three of these experiments is plotted in Figure 6.6. The slopes of these curves provide the mass transfer parameters shown in Table 6.2.

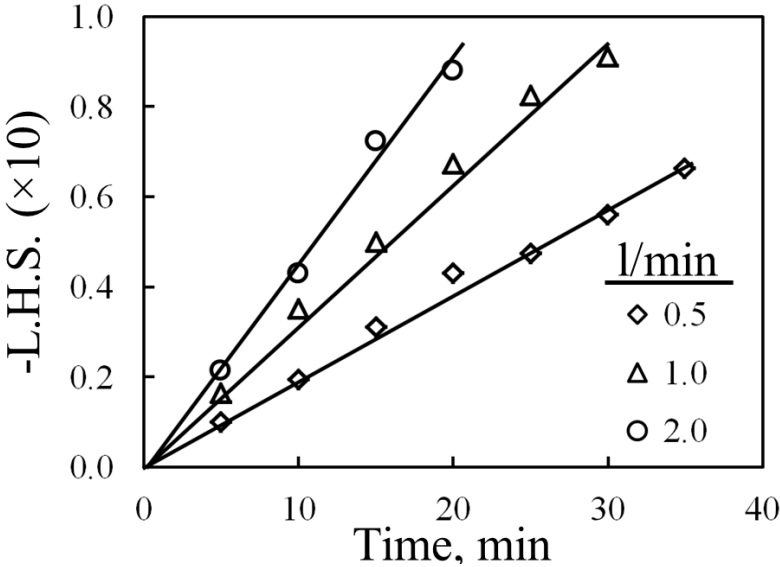


Figure 6.6 - LHS evolution in our experiments.

In a few cases, *e.g.* 0.6, 0.8 and 0.9 l/min, we could perform the experiment twice in order to confirm the mass transfer measured. This limited number of duplicate experiments was due to time constraints linked with the equipment rent.

The mass transfers measured are plotted as a function of gas flow rate in Figure 6.7. One can see the three regimes identified by Kim *et al* [14]. The characteristics of these regimes are the same as described by Kim *et al* [14]. In the first region, the interface is relatively stable with only few perturbations due to the bubbles passage across the oil layer. By increasing the gas flow rate the water/oil interface became more unstable and we observed the appearance of the first oil droplets, which remained close to the interface region. These droplets increase the area for mass exchange and the mass transfer is enhanced. In the later regime, more droplets are formed and dragged into the bulk flow. Some oil emulsion was formed at the extremities of the open-eye. The formation of these droplets and emulsions contribute to the increase of the total interface area and mass transfer.

Table 6.2 – Mass transfer parameters from different gas flow rates.

Trial	Water Flow Rate [l/min]	kA/V [min ⁻¹]
1	0.4	0.00166
2	0.5	0.00178
3	0.6	0.00183
4	0.6	0.00187
5	0.7	0.00204
6	0.8	0.00234
7	0.8	0.00254
8	0.9	0.00280
9	0.9	0.00270
10	1	0.00291
11	1.4	0.00357
12	2	0.00457

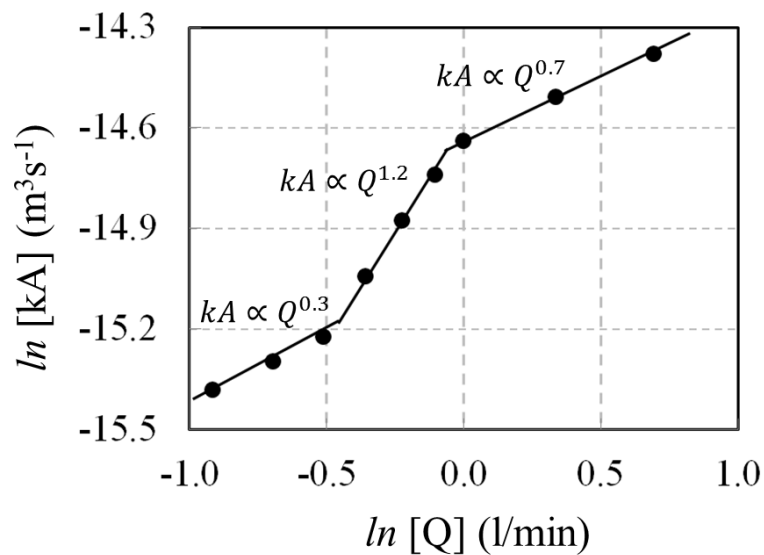


Figure 6.7 – Mass transfer measured in different gas flow rates.

With these measurements we built the data needed to validate the liquid/liquid mass transfer models in a reduced scale.

6.1.3 Simplified liquid/liquid mass transfer modeling

The simplified experiments were simulated with Thetis. The same models, schemes and equations used in the CC modeling were applied. They are explained in the Chapter 4 of this thesis.

To ensure good liquid/liquid interface modeling and accurate velocity calculations close to the interfaces, we need the appropriate mesh size near the interface regions. As stated before in this work, the code Thetis uses a structured mesh and a mesh refinement in one direction drastically increased the number of mesh elements. In order to guarantee the good description of the phenomena involved in an affordable calculation time, we prioritized the mesh refinement at the interface region. Hence, the mesh is denser at the height of the water/oil interface, as observed in Figure 6.8. The maximum mesh size perpendicular to the water/oil interface was 0.5 mm. The calculations ran in 32 processors at the supercomputer Condor in the I2M laboratory at the University of Bordeaux.

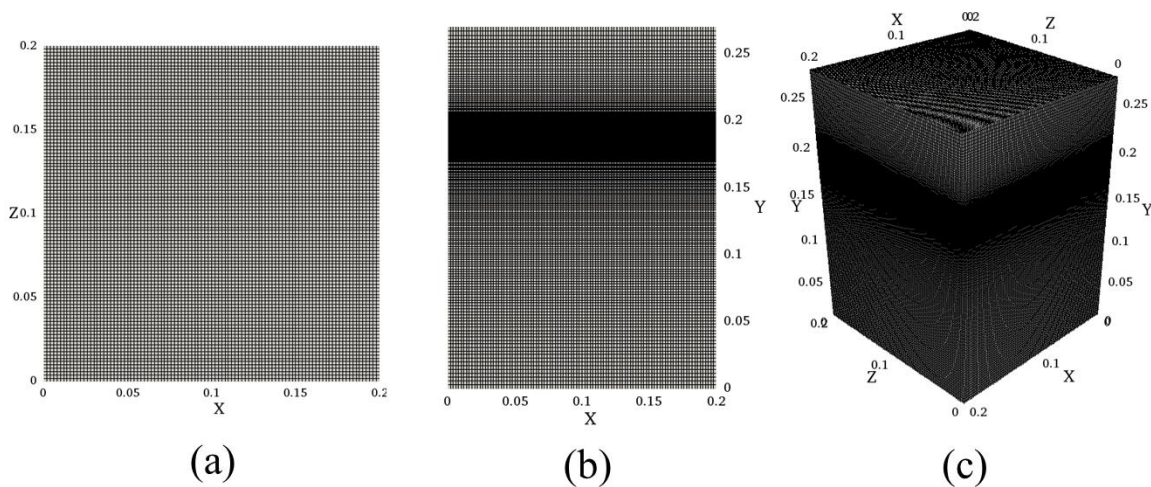


Figure 6.8 – The mesh used during the simulations. (a) the top view, (b) the front view and (c) an isometric view.

The validation criterion we used was the average diameter of the open-eye in the oil layer. This opening phenomenon occurs due to the air bubbles injected from the model bottom crossing the oil layer. It is, then, intimately linked to the system hydrodynamics and interface properties.

To measure the open-eye, many videos were recorded, and images were randomly extracted. The open-eye shape was considered to be perfect circular in order to make such

measurements possible. The diameter of the open-eye was measured with four diagonals traced and its average size was attributed to the diameter of the open-eye captured in this frame. Fifty measures were manually performed in order to have a good representation of the average open-eye diameter.

In the case of the CFD results, an algorithm was used to extract the open-eye contour and calculate its area. The area of the open-eye was considered to be the area of a perfect circle and the diameter of this circle was compared with the values found experimentally. Figure 6.9 shows the procedure of the diameter measurement of the experiments and the CFD results.

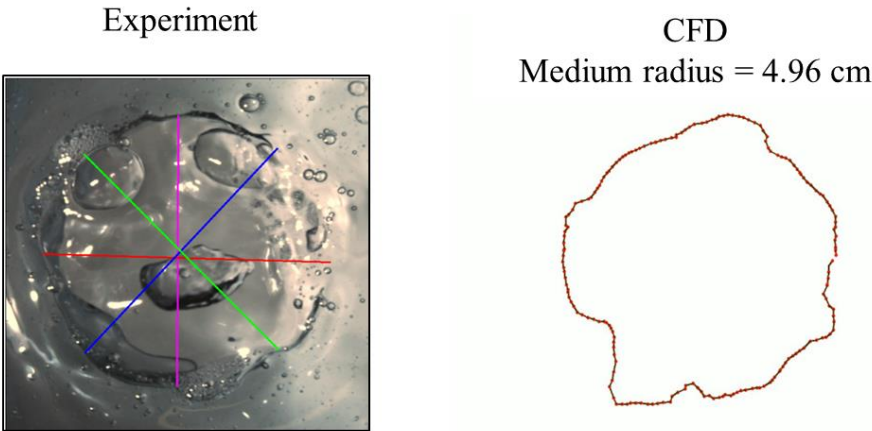


Figure 6.9 – Experimental and numerical open-eye size measurement.

The comparison of the CFD and experimental results is shown in Figure 6.10. Good agreement was found between the experiments and calculations in the first zone. This can be explained by the fact that the configurations at this zone present a stable interface, and the accurate description of the flow is more affordable in a relatively coarse mesh. In the second zone, as previously explained, many droplets start to form, and we were no able to compute this droplets formation in our model. This is an indication that the model was not able to correctly predict the perturbations at the interface. Hence, the open-eye, as well as the interface shape as a whole was not well predicted in the zones II and III.

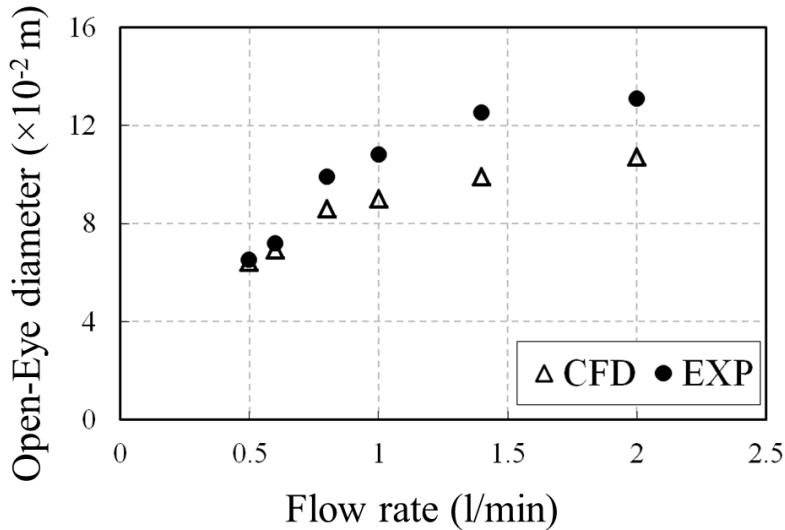


Figure 6.10 - Comparison between CFD and experimental average open-eye diameters.

The mass transfer parameter experimentally measured and described by Eq.(6.6) is multiplied by the exchange area. Hence, those bad interface predictions in the regimes II and III will harm the mass transfer obtained from the CFD model. As an increase in the mesh elements of the models would exorbitantly increase the computational time, we focused our mass transfer validation on the first regime, where the model has achieved good open-eye description with the actual mesh size.

The comparison of the mass transfer parameter measured and calculated by our CFD model, is shown in Figure 6.11. We discovered that relation suggested by the LEM can be used to the liquid/liquid mass transfer configuration with a slightly different coefficient. In this case, the liquid/liquid mass transfer coefficient is given by Eq. (6.8).

$$k = 0.095u^*Sc^{-0.5} \quad 6.8$$

Reasonably good agreement was found for the mass transfer with low gas flow rates at Zone I. The coefficient applied in Eq. 6.8 is very similar to the ones suggested by Banerjee [31], (between 0.108 and 0.158) even though a strange deviation from the experimental data is observed. This slight deviation might be due to the calculation time, which may not have attended a stationary regime. These simulations are still running and the final results are to be published soon.

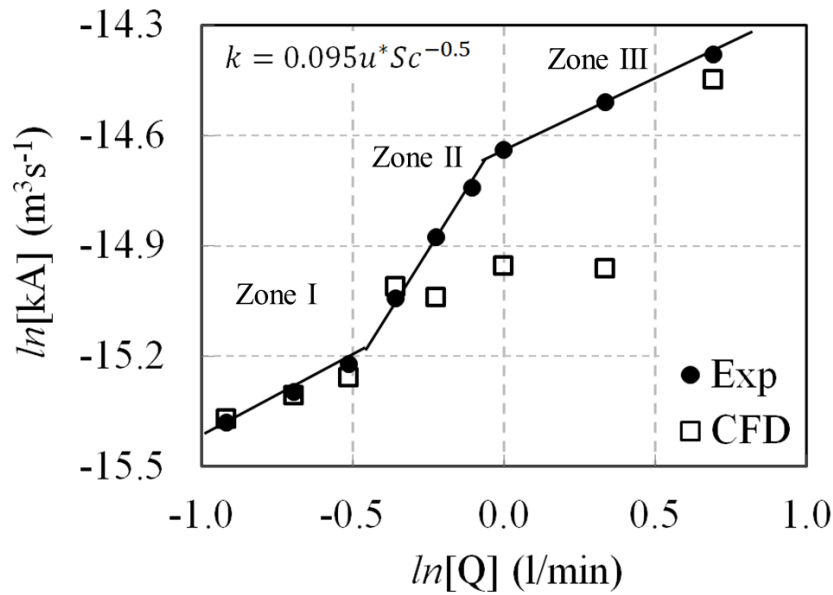


Figure 6.11 - Comparison of the mass transfer parameter measured and calculated from CFD.

At the regions of high gas flow rate, Zones II and III, the CFD mass transfer parameter is much lower. In these regions, if we tried to match the CFD results with the experimental ones, the coefficient in Eq. 6.8 would be higher. This inaccuracy may be due to the reduction of the velocity boundary layer thickness with the increasing of the velocities in the system. A thinner boundary layer needs thinner mesh elements to be fully modeled. This observation was confirmed by the fact that the shear stress continuity was not attained at the liquid/liquid interfaces of the simulations of Zones II and III. To confirm this hypothesis a mesh independence study should be performed.

Figure 6.12 shows the calculated water/oil interface colored by the mass transfer coefficients calculated by Eq.(6.8). One can see that the mass transfer is higher near the borders of the open-eye, where the bubbles cross the interface. This is also the region where higher shear stresses are found. This mass transfer enhancement at the regions where the bubbles cross the interface is important to the CC simulations, since gas injection is used to stabilize the flow in the industrial configuration.

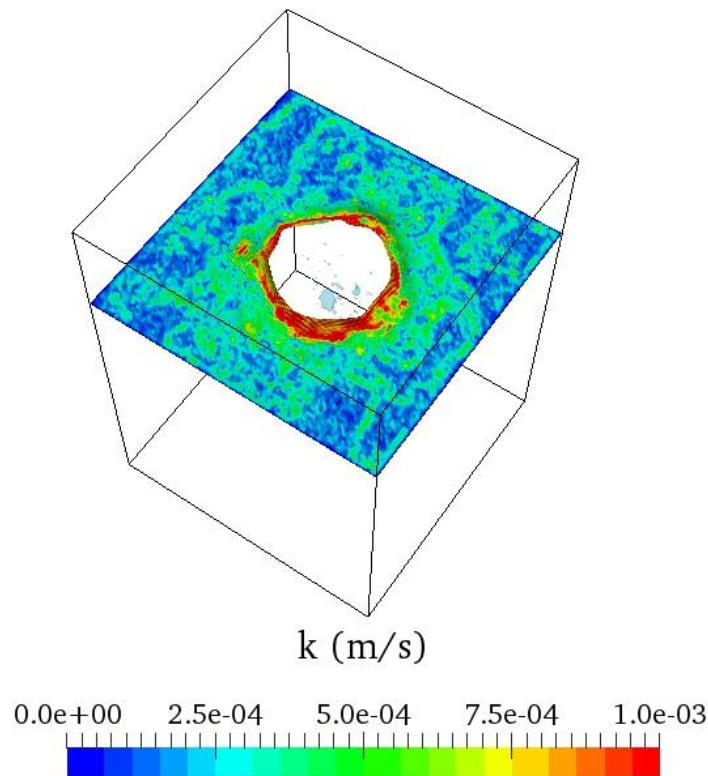


Figure 6.12 - Water/oil interface predicted by our CFD model. The gas flow of this simulation is 0.5 l/min. The interface is colored by the calculated mass transfer coefficient.

6.1 Conclusion

In this chapter, we described the mass transfer experiments used to validate the mass transfer models proposed in section 2. As one may remember, those mass transfer models were conceived for a liquid/gas mass transfer and we needed experimental data to evaluate its usability in a liquid/liquid environment.

We proposed a simplification of the cases studied by Kim *et al* [14], where the liquid/liquid mass transfer could be experimentally measured. Then, we performed CFD simulations to evaluate the mass transfer models. To validate the hydrodynamics of the system, we used the open-eye size to compare the experimental and numerical results. It was found that our model was able to accurately predict the interface shape in the first regime of the experiments. Worse results were found in the regimes II and III, where the oil droplets were poorly described by our model. Besides the bad results found in regions II and III, the mass transfer model provided good prediction of the liquid/liquid mass transfer parameter in the first regime. The CC configuration does not present a highly perturbed interface and is comparable

to the interface perturbations found in zone I. Therefore, the mass transfer model could be validated for a low disturbed liquid/liquid interface.

Due to the difficulties to evaluate the mass transfer based on the surface divergence theory (already discussed in Chapter 2), we focused our analyses on the simplified version of the large eddy model which is finally presented in Eq. 6.8. The proportionality of the mass transfer with the shear stress was confirmed, and we can use this model to study the liquid/liquid mass transfer on liquid/liquid interfaces with relatively low perturbations.

7 Mass Transfer on an Industrial Configuration

In the previous sections, we presented the mass transfer models, the mathematical tools used to build the CFD models of this work, and some validation cases used to verify the code accuracy to predict the hydrodynamics of multiphase flows with high density and viscosity ratios at the interface. The last section was concerning the validation of a model to predict the mass transfer on a liquid/liquid scenario. We have seen that the correlation of the mass transfer coefficient with the shear stress is applicable to the liquid/liquid case (at least in the cases of low interface perturbation) with a slight different proportionality coefficient. We may now apply this mass transfer model to predict the mass transfer on an industrial case.

The industrial process which we aim at modeling in this work is the continuous casting. Its operation and fundamental parameters were presented in the introductory part of this thesis. We are going to proceed by presenting the CC mold that we modeled to calculate the mass transfer coefficients.

7.1 Continuous Casting – Industrial Configuration

7.1.1 The mold

The continuous casting is used to solidify the liquid steel and produce slabs, blooms or billets. In this work, we are interested in the slab production, which aim at supplying steel sheets, mainly, to the automotive industry. To ensure diversified variety of products, the CC machine needs to be able to cast slabs with different dimensions. Hence, there is no such a unique dimension of the mold of a slab caster. However, some product dimensions are more frequently produced than others, and we will focus our work in a common mold dimension.

The main mold dimensions are the width and the thickness. The mold width typically ranges from 1.2 to 1.6 meters. Some slabs may be casted in bigger or smaller shapes, but the range is typically the one mentioned. The height of the mold is usually about 1.0 m. However, to simulate the CC it often simulated the domain where there is still liquid metal inside the steel shell. This length is the *metallurgical length*, and the simulated metallurgical length has an important influence when simulating the CC because of the bottom loop formed during the liquid steel injection. Hence, the CC simulation has to be sufficiently long to avoid

disturbances in the flow coming from the bottom. Zhang [99], for example, studied the inclusion removal process in a CC mold of 1.3 m width and 0.25 m thickness. In his case, he simulated the CC with a height of 2.55 m. Maurya and Jha [100], when studying the effects of the casting speed on a CC slab caster, simulated the mold with 1.64 m width and 0.20 m thickness. The height was 1.64 m and was enough for them to have good results. Kumar [101] simulated a thin CC mold with 1.56 m width and 0.08 m thickness. His simulated height was 1.5 m. Countless studies could be referenced here, but one could see the common range of the mold dimensions in these ones. In the present study, we simulated the industrial CC configuration with a mold of 1.50 m width and 0.22 m thickness. The height of our simulation was 2.5 m to ensure good representation of the phenomena involved in the CC mold.

In order to have results faster, we simulated half of the geometry and considered the symmetry of the system. The configuration studied is shown in Figure 7.1.

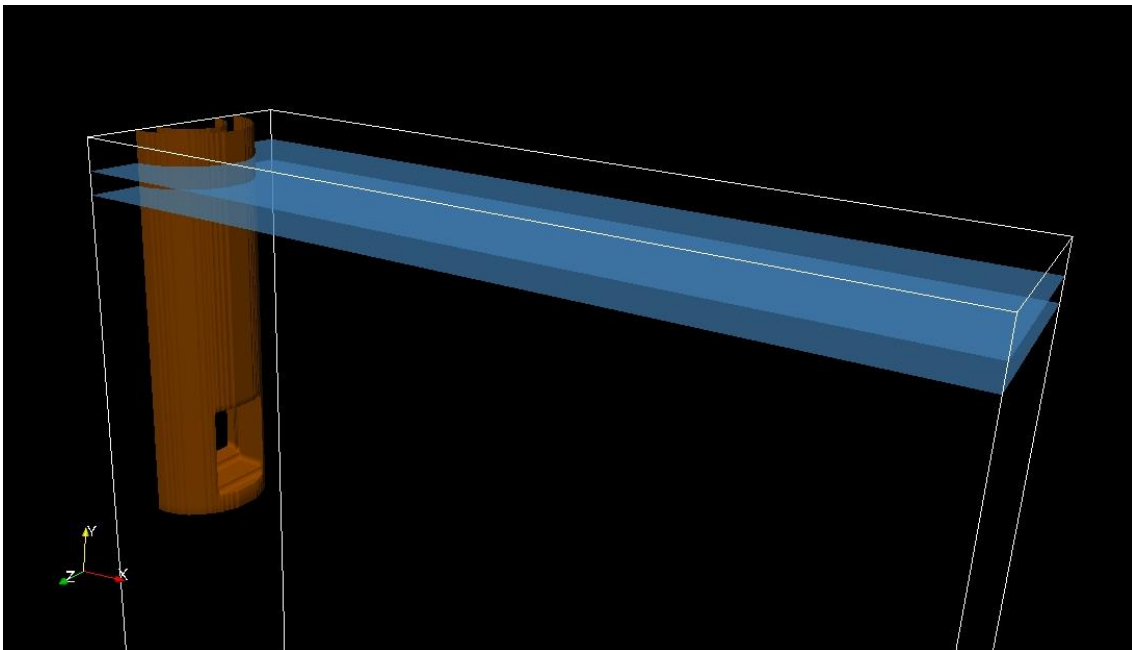


Figure 7.1 - CC industrial configuration. The simulated domain (half of a complete geometry) was reduced to diminish computational time.

7.1.2 The Submerged Entry Nozzle (SEN)

We have dedicated a section in chapter one to discuss about the nozzle design and the main parameters to be evaluated in its geometry. The nozzle also has no universal form, and its shape is optimized to ensure the best CC performance. Therefore, we used conventional

nozzle geometry to provide results comparable to the ones of the industrial nozzles. The main parameters are the SEN diameter, the nozzle outlet ports, and the outlet angle. In our case, the SEN has 0.12 m diameter, and outlet ports of $0.015 \times 0.020 \text{ m}^2$ and an inclination of 15° . In our simulations, the SEN geometry was defined with the Fictitious Domain Method (FDM) as described in section 4.3. Figure 7.2 shows the nozzle geometry.

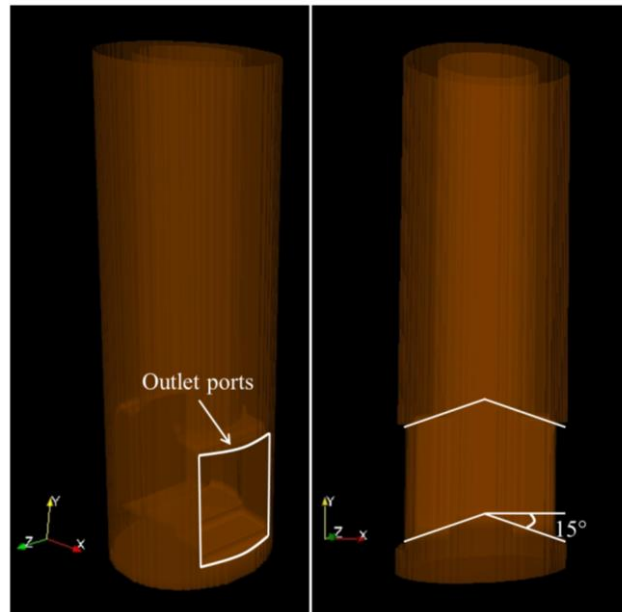


Figure 7.2 - SEN geometry defined in Thetis by the FDM.

7.1.3 The operational conditions

The simulation of the CC machine involves very high viscosity ratios and surface tension effects (steel/slag, steel/argon, slag/argon and steel/slag/argon interfaces). Besides these facts, the presence of three fluids adds even more complexity to the full simulation of an industrial CC configuration. In order to make the CC simulation more affordable, we decided to simplify some aspects of the industrial case and keep the most important phenomena to study the mass transfer between liquid steel and slag. Thus, we did not consider the gas injection (the same was made for the experiments and simulations of chapter 5), neither had we considered the heat transfer and the phase changes of the system. With this simplification, our simulation consisted of CC case with three phases, as there is gas above the free surface of the liquid slag layer. The initial distribution of the phases in our model is presented in Figure 7.1. The density and viscosity of the fluids were that of the industrial process. Attention must be paid to the fact that the liquid steel and slag varies its viscosity with the temperature and

chemical composition. Hence, to make possible the simulation of this process, we used an average density and viscosity for the fluids at 1,600 °C and a typical chemical composition. The fluid properties are summarized in Table 7.1.

Table 7.1 - Fluid properties used in the CC industrial configuration.

	ρ (kg/m ³)	μ (Pa·s)	σ (N/m)
Liquid Steel	7,000	0.005	1.2
Liquid Slag	2,700	0.070	

The operational conditions might also affect the stability of the simulations. The casting speed has strong influence on the steel quality, and during CC operation it may vary according to the desired product quality. To avoid problems due to very high speeds in such a multiphase environment, we simulated a very low casting speed, yet in a typical industrial range. The casting speed of our simulation is about 0.8 m/min (m/min is the usual unit adopted by steelmakers). This casting speed is defined by the inlet velocity at the SEN, which is 1.2 m/s. The Reynolds number of the liquid injection is of the order of 1×10^5 , which characterizes a turbulent flow.

7.2 CFD Model Results

The CC configuration model was built in a cartesian staggered grid composed of 5.7 million mesh elements. The computation ran on 128 cores at the super computer Condor in the I2M laboratory. Because of its complexity, the time steps were reduced to $\Delta t = 0.5 \times 10^{-4}$ seconds as compared to the ones from the simulations of the experiments ($\Delta t = 1.0 \times 10^{-4}$). The model ran during 90 days to achieve roughly 55 seconds of physical time. The average analysis was performed on the last 30 seconds of calculations to avoid perturbations from the low velocity values from the starting point.

7.2.1 Hydrodynamic aspects

The hydrodynamics of the industrial configuration is quite similar to that of the physical experiments presented in Chapter 5. The main flow pattern, the double loop, was also verified.

We observed a boundary layer near the liquid steel/slag interface. As an example, we plotted in Figure 7.3 three velocity profiles at 30, 50 and 60 cm from the center position of the SEN. This boundary layer is an effect of the high viscosity of the upper phase. This phenomenon was already explained in Chapter 5, when we discussed the presence of the same boundary layer at the oil/water interface.

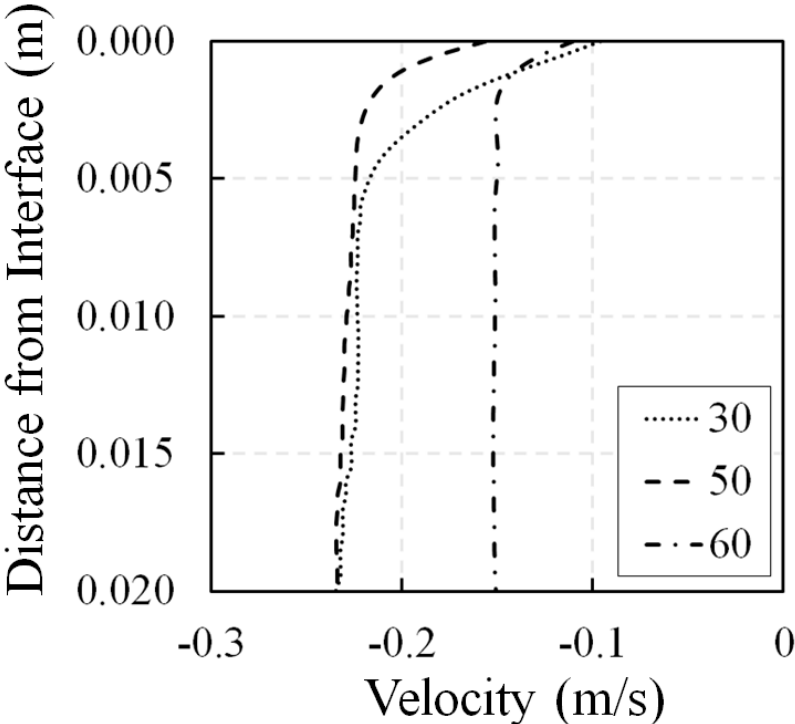


Figure 7.3 - Horizontal Velocity component profile at different distances from the SEN (30, 50, 60 cm).

The interface did not present strong perturbations and was fairly stable during the simulations. We verified the continuity of the shear stress constraint in both sides of the liquid steel/slag interface. With these velocity profiles, we could apply the mass transfer model previously validated to evaluate the mass transfer coefficient distribution over the liquid steel/slag interface. The results are presented in the following section.

7.2.1 Mass Transfer Coefficient

By applying the mass transfer correlation (Eq. 6.8) validated at low disturbed interfaces in Chapter 6, we observed similar results as the ones found during the simulations of the

experimental configuration. The mass transfer coefficients are not homogeneously distributed over the liquid steel/slag interface as shown in Figure 7.4.

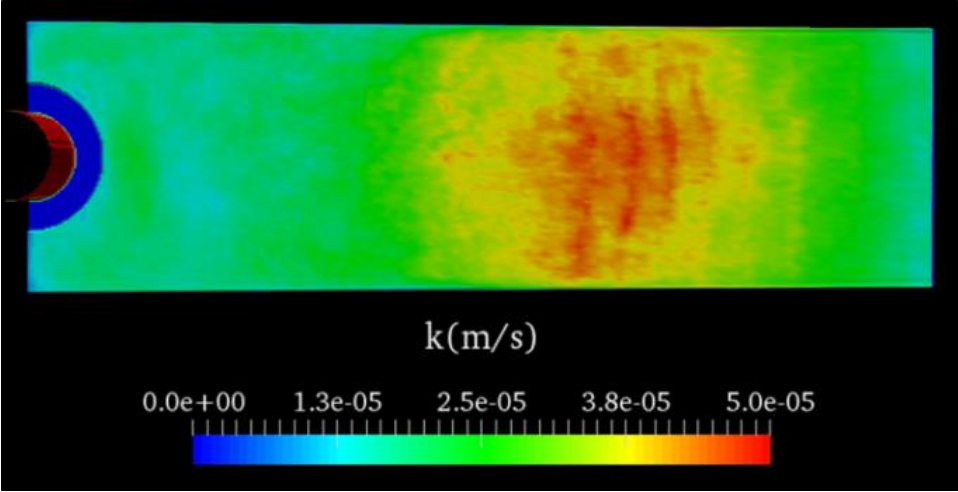


Figure 7.4 - Mass Transfer Coefficient distribution at a liquid steel/slag interface ($Sc = 1 \times 10^3$). Values averaged over 30s.

Again, we have higher mass transfer coefficients in the regions where the shear stresses are higher, e.g. where the upper loop touches the interface (Figure 7.5). This result is related to the mass transfer model implemented, in which the mass transfer coefficient was proved to correlate with the interface shear stress.

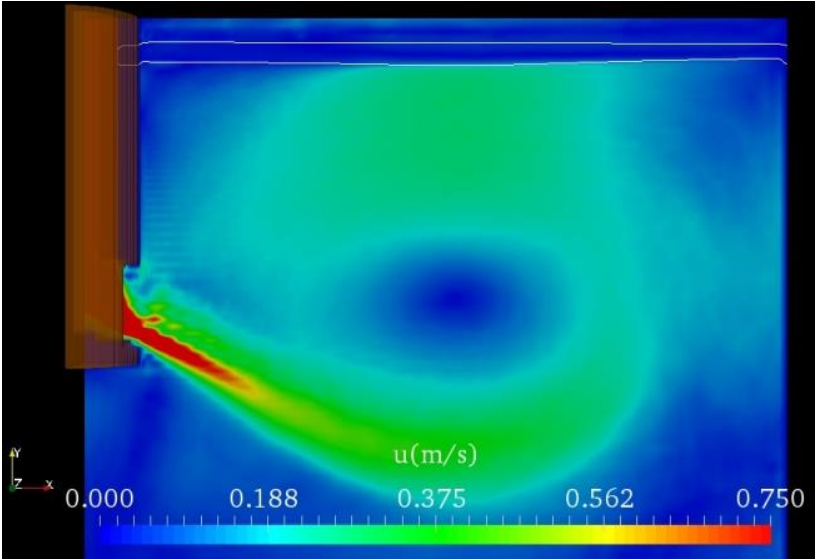


Figure 7.5 – Averaged velocity profile at the symmetry plane of the CC mold. The upper loop touches the interface at the same position where the higher mass transfer coefficients were observed.

These findings on the inhomogeneity of the mass transfer coefficients help to explain the variances of the chemical composition of the slag during industrial trials. Even when the samples are taken under the same conditions and at the same time, differences in the chemical composition are observed. Chaubal *et al* [94] [102] developed a simplified model to predict the slag chemical composition. To validate their model, they took samples of the slag on a CC and compared the MnO content measured and predicted. The measurements have shown a wide dispersion, even the ones taken at the same time (Figure 7.6). This might be an indication of the inhomogeneity of the mass transfer coefficients, since the samples are not rigorously taken at the same location on an industrial process. The sampling is usually performed at the places of easiest access where safety is a priority. Due to process instabilities, these sample regions may vary from one sampling to another and, therefore, the chemical composition may present itself a variation proportional to the mass transfer coefficient distribution.

To confirm this hypothesis, an industrial trial should be performed, where slag samples must be deliberately taken in different regions and the chemical composition evaluated. With these results, we could see if the chemical compositions vary more rapidly in one region as compared to the other one.

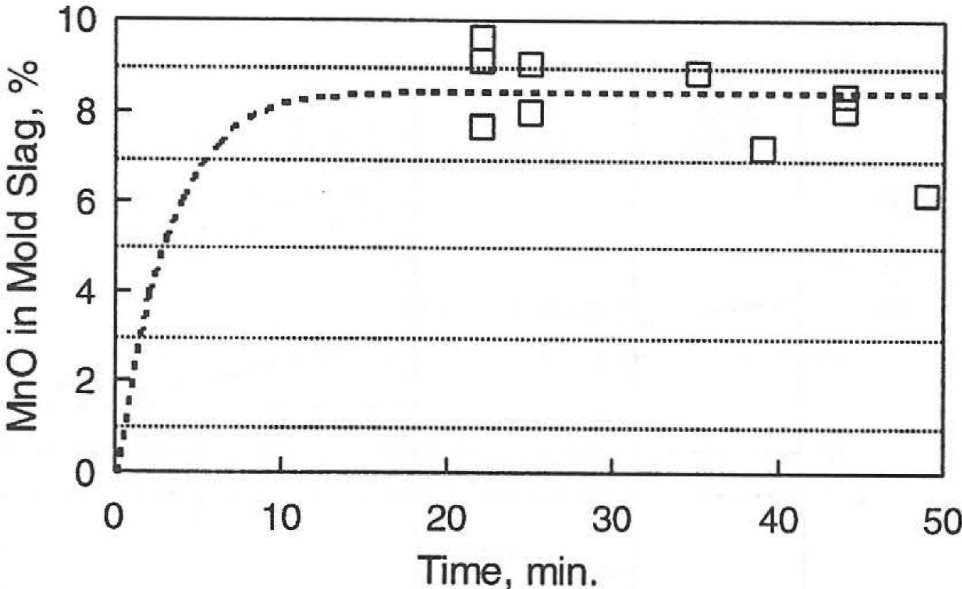


Figure 7.6 - Measured and predicted MnO content of slags in a CC machine during the casting of a free-machining steel. Work presented by Chaubal *et al* [94] [102].

Another important remark is the absence of the gas injection in these simulations. The bubbles are commonly used to inert the SEN and avoid the nozzle clogging from oxides formed inside. These bubbles emerge around the SEN and as we have seen in the previous chapter, it may enhance the mass transfer when crossing the interface. Hence, the presence of the bubbles injected may change the distribution of the mass transfer coefficients. New simulations must be performed to evaluate the gas injection influences.

7.3 Conclusion

In this chapter, we have presented the industrial application of the mass transfer correlation validated in a liquid/liquid configuration during the thesis. We briefly described the CC mold simulated, the phases and industrial conditions, and we explained the simplifications made in order to make this simulation affordable and feasible within the thesis framework.

The hydrodynamics of the CC industrial configuration presented some similarities with the water models used in Chapter 5. We have seen that a viscous boundary layer is present near the liquid steel/slag interface. The double loop pattern of the flow was verified and we focused our analysis on the upper loop due to its direct influence on the mass transfer. It was seen that the regions where the upper loop touches the liquid steel/slag interface are the regions where the highest mass transfer coefficients are found. This happens because the mass transfer model used predicts the mass transfer coefficient based on the shear stress at the interface and Sc number.

The mass transfer coefficients are not homogeneously distributed in the liquid steel/slag interface. This implicates that in the regions of high mass transfer coefficient the local chemical composition is likely to change faster than in the regions with low mass transfer rates. Therefore, the physical properties of the slag, which are dependent on the slag chemical composition, will not be homogeneously distributed. The implications of these findings on CC operations are probably the need of different flux powder to be used in order to better control the slag properties and ensure the appropriate mold lubrication.

Nonetheless, due to the time needed to perform the simulations, we did not consider the argon injection. The gas bubbles may change the mass transfer distribution, homogenizing the mass transfer over the liquid steel/slag interface. Further studies are needed to evaluate the impact of the gas injection on the mass transfer distribution in this CC industrial configuration.

8 Conclusions

The main objective of the present study was to characterize the liquid/liquid mass transfer phenomena and to apply the generated models on industrial processes. We started with a broad idea of what could be achieved and readily identified the technical hitches to fully achieve our objectives.

Many numerical studies had already been performed in order to characterize the mass transfer in a gas/liquid configuration and they were used as the starting point for this project. At first, we performed a deep review of the existing mass transfer models and the methodologies used to build them.

The first point was the characterization of the hydrodynamic aspects of the regions near the liquid/liquid interface. We performed original experimental measurements to have enough data to validate our future model. Measurements were made with LDA equipment in a physical water model of a CC mold. Many configurations were tested in order to obtain good interface stability, allowing us to take velocity measurements very close to a water/oil interface. The measurements were taken under different operational conditions and we could evaluate the impact of some industrial parameters, such as casting speed, slag viscosity and thickness, on the interface behavior. These results were the subject of four international conference presentations [103] [104] [105] [106].

At the same time, we performed CFD simulations of the most stable configurations. The calculations generated liable results and confirmed the trends observed experimentally. The increase in the casting speed was shown to increase the turbulence into the whole system and to increase the interface shear stress, thus, contributing to the mass transfer as we will discuss later. The upper phase viscosity has little effect on the interface shear stress. It slightly increases the shear stress when the upper phase viscosity is increased. The thickness of the upper phase has an important role on the interface stability. It was seen that a thick oil layer presented a very disturbed interface, whilst a thin oil layer is much more easily pushed away from the walls.

The validated simulations were used to investigate the turbulence near the liquid/liquid interface. For the first time it was proved through experimental measurements that the use of a single-phase LES turbulence model, which does not take into account all the terms related to the presence of an interface, can be used for a turbulent multi-phase flow simulation. This

conclusion is valid for the cases where the interface between the phases is not strongly deformed and the flow is mostly parallel to it.

It was seen that the viscous oil layer was regarded as a movable wall by the water phase. This was indicated by the boundary layer found beneath the water/oil interface. A similar behavior was observed on the industrial simulation, where the upper phase is the liquid slag, far more viscous than the molten steel. This boundary layer was also observed in the water/air configuration, but animations produced with the CFD results showed that the boundary layers observed in the water/air configuration were an effect of the time averaging velocities near the water/air interface.

With the validated velocity profiles near the liquid/liquid interface, we could evaluate the mass transfer model most suitable for our purposes. We concluded that the most suitable model, for our applications, is the simplified version of the Large Eddy Model (LEM). This model suggests that the mass transfer coefficient is proportional to the shear stress at the liquid/liquid interface and the inverse of the root square of the Sc number. The LEM avoid all the ambiguities of other models, such ambiguities include the definition of the Reynolds number based on global velocity and length scales, as well as the miss definition of the methodologies of the Surface Divergence Model (SDM) to compute the rms values of the interface divergence field in perturbed interfaces, where droplets are usually present.

Difficulties arose when we perceived the lack of data to validate liquid/liquid mass transfer models. Because of these, we built a small scale representation of the work performed by Kim *et al* [14] and we could built our own mass transfer dataset to validate the mass transfer model. The validation was only possible in the cases with low interface perturbations, which is comparable to the situation we have in the simulated continuous casting configurations. Conversely, the mass transfer correlation found in the liquid/liquid mass transfer simulations, presented similar coefficient of about 0.1, while the suggested values are between 0.108 and 0.158 for gas/liquid mass transfer. This mass transfer correlation provided reasonable results only in the cases with low interface perturbations, *e.g.* low gas flow rates. For the high gas flow rates configuration, the predicted mass transfer coefficients were lower than the experimental values, indicating an under resolved calculation in the interface shear stress. As the velocities in the system are increased, the interface shear stress increases and the viscous boundary layer at the liquid/liquid interface is reduced and a refined mesh is needed to accurately compute the flow. This observation must be confirmed by a mesh independence study, which is one of the proposed studies for a near future.

The validated liquid/liquid mass transfer correlation was applied to the simulation of an industrial continuous casting configuration, where some simplifications were made in order to make it more affordable and less time consuming. The results indicated the non-homogeneity distribution of the mass transfer coefficients over the liquid steel/slag interface. With this distribution, it is expected that the mass transfer rate should be different in the regions of the mold, affecting the slag properties and causing instabilities during the process. However, in a real process, argon is injected through the SEN to avoid the nozzle clogging, and it also may affect the mass transfer coefficients distribution. We have seen in Chapter 6 that mass transfer is enhanced in the regions where the bubbles cross the interface. In the CC configuration, the argon bubbles usually cross liquid steel/slag interface in the regions around the SEN, where we observed the lower mass transfer coefficients in our simulation. Therefore, we can predict the argon injection may make the mass transfer more uniform over the liquid steel/slag interface, by increasing the mass transfer rates at the regions around the SEN. However, we can only verify this assumption by proceeding with a new simulation of the CC configuration with argon injection, or by analyzing samples taken in an industrial CC mold. Both of these suggestions are in the perspectives for the ongoing projects.

As a final conclusion, the liquid/liquid mass transfer is proved to follow the proportionality with the interface shear stress and can be calculated based on the simplified version of the LEM proposed by Banerjee *et al* [33]. However, further studies, with improved mesh refinement in the interface region should be performed to verify the good mass transfer coefficient to be applied on high disturbed interfaces.

We have good perspectives for the present work. The future studies ongoing this project are:

- Mass transfer correlation: it will be extremely interesting to perform new simulations with an adaptive mesh code in order to achieve optimum mesh refinement without compromising the simulation efficiency. With this feature, it will be possible to accurately predict the interface shear stress and exchange area.
- Mass transfer experiments: the mass transfer experiments are based on the assumption of perfect mixture of components into the phases. This assumption may be examined to determine its effect on mass transfer data.
- Industrial configuration: new simulations accounting the gas injection will provide new insights concerning the mass transfer distribution, allowing steelmakers to better design flux powders to be used in the case of casting new grades of high alloyed steels. It will be of great contribution to the advancements of the steelmaking industry.

- Industrial mass transfer measurements: Samples of the slag can be collected during the casting operation. Its chemical composition can be analyzed and the mass transfer coefficients can be extracted to compare with the ones from numerical investigations.

Chemical composition evolution: The mass transfer coefficients calculated with the CFD model might be used as input for computational thermodynamic models to predict chemical slag composition evolution during the casting. This prediction may be of great use for steelmakers when designing flux powders to successfully cast new products.

9 References

- [1] Steel Feel 2016. [Online]. Available: <http://steelfeel.com/mechanical/steel-making-process/>. [Accessed 01 11 2016].
- [2] I. Hikoya and K. Kunisada. Desulphurization and Simultaneous Desulfurization and Dephosphorization of Molten Iron by Na₂O-SiO₂ and Na₂O-CaO-SiO₂ Fluxes. *ISIJ International*, vol. 29, no. 2, pp. 135-139, 1989.
- [3] JFE 21st Foundation, Century http://www.jfe-21st-cf.or.jp/chapter_2/2j_2_img.html.
- [4] World Steel Association. World Steel Association. [Online]. Available: www.steeluniversity.org. [Accessed 01 08 2016].
- [5] K. Ogawa and T. Onoue. Mixing and Mass Transfer in Ladle Refining Process. *ISIJ International*, vol. 29, no. 2, pp. 148-153, 1989.
- [6] B. G. Thomas. Continuous Casting of Billets, Blooms and Slabs, vol. I, The University of British Columbia, April, 1993.
- [7] M.E.A. Görnerup. Mold fluxes in continuous casting of steel - characterization and performance tuning. *VII International Conference on Molten Slags Fluxes and Salts*, 2004.
- [8] A.E.A. Azhari. An investigation in mold powders properties consumed in Iran, vol. 4, 2007.
- [9] Continuous Casting Consortium. [Online]. Available: <http://ccc.illinois.edu/introduction/overview.html#schematics>. [Accessed 20 07 2016].
- [10] R. P. Tavares. Mass Transfer in Steelmaking Operations.
- [11] S.-y. e. a. Kitamura. Analysis of Dephosphorization Reaction Using a Simulation Model of Hot Metal Dephosphorization by Multiphase Slag. *ISIJ International*, vol. 49, no. 9, 2009.
- [12] V.E.A. Singh. A Novel Bottom Stirring Scheme to Improve BOF Performance through Mixing and Mass Transfer Modeling. *ISIJ International*. vol. 49, no. 12, 2009.
- [13] K. Ogawa and T. Onoue. Mixing and Mass Transfer in Ladle Refining Process. *ISIJ International*, vol. 29, no. 2, 1989.
- [14] S.H. Kim and R. Fruehan. Physical Modeling of Gas/Liquid Mass Transfer in a Gas Stirred Ladle. *Metallurgical Transactions B*, pp. 673-680, December 1987.

- [15] C. Gualtieri and P. Doria. Gas-transfer at unsheared free-surfaces, 2nd Edition ed., Taylor and Frances Group, 2008.
- [16] P. Lombardi, V. de Angelis and S. Banerjee. Direct numerical simulation of near-interface turbulence in couples gas-liquid flow. *Physics of Fluids*, vol. 8, pp. 1643-1665, 1996.
- [17] S. Banerjee and S. MacIntyre. The air-water interface: turbulence and scalar exchange, Santa Barbara: Department of Chemical Engineering - University of California.
- [18] M.Y. Lin, C.H. Moeng, W.T. Tsai, P. P. Sullivan and S. E. Belcher. Direct numerical simulation of wind-wave generation processes. *Journal of Fluid Mechanics*, vol. 616, pp. 1-30, 2008.
- [19] S. Komori, R. Kurose, I. Koji, T. Ukai and N. Suzuki. Direct numerical simulation of wind-driven turbulence and scalar transfer a sheared gas-liquid interfaces. *Journal of Turbulence*, vol. 11, no. 32, pp. 1-20, 2010.
- [20] D. E. Turney, W. C. Smith and S. Banerjee. A measure of near-surface fluid motions that predicts air-water gas transfer in a wide range of conditions. *Geophysical Research Letters*, vol. 32, 2005.
- [21] W. L. Peirson, J. W. Walker and M. L. Banner. On the microphysical behaviour of wind-forced water surfaces and consequent re-aeration. *Journal of Fluid Mechanics*, vol. 743, pp. 399-447, 2014.
- [22] S. Kline, W. Reynolds, F. Schraub and P. Runstadler. The structure of turbulent boundary layers. *Journal of Fluid Mechanics*, vol. 30, pp. 741-773.
- [23] J. G. Venditti, J. L. Best, M. Church and R. J. Hardy. Coherent Flow Structures at Earth's Surface. Wiley Blackwell, 2013.
- [24] A. Perry, T. Lim and E. The. A visual study of turbulent spots. *Journal of Fluid Mechanics*, vol. 104, pp. 387-405, 1981.
- [25] I. Calmet and J. Magnaudet. Large-eddy simulation of high-Schmidt number mass transfer in turbulent channel flow. *Physics of Fluids*, no. 9, p. 438-455, 1997.
- [26] Y. Hasegawa and N. Kasagi. Effects of interfacial velocity boundary condition on turbulent mass transfer at high Schmidt numbers. *International Journal of Heat and Fluid Flow*, vol. 28, pp. 1192-1203, 2007.

- [27] D. E. Turney and S. Banerjee. Air-water gas transfer and near-surface motions. *Journal of Fluid Mechanics*, vol. 733, no. doi:10.1017/jfm.2013.435, pp. 588-624, 2013.
- [28] N. Takagaki, R. Kurose, Y. Tsujimoto, S. Komori and K. Takahashi. Effects of turbulent eddies and Langmuir circulations on scalar transfer in a sheared wind-driven liquid flow. *Physics of Fluids*, vol. 27, 2015.
- [29] M. Rashidi and S. Banerjee. The effect of boundary conditions and shear rate on streak formation and breakdown in turbulent channel flows. *Physics of fluids*, vol. 2, no. 10, pp. 1827-1838, 1990.
- [30] S. T. D. Banerjee. Transport Phenomena at Interfaces Between Turbulent Fluids. Wiley InterScience (www.interscience.wiley.com), December 28, 2007.
- [31] S. Banerjee. Turbulence structure and transport mechanisms at interfaces. *9th International Heat Transfer Conference*, 1990.
- [32] S. Liu, A. Kermani, L. Shen and . D. K. P. Yue. Investigation of coupled air-water turbulent boundary layers using direct numerical simulations. *Physics of Fluids*, no. 21, 2009.
- [33] S. Banerjee, D. Lakehal and M. Fulgosi. Surface divergence models for scalar exchange between turbulent streams. *International Journal of Multiphase Flow*, no. 30, p. 963–977, 2004.
- [34] Banerjee, Scott and Rhodes. Mass Transfer to Falling Wavy Liquid Films in Turbulent Flow. *Industrial Engineering Chemical Fundamentals*, no. 7 (1), p. 22–27, 1968.
- [35] M. Fulgosi, D. Lakehal, S. Banerjee and v. De Angelis. Direct numerical simulation of turbulence in a sheared air–water flow with a deformable interface. *Journal of Fluid Mechanics*, vol. 482, p. 319–345, 2003.
- [36] Y. Cohen, D. Mackay and W. Y. Shiu. Mass Transfer Rates Between Oil Slicks and Water. vol. 58, pp. 569-575, 1980.
- [37] J. M. Santos, V. Kreim, J.-M. Guillot, N. Costa Reis Jr, L. M. de Sa and N. J. Horan. An experimental determination of the H₂S overall mass transfer coefficient from quiescent surfaces at wastewater treatment plants. *Atmospheric Environment*, vol. 60, pp. 18-24, 2012.
- [38] S.H. Kim and R. Fruehan. Physical Modeling of Gas/Liquid Mass Transfer in a Gas Stirred Ladle. *Metallurgical Transactions B*, pp. 673-680, December 1987.

- [39] D. Mackay and A. T. K. Yeun. Mass transfer Coefficient correlations for Volatilization of organic solution from water. *Environmental Science and Technology*. vol. 17, no. 4, pp. 211-217, 1983.
- [40] D. E. Turney and S. Banerjee. Air-water gas transfer and near-surface motions. *Journal of Fluid Mechanics*, vol. 733, pp. 588-624, 2013.
- [41] D. Lewis and W. Whitman. Principles of gas absorption. *Industrial and Engineering Chemistry*, vol. 16, pp. 1215-1220, 1924.
- [42] R. Higbie. The rate of absorption of a pure gas in a still liquid during short periods of exposure. *American Institute of Chemical Engineers*, vol. 31, pp. 365-390, 1935.
- [43] P. Dankwerts, Significance of liquid-film coefficients in gas absorption, *Industrial and Engineering Chemistry*, vol. 43, no. 6, pp. 1460-1467, 1951.
- [44] I. Cuesta, F. Grau, F. Giralt and Y. Cohem, Air-water mass transfer of organics from shallow ponds under laminar recirculation, *International Journal of Heat and Mass Transfer*, vol. 42, pp. 165-179, 1999.
- [45] H. v. Limpt, R. Beerkens, A. Lankhorst and A. Habraken, Mass transfer relations for transpiration evaporation experiments, *International Journal of Heat and Mass Transfer*, vol. 48, pp. 4265-4281, 2005.
- [46] S. Komori, Y. Murakami and H. Ueda, The relationship between surface-renewal and bursting motions in an open-channel flow, vol. 203, pp. 103-123, 1989.
- [47] P. Fortescue G, On gas absorption into a turbulent liquid, *Chemical Engineering Science*, no. 9, 1967.
- [48] V. De Angelis, Numerical Investigation and Modeling of Mass Transfer Processes at Sheared Gas-Liquid Interfaces, University of California, Santa Barbara, 1998.
- [49] T. Theofanous, R. Houze and L. Brumfield, Turbulent mass transfer at free, gas-liquid interfaces, with applications to open-channel, bubble and jet flows, *International Journal of Heat and Mass Transfer*, vol. 19, pp. 613-624, 1976.
- [50] M. McCready, E. Vassiliadou and T. Hanratty, Computer Simulation of Turbulent Mass Transfer at a Mobile Interface, *AIChE Journal*, vol. 32, no. 7, pp. 1108-1115, July 1986.

- [51] W. C. Chan and L. E. Scriven, Absorption into Irrotational Stagnation Flow. A Case Study in Convective Diffusion Theory, *Industrial & Engineering Chemistry Fundamentals*, vol. 9, no. 1, pp. 114-120, 1970.
- [52] J. C. R. Hunt and J. M. R. Graham, Free-stream turbulence near plane boundaries, *Journal of Fluid Mechanics*, vol. 84, pp. 209-235, 1978.
- [53] S. Kumar, R. Gupta and S. Banerjee, An experimental investigation of the characteristics of free-surface turbulence in channel flow, *Physics of Fluids*, vol. 10, no. doi: 10.1063/1.869573, pp. 437-456, 1998.
- [54] R. I. Guthrie, *Engineering in Process Metallurgy*, Clarendon Press, 1989.
- [55] M. De Santis, A. Cristallini, M. Rinaldi and A. Sgrò, Modelling-based Innovative Feeding Strategy for Beam Blanks Mould Casting Aimed at As-cast Surface Quality Improvement, *ISIJ International*, vol. 54, no. 3, p. 496–503, 2014.
- [56] R. Kalter, *Electromagnetic control of oscillating flows in a cavity*, Technische Universiteit Delft, 2015.
- [57] DANTEC, Measurement principles of LDA [Online]. Available: <http://www.dantecdynamics.com/measurement-principles-of-lda>. [Accessed 01 08 2016].
- [58] R. Kalter, M. J. Tummers, J. Bettink, B. Righolt, S. Kenjeres and C. Kleijn, Aspect Ratio Effects on Fluid Flow Fluctuations in Rectangular Cavities, *Metallurgical And Materials Transactions B*, vol. 45B, pp. 2186-2193, 2014.
- [59] G. e. a. Pianet, Simulating compressible gas bubbles with a smooth volume tracking 1-Fluid method, *International Journal of Multiphase Flow*, no. 36, 2010.
- [60] J. C. J.-P. Ritz, A numerical continuous model for the hydrodynamics of fluid particle systems, *International Journal of Numerical Methods in Fluids*, vol. 30, p. 1067–1090, 1999.
- [61] J. Brackbill, B. Kothe and C. Zemach, A continuum method for modelling surface tension, *Journal of Computational Physics*, vol. 335, no. 100, p. 335–354, 1992.
- [62] S. Vincent and J.P. Caltagirone, A one cell local multigrid method for solving unsteady incompressible multiphase flows, *Journal of Computational Physics*, no. 163, p. 172–21, 2000.

- [63] S. Vincent, J.P. Caltagirone, P. Lubin and T. Randrianarivelo, An adaptive augmented Lagrangian method for three-dimensional multi-material flows, *Computational Fluids*, no. 33, p. 1273–1289, 2004.
- [64] C. J.-P. a. B. J., A vectorial projection method for solving the navier-stokes equations, *Comptes Rendus de l'Académie des Sciences - Series IIB*, p. 1179–1184, 1999.
- [65] H. Van Der Vorst, A fast and smoothly converging variant of BI-CG for the solution of non-symmetric linear systems, *SIAM Journal on Scientific and Statistical Computing*, no. 44, p. 631–644, 1992.
- [66] I. Gustafsson, On First and Second Order Symmetric Factorization Methods for the Solution of Elliptic Difference Equations, PhD Dissertation, 1978.
- [67] D. Youngs, K. Morton and M. Baines, Time-dependant multimaterial flow with large fluid distortion, *Numerical Method for Fluid Dynamics*, 1982.
- [68] S. Vincent, J.P. Caltagirone and D. Jamet, Test-case no. 15: phase inversion in a closed box (PC), *Multiphase Science Technology*, no. 16, p. 101–104, 2004.
- [69] S. Vincent, J. Larocque, D. Lacanette, A. Toutant, P. Lubin and P. Sagaut, Numerical simulation of phase separation and a priori two-phase LES filtering, *Computational Fluids*, no. 37, p. 898–906, 2008.
- [70] S. Vincent, T. Randrianarivelo, G. Pianet and J.P. Caltagirone, Local penalty methods for flows interacting with moving solids at high Reynolds numbers, *Computational Fluids*, no. 36, p. 902–913, 2007.
- [71] S. Vincent and J.P. Caltagirone, A one cell local multigrid method for solving unsteady incompressible multiphase flows, *Journal of Computational Physics*, no. 163, p. 172–215, 2000.
- [72] H. K. a. M. W. Versteeg, An Introduction to Computational Fluid Dynamics - The Finite Volume Method, Harlow, England , Pearson Education Limited, 2007.
- [73] D. C. Wilcox, Turbulence Modeling for CFD La Cañada, California , DCW Industries, 1994.
- [74] H. K. Versteeg and W. Malalasekera, An Introduction to Computational Fluid Dynamics: *The Finite Volume Method*, vol. 2, Prentice Hall.

- [75] P. Sagaut, Large eddy simulation for incompressible flow - an introduction, Springer-Verlag, 2001.
- [76] O. Vasilyev, T. Lund, P. Moin and K. Aksellvoll, A general class of commutative filters for LES in complex geometries, *Journal of Computational Physics*, no. 146, pp. 82-104, 1998.
- [77] S. Vincent, J. Larocque, D. Lavanette, A. Toutant, P. Lubin and P. Sagaut, Numerical simulation of phase separation and a priori two-phase LES filtering, *Computers & Fluids*, no. 37, pp. 898-906, 2008.
- [78] J. Larocque, S. Vincent, L. Delphine, P. Lubin and J.P. Caltagirone, Parametric study of LES subgrid terms in a turbulent phase separation flow, *International Journal of Heat and Fluid Flow*, no. 31, pp. 536-544, 2010.
- [79] Y. Dakhoul and K. Bedford, Improved averaging method for turbulent flow simulation. Part 1: theoretical development and application to Burger's transport equation, *International Journal Number Methods Fluids*, no. 6, pp. 49-64, 1986.
- [80] Y. Dakhoul and K. Bedford, Improved averaging method for turbulent flow simulation. Part 2: calculation and verification, *International Journal Number Methods Fluids*, no. 6, pp. 65-82, 1986.
- [81] E. Labourasse, D. Lacanette, D. Toutant, S. Vincent, P. Lubin, O. Lebaigue, J. Caltagirone and P. Sagaut, Towards large eddy simulation of isothermal two-phase flows: governing equations and a priori tests, *International Journal of Multiphase Flows*, vol. 33, no. 1, pp. 1-39, 2007.
- [82] J. Chesnel, J. Reveillon, F. Demoulin and T. Menard, Subgrid modeling of liquid atomization. *6th International Conference on Multiphase Flow*, Leipzig, Germany, 2007.
- [83] Y. Zang, R. L. Street and J. Koseff, A dynamic mixed subgrid-scale model and its application to turbulent recirculating flows, *Physics of Fluids*, vol. 5, p. 3186 – 3196, 1993.
- [84] J. Smagorinsky, General Circulation Experiments with the primitive equations *Monthly Weather Review*, vol. 91, no. 3, pp. 99-151, March 1963.
- [85] J. Bardina, Improved turbulence models based on large eddy simulation of homogeneous incompressible turbulent flows, Stanford, California USA: Stanford University, Dept. Mech. Engr., 1983 .

- [86] I. Calmet, Analyse par simulation des grandes échelles des mouvements turbulents et du transfert de masse sous une interface plane in Thèse de doctorat, Institut National Polytechnique de Toulouse, 1995.
- [87] A. Merle, Interaction d'une bulle sphérique avec un écoulement turbulent ou tourbillonnaire in Thèse de doctorat, Institut National Polytechnique de Toulouse, 2004.
- [88] E. Arquis and J. Caltagirone, Sur les conditions hydrodynamiques au voisinage d'une interface milieu fluide-milieu poreux: application à la convection naturelle. *Comptes Rendus de l'Académie des Sciences - Séries IIB*, vol. 299, pp. 1-4, 1984.
- [89] K. Khadra, P. Angot, S. Parneix, J.P. Caltagirone, Fictitious domain approach for numerical modeling of navier-stokes equations, *International Journal of Numerical Methods in Fluids*, p. 651–684, 2000.
- [90] L. C. Hibbeler and B. G. Thomas, Investigation of Mold Flux Entrainment in CC Molds Due to Shear Layer Instability. *AISTech*, Pittsburgh, 2010.
- [91] M. Brocchini and D. Peregrine, The dynamics of strong turbulence at free surfaces. Part 1. Description, *Journal of Fluid Mechanics*, vol. 449, pp. 225-254, 2001.
- [92] M. Brocchini and D. Peregrine, The dynamics of strong turbulence at free surfaces. Part 2. Free-surface boundary conditions, *Journal Fluid Mechanics*, vol. 449, pp. 255-290, 2001.
- [93] P. Gardin, Z. Kountouriotis, K. Pericleous, G. Djambazov and J. Domgin, Study Of The Steel/Slag Interface Instability And The Influence Of Injected Gas In The Continuous Casting Of Steel, 2011.
- [94] P. Chaubal and R. Bommaraju, Development and use of a model to predict in-mold slag composition during the continuous casting of steel. *Steelmaking Conference Proceedings*, 1992.
- [95] S. Banerjee and S. MacIntyre, The air-water interface: turbulence and scalar exchange, 1998.
- [96] Herlina and G. H. Jirka, Experiments on gas transfer at the air–water interface induced by oscillating grid turbulence. *Journal of Fluid Mechanics*, vol. 594, pp. 183-208, January 2008.

- [97] C. G. Méndez, N. Nigro, A. Cardona, S. S. Begnis and W. P. Chiapparoli, Physical and numerical modeling of a gas stirred ladle. *First South American on Computational Mechanics*, Santa Fé-Parana, Argentina, 2002.
- [98] A. Conejo, S. Kitamura, N. Maruoka and S.-J. Kim, Effects of Top Layer, Nozzle Arrangement, and Gas Flow Rate on Mixing Time in Agitated Ladles by Bottom Gas Injection, *Metallurgical And Materials Transactions B*, 13 March 2013.
- [99] L. Zhang, Fluid Flow and inclusion removal in molten steel continuous casting strands. *Fifth International Conference on CFD in the Process Industries*, Melbourn, Australia, 2006.
- [100] A. Maurya and P. K. Jha, Effect of casting speed on continuous casting of steel slab International, *Journal of Mechanical Engineering and Robotics Research*, vol. 1, no. 1, pp. 13-21, 2014.
- [101] R. Kumar, Computational Fluid Dynamic Simulation for Continuous Casting process of Steels, National Institute of Technology, 2015.
- [102] P. Chaubal, Slag-Metal Reactions during the Continuous Casting of Steel. *Molten Slags, Fluxes and Salts*, Sydney, Australia, 1997.
- [103] L.D.O. Campos, P. Gardin, S. Vincent and J. P. Caltagirone, Fluid Flow and Turbulence Description in the vicinity of liquid/liquid Interfaces. *Turbulence Interactions 2015*, Cargese, France, 2015.
- [104] L.D.O. Campos, P. Gardin, S. Vincent and J.-P. Caltagirone, Fluid flow description in the vicinity of a liquid steel_slag interface. *The 6th International Congress on the Science and Technology of Steelmaking*, 2015.
- [105] L.D.O. Campos, P. Gardin, S. Vincent and J.-P. Caltagirone, Physical modeling of turbulent multiphase flow in continuous casting steel mold. *8th International Conference on Computational and Experimental Methods in Multiphase and Complex Flow*, 2015.
- [106] L.D.O. Campos, P. Gardin, V. Stéphane and J.P. Caltagirone, Physical and Numerical Fluid Flow and Mass Transfer Modeling in Continuous Casting Mold. *SCANMET V*, Lulea, Sweden, 2016.
- [107] J. Kubota, Mechanism of Level Fluctuation and Mold Powder Catching in Slab Continuous Casting at High Speeds. *The Sixth International Iron and Steel Congress*, Nagoya, 1990.